Alma Mater Studiorum – Università di Bologna

DOTTORATO DI RICERCA IN

Modellistica Fisica per la Protezione dell'Ambiente

Ciclo XXV

Settore Concorsuale di afferenza: 02/C1

Settore Scientifico disciplinare: FIS/06

TITOLO TESI

GLOBAL SCALE INVESTIGATION OF CIRRUS CLOUDS PROPERTIES USING ACTIVE AND PASSIVE SENSORS

Presentata da: Dott. Paolo Veglio

Coordinatore Dottorato	**Relatore**
Prof. Rolando Rizzi	Dott. Tiziano Maestri

Esame finale anno 2013

Sometime we see a cloud that's dragonish;
A vapour sometime like a bear or lion,
A tower'd citadel, a pendant rock,
A forked mountain, or blue promontory
With trees upon't, that nod unto the world,
And mock our eyes with air: thou hast seen these signs;
They are black vesper's pageants. [...]
That which is now a horse, even with a thought
The rack dislimns; and makes it indistinct,
As water is in water.

W. Shakespeare - *Antony and Cleopatra*

Contents

List of Figures

List of Tables

Chapter 1

Introduction

Clouds in the Earth atmosphere come in a large variety of habits with a great diversity in their physical characteristics, but the common denominator of all of them is the fundamental contribution they provide in the regulation of the Earth radiation budget (Wylie et al., 2005).

Clouds, in fact, have a twofold effect on the atmosphere. On one hand they attenuate the incoming solar radiation reflecting it back to space. This effect, which is known as cloud albedo, results in a cooling of the Earth–atmosphere system. On the other hand, clouds also absorb thermal infrared radiation emitted from both the Earth surface and the atmosphere, partially re-emitting it in all directions. This latter contribution, called infrared-greenhouse effect, causes an increase of the radiation budget which, in general, results in a warming of the Earth–atmosphere system. Therefore, the competition between the solar albedo and the infrared greenhouse effects determines whether the surface will undergo cooling or warming (Hartmann, 1994).

The Intergovernmental Panel for Climate Change (IPCC) in its fourth assessment (IPCC, 2007) concluded that the poor comprehension of the coupling between the clouds and the Earth's atmosphere still represents one of the largest source of uncertainties in climate and weather prediction. Clouds in fact, regularly cover about 50 % of the sky and it has been shown (Chahine et al., 2006; Wylie et al., 2005, 1994) that they "contamine" a great majority of satellite observations, with cirri especially. Moreover, clouds (cirri in particular), are difficult to model and their properties are in general tough to retrieve by satellite sensors (Waliser et al., 2009). The radiative impact of cirri, however, is crucial in determining the energy balance of the atmosphere

since the greenhouse and albedo effects can be both slightly predominant depending on the optical depth (McFarquhar et al., 2000).

1.1 Cirrus clouds

Cirrus clouds are morphologically described by the World Meteorological Organization (WMO) as *detached clouds in the form of white, delicate filaments or white or mostly white patches or narrow bands, which have a fibrous appearance, or a silky sheen, or both.* This description could have been useful in the past, when a meteorologist was deputed to the observation and classification of clouds, but is completely inadequate for a rigorous, modern classification, such as an automated procedure for the detection of clouds from remote sensing data. Hence, a more physical characterization can be provided considering the attributes that identify these clouds, that are the typical altitudes where they can be found in the atmosphere, the phase of the water particles and the optical thickness. Thus, cirri can be described as cold, optically thin clouds composed of frozen water droplets, that reside in the upper parts of the troposphere, often at temperatures below the homogeneous nucleation (i.e. -41 °C).

Nevertheless, one should not think that cirri do not have a relevant contribution when the radiation processes in the atmosphere are studied. A single cirrus, in fact, might have a small impact on the Earth radiation budget, but globally these clouds represent about the 40 % of all the clouds, and constantly cover more than 20 % of the Earth surface (see for example Wylie et al. (2005, 1994)), so that they cannot be lightly labeled as negligible, second order elements.

It has been shown that the sizes of ice crystals can have large variations along the cloud vertical (from 10 μm at cloud top up to few millimeters at cloud base), but differences in the particle size distributions (PSD) can be found also depending on the latitude (Field et al., 2007, 2008; Heymsfield and Miloshevich, 2003; Korolev et al., 2011).

At midlatitudes, where cirri are usually sinoptically generated, the gravitational deposition is the responsible of the increase in size of the ice crystals approaching the cloud base. The greater the vertical extent of the cloud, the deeper the ice crystals fall, giving them more time for growing due to vapor deposition and crystals aggregation (Field et al., 2008, 2005; Heymsfield et al., 2002). Cirrus clouds in the tropics are mainly originated from

an outflow of the convective core of cumulus clouds. The strong updrafts that occur in tropical regions can transport large ice crystals towards the cloud top, so that larger sizes are found with respect to the midlatitude cirri (Heymsfield, 2003).

Many studies, in the last two decades, investigated the results of in situ measurements of ice crystal sizes in order to determine the particle size distributions of cirrus clouds. All these works agree that the PSDs are generally bi-modal with a simultaneous presence of both small and large particles, with the former occurring more often than the latter (Baker and Lawson, 2006; Field et al., 2007, 2005; Heymsfield and Miloshevich, 1995; Ivanova et al., 2001; Zhao et al., 2011).

It is important to know the size of the ice crystals within cirrus clouds, since this quantity is related to the geometric cross section of the particles which, in turn, allows to study the interactions with the incident radiation. Moreover, ice crystals do not occur only in very different sizes but also in a large variety of habits, from simple shapes, such as hexagonal plates or columns (usually found at the cloud top), to very complex aggregates at cloud base. It has been shown (Baran et al., 2011; Baum et al., 2005a, 2011) that the best representation of the phase function is obtained when mixtures of habits are considered. Having a good model to represent the habit mixture of ice crystals is essential to better simulate the bulk properties of cirrus clouds, which, in turn, is required to improve the capabilities of the current general circulation models (GCM).

All these aspects of cirrus clouds need to be further investigated and, for this purpose, obtaining global measurements of radiative properties of cirri is crucial. A new opportunity is available to the scientific community, a constellation of satellites called A-train, in fact, became available for this task in the last few years. This series of satellites, the first of them is orbiting since 2002, flies in low polar orbit at an altitude of about 705 km and includes passive and active sensors capable of measuring the radiometric properties of the same cloud nearly simultaneously in a wide portion of the electromagnetic spectrum (Stephens and Vane, 2007; Stephens et al., 2002).

1.2 State of the art

The study of cirrus clouds have done many steps forward in the recent years and our comprehension of both their microphysical and optical properties

have widely improved, but still, many uncertainties are not solved yet.

Radiative processes

There have been a number of theoretical and experimental works that have examined the net radiative effect of cirri and the scattering properties of ice particles. For instance, Zhang et al. (1999) demonstrated that radiative cloud forcing is extremely sensitive to crystal shape and particle size distribution which, in general, results in a negative contribution (i.e. cooling) for small particles and in a positive one (i.e. warming) for large ice crystals. A theoretical study by Fu (2007) shows that the change of the aspect ratio of pristine hexagonal ice ctystals (i.e. the ratio between width and length of the particle) from 1.0 to 0.1 leads to differences in the reflected solar flux of about -70 $\mathrm{W\,m^{-2}}$ when a cloud with an optical depth of 4 is considered. Furthermore, a laboratory experiment by Ulanowski et al. (2006) shows that large differences can be found in the phase function, mainly at side and back scattering angles, if rough particles are taken into account instead of smooth ones.

In addition the vertical distribution of macrophysical and microphysical properties within a cloud influences its radiative features (Maestri et al., 2005) and the interpretation of remote sensing data. It has been shown by Maestri and Holz (2009) that different assumptions on vertical distribution of the IWC might impact cloud properties retrieval (i.e. optical depth and effective dimension) from infrared satellite measurements. Chiriaco et al. (2006), while highlighting the potentialities of using combined visible (532 nm) and infrared (10.6 μm) lidar observations for retrieving vertically resolved profiles of particle absorption efficiency, particle concentration and IWC, show the importance of determining the position of the maximum of absorption within a cloud layer and provide an example of the large variations in the retrievals of the particle effective sizes for different hypotheses on where maximum of absorption takes place. Along the same line of research, Zhang et al. (2010) demonstrate that homogeneous cloud assumptions of ice particle size on the vertical can affect the solar reflected bi-spectral and infrared split-window methods to different extents and, consequently, can lead to significantly different retrievals of effective dimensions and IWC. The importance of knowing the vertical structure is discussed in detail also by Yang et al. (2012), who showed that, making use of in situ measurements of ice crystal habit and size distribution to better define cirrus cloud properties, results in non-negligible

differences in the simulated radiative fluxes of the order of $10\,\mathrm{W\,m^{-2}}$.

Scattering in the Far Infrared

All the above cited studies mostly analyze the visible and the near infrared (up to about $15\,\mu$m) portions of the electromagnetic spectrum. It has been shown, however, that the study of the far infrared (FIR) can be of major importance to better understand the Earth energy balance and to characterize clouds, cirri in particular (Harries et al., 2008). In this review our current knowledge of the far infrared (FIR) portion of the Earth's infrared emission to space is discussed. Harries et al. (2008) point out that the FIR is important to the understanding of the climate system because the Earth is a cool object in space and the peak energy from a blackbody at 255 K occurs at about $500\,\mathrm{cm^{-1}}$, according to the well known Wien's law. They also state that, in clear sky conditions, 35 % of the energy escaping to space is at wave numbers below $500\,\mathrm{cm^{-1}}$ and that the emission comes from the upper troposphere because the lower troposphere, over most of the planet, is totally opaque and the surface is obscured.

One of the issues to be considered is how well we account for the longwave emission to space in the FIR, in presence of cold clouds. There is a clear connection with the broad issue of the role of clouds for the Earth's radiative balance at the top of the atmosphere (TOA), since the net effect of cold clouds is the difference of their shortwave and longwave radiation budget. The presence of ice clouds, and to a lesser extent of warm water clouds, increases considerably the role of the FIR within the total emission to space. This was quantified by Rizzi and Mannozzi (2000), that compute spectral radiance emitted vertically to space at TOA for six standard atmospheres (Anderson et al., 1986) for clear sky conditions and for a range of warm and cold clouds of various top heights and particulate density. The radiance is integrated in the range 100 to $600\,\mathrm{cm^{-1}}$ (FIR) and in the 50 to $2700\,\mathrm{cm^{-1}}$ one and attention is focused on the ratio of the two quantities. It has been shown that in clear sky conditions this ratio attains values ranging from 0.38 for the tropical (TRO) atmosphere to 0.48 for the sub-arctic winter (SAW) profile. In presence of clouds the ratio increases with the opacity of the cloud and its height, which is to be expected. The largest values are found at the Tropics (close to 0.6) since in the tropical area clouds can be very high hence cold. An opaque cloud with top at 8.7 km placed in a sub-arctic winter and summer atmosphere produces a ratio of respectively 0.45 and 0.51.

These results indicate that great care should be used when defining the radiative properties especially of cold clouds. In fact ice crystal models that are used to predict their radiative properties should be applicable over large wavelength ranges (Baran, 2009). At this purpose an intense testing activity of the main radiative properties is being performed by various groups. Ham et al. (2009) compare cloudy satellite radiances measured by MODIS (King et al., 1997) to simulations and show that radiances for short-wave bands (from which the cloud optical properties were retrieved) appear to be quite accurate with errors on the order of 5 %. However simulated radiances for mid infrared and infrared window bands show larger discrepancies with the observed radiances. The authors suggest that the discrepancies are likely due lack of accuracy in the estimate of cloud-top and cloud-base heights and also that the simulations could be substantially improved by accounting for the vertical cloud distribution provided by colocated active sensors. Bozzo et al. (2010) perform a similar comparison to airborne data collected by MAS (King et al., 1996). Their state-of-the-art simulation stategy uses retrieved cloud optical depth and effective radius from co-located S-HIS (Revercomb et al., 1998), cloud height and geometrical thickness from colocated airborne lidar and atmospheric thermodynamic profiles from drop-sondes. Their results show excellent agreement in long-wave bands (where the cloud optical depth and effective radius are retrieved), but a sensible underestimation of short-wave radiances. They also show that the impact of the assumptions on particle size distribution and vertical profile of ice content is much smaller than the observed differences between measured and simulated radiances. In order to understand their results they simulate also MODIS data in short-wave channels, using MODIS operational cloud parameters (retrieved from shortwave MODIS channels) and obtain a very good agreement. They state that the likely cause of the contradictory results is the consistency of the database of single scattering properties of ice crystals over the wavelength domain from shortwave to infrared. Baum et al. (2010) develop new bulk scattering and absorption properties on the basis of updated microphysical data and libraries of single-scattering properties. Comparing simulations against CALIOP data, models built with severely roughened particles compare best for all the considered habit mixtures. They state that the use of roughened rather than smooth particles to infer optical thickness and effective diameter from satellite imagery, such as MODIS, results in a decrease in optical thickness and an increase in particle size, thus suggesting that operational cloudy product might be affected by large uncertainties. Cox

et al. (2010) state that cloudy radiance simulations are not able to consistently reproduce the observed spectral radiances across the entire infrared region, and are particularly poor in the 330-600 cm^{-1} region. They also state that possible causes are model input uncertainties arising from inadequate sampling of the cloud structure and of atmospheric parameters. The discrepancies between state-of-the-art simulations and radiances measured in cloudy conditions may originate from various factors, as highlighted above. The important point is that these properties can be tested against available measurements by a number of multi spectral radiometers covering the shortwave to infrared range, and in addition by hyper-spectral infrared spectrometers. Unfortunately there are currently no spaceborne sensors that measure spectral radiance in the FIR, at any spectral resolution, and very little FIR experimental activity which is a serious weakness in our capability to assess the quality of the basic radiative properties that are used in all transfer computations also in climate (and meteorological) models, in particular in cloudy conditions.

The role of scattering processes for infrared computations in presence of clouds is a subject of some debate, since scattering processes greatly increases the complexity of the transfer computations. The imaginary part of the ice refractive index has a local minimum in the FIR around 450 cm^{-1}, while the real part shows values comparable or greater than in the main IR window. Di Giuseppe and Rizzi (1999) derive a simple formula that allows to estimate the irradiance upwelling from a cloud layer given its basic radiative parameters (direct transmittance, diffuse transmittance and reflectance) computed as by (Mannozzi et al., 1999). They compute the difference (SE) in spectral irradiance between a case with no scattering and the general case, normalised to the latter, for a number of effective radii of the cloud size distribution and ice water path. They conclude that scattering increases the optical depth of the cloud and reduces the upwelling irradiance at all wavelegths, and the largest values of SE are found in the region around 400 cm^{-1}, at the margin of both the CO_2 vibro-rotational band and of the H_20 rotational band, characterised by relatively high values of single scattering albedo for typical cirrus size distributions. They also state that this region of the spectrum may hold some promise for the identification of high clouds using remote sensing.

A further reason to explore the behaviour of cold clouds at FIR wavelengths stems from results presented by Stackhouse and Stephens (1991). They point out that detailed calculations of the longwave radiative budget

of a cirrus cloud demonstrate that the net budget is the result of heating at window wavelengths and cooling in the more opaque water vapor bands. The subject is investigated also by (Maestri and Rizzi, 2003b) and the previous results are confirmed for a number of cold clouds in the tropical atmosphere. Hence it is a well established result that the longwave heat budget of cold clouds, which is an important part of the cloud radiative budget, is determined by a difference between radiative heating and cooling, the latter taking place in the FIR.

Cloud Properties

The knowledge of the radiative contribution of cirrus clouds is only one of the aspects currently under investigation. It has been pointed out by many authors (e.g. Berthier et al. (2008); Nazaryan et al. (2008); Martins et al. (2011)) that a better understanding of spatio-temporal distributions of these clouds, both vertical and horizontal, would be extremely helpful in improving the parameterization of ice clouds in the existing numerical models. At this regard, a detailed study of occurrence of cirrus clouds was recently performed by Nazaryan et al. (2008), who report global and seasonal frequencies, as well as top and base height distributions of cirri analyzing a year of CALIOP (Cloud-Aerosol Lidar with Orthogonal Polarization) data. A similar work is performed by Sassen et al. (2008), utilizing a year of combined CloudSat/CALIPSO data, who also introduce a study of the day versus night differences. Berthier et al. (2008) study and compare the data provided by LITE (Lidar In-space Technology Experiment), GLAS (Geoscience Laser Altimeter System) and CALIOP spaceborne lidar sensors in order to investigate the influence of the intra- and inter-annual variability of intertropical convergence zone (ITCZ) latitudinal position and polar stratospheric clouds (PSC) on the lidar cloud top heights for different latitudinal regions and altitudes. Also Martins et al. (2011) perform a detailed statistical analysis of cirrus clouds providing distributions of some physical quantities such as geometrical thickness, cloud top height, midlayer temperature and ice crystals depolarization ratios, using nighttime CALIPSO data. They also found correlations between these physical properties and horizontal and vertical wind speed, characterizing the air motions in the tropics and the jet streams at midlatitudes.

Microphysics

As briefly reported in the previous section, the microphysics of ice clouds (i.e. PSDs and ice crystal shapes) is another piece of the puzzle that is the study of ice clouds. Two ways are available for the study of the cirri microphysics: the in situ and the remote sensing measurements. For the former method an airborne instrument is usually employed, but the high altitudes and the extreme flight conditions make these measurements hard to obtain. Moreover, in situ measures are obviously limited to a very small region, or even to a single cloud, and a global study is technically impossible. Satellite-borne instruments, on the other hand, are able to provide global, or nearly global measurements, but they have to face with the difficulties related to the retrieval of ice cloud properties. In order to overcome these limitations, the use of multiple sensors that scan a single scene in different regions of the electromagnetic spectrum can be very helpful. This kind of approach, already used for the study of small regions with ground-based sensors, has recently become available on a global scale with the A-Train satellite constellation which is composed by a set of active and passive sensors able to provide measurements of a single scene from visible to microwave frequencies.

As it can be seen by this brief and surely non-exhaustive summary of recent works, a wide variety of fields of the atmospheric physics is involved in the study of cirrus clouds and a lot of efforts are put into improving our knowledge in this sense. The literature about cirri is flourishing, denoting a deep interest in this topic and a pressing need of reducing the uncertainties related with the unknowns about optically thin ice clouds. The results presented in this work contribute to a better definition of cirrus clouds properties, providing information on their average vertical structure and on their optical features in the far infrared portion of the electromagnetic spectrum. Moreover, the basis for a future development of the study are set with the realization of a database made of satellite data from multiple sensors.

1.3 Work goals and overview

The present work introduces a study of optically thin ice clouds in the upper troposphere providing an analysis of bulk properties and, for the first time, of vertical features of cirri on a global extent. This goal is achieved by performing a detailed statistical analysis on a full year of satellite lidar products

(CALIOP).

A second aspect under investigation is the ability to represent the scattering properties of ice cloud particles in the far infrared. For this purpose the radiances of a limited number of FOVs, derived from a case study, are compared to those produced by a forward radiative transfer code. The radiative transfer algorithms utilized in this study make use of vertical profiles of atmospheric quantities such as altitude, pressure, temperature and ice water content. This latter quantity is derived by using the results found in the analysis of the CALIOP data.

The last goal of this work, that marks a possible path for future progresses in the study of ice cloud properties, is the development of a database of collocated satellite products. Data from a hyperspectral sounder (AIRS), an imager (MODIS) and a lidar (CALIOP) are merged together in a single product that contains most of the variables available from these three instruments. It has been shown, in fact, that having simultaneous measurements of the same scene in different spectral intervals and at various spatial resolution can largely improve the knowledge on cirrus clouds. Moreover, the satellite sensors provide constant global measurements, that are crucial in the study of climate.

1.3.1 Work summary

The present thesis is organized as follows. In Chapter 2 a description of the instruments, focusing in particular on CALIOP and on the lidar physics in general, is provided. Moreover the CALIOP products used in this work are described. The data of the lidar CALIOP are analyzed in Chapter 3, where two data set of ice clouds, homogeneous and non-homogeneous, are defined and statistics on frequency of occurrence are given. In Chapter 4 annual and seasonal mean backscatter profiles are computed for night and day and for tropics and midlatitudes. The influence of the main atmospheric and cloud parameters on mean BSPs is studied. Fitting functions, that describe the mean shape of the BSP as function of the cloud geometrical thickness, are derived. In the last section of the Chapter the relationship between backscatter profile and ice water content profile is discussed. Chapter 5 describes the COBRA-ECOWAR experiment. The results of the backscatter profiles analysis are utilized to improve an infrared cloud properties retrieval algorithm (RT-RET). The output of this code are used to simulate the radiances with a forward radiative transfer code (RTX). A comparison between the measured

and the simulated radiances is performed and sensitivity studies are conducted. In Chapter 6 a methodology to collocate data from different satellite sensors is described. The resulting collocated data set is used to test one of the output of a new physical-statistical infrared retrieval. A summary is given in Chapter 7 and future developments of this work are discussed.

Chapter 2

The CALIPSO mission and the lidar physics

Since the advent of the satellite era in the '70s the space-borne instruments have provided valuable measurements for the study of atmosphere and clouds. One of the obvious advantages of using satellite-borne sensors for the study of the Earth atmosphere is the possibility of having global measurements of what is to be observed and investigated, allowing an advancement in the general understading of its properties. This peculiar point of observation is particularly important in the study of clouds, which can have very different characteristics depending, among other factors, on where they are originated.

Among the many sensors orbiting around the Earth, of particular importance are those of the A-Train constellation (for a brief description see Section 2.1), some of which are used in this work. The A-Train, finding inspiration in the Aristotle's words "*the whole is more than the sum of its parts*", offers the unique opportunity of having almost simultaneous measurements of the same atmospheric column from different instruments. The multi-sensor approach, in fact, is very useful to overcome the limitations of a single instrument. In the study of clouds, for example, radars are sensitive to optically thick clouds, but lack in the detection of particles smaller than about 100 microns. On the other hand lidars are sensitive to such small particles but they are not able to penetrate clouds with optical depths larger than about 3. A somehow similar thought process can be made also for passive sensors such as radiometers or interferometers, depending on which part of the electromagnetic spectrum they measure. The visible wavelengths are commonly used to obtain microphysical information on clouds, such as

particle sizes and shapes while the infrared is mostly used for the cloud top detection (if a satellite-borne instrument is considered).

Last but not least, the downlooking perspective presents some undisputed advantages for the study of ice clouds in the high troposphere. The signal, in fact, is only poorly attenuated by the column of the atmosphere between the satellite and the cloud. On the contrary, a signal from the ground can be attenuated by aerosol and water vapor, whose average concentration strongly decreases with altitude, and also by low, optically thick water clouds such as cumuli that could even prevent the observation of the ice clouds above them.

2.1 The A-Train Constellation

The Afternoon "A-Train" Constellation presently consists of five satellites (GCOM-W1, Aqua, CALIPSO, CloudSat and Aura) in a polar orbit at a nominal altitude of 705 km, crossing the equator northbound at about 1:30 p.m. local time within seconds to minutes of each other. Together these satellites contain 17 scientific instruments that observe the same portion of atmosphere at a very broad range of wavelengths. A scheme of the constellation is shown in Figure 2.1. A brief description of the A-Train satellites is provided in what follows.

2.1.1 Aqua

Aqua is the oldest component of the A-Train formation, orbiting around the Earth since May 2002. As the name suggests, the main objective of this satellite is the study of water in the Earth-Atmosphere system, although its capabilities cover also some aspects of climate and biosphere. Among the six instruments carried by this satellite there are MODIS, AIRS and CERES.

MODIS (Moderate resolution Imaging Spectroradiometer) is a cross-tracking scanning radiometer with 36 bands spanning the visible and infrared portions of the electromagnetic spectrum. MODIS was constructed to obtain information about a wide variety of biological and physical processes crucial in the study of the Earth system. Due to its small field of view (1 km at nadir) and its ability to measure in multiple spectral channels, it is widely used in cloud characterization and studies.

AIRS (Atmospheric Infrared Sounder) is a high spectral resolution infrared sounder designed primarly to obtain temperature and humidity pro-

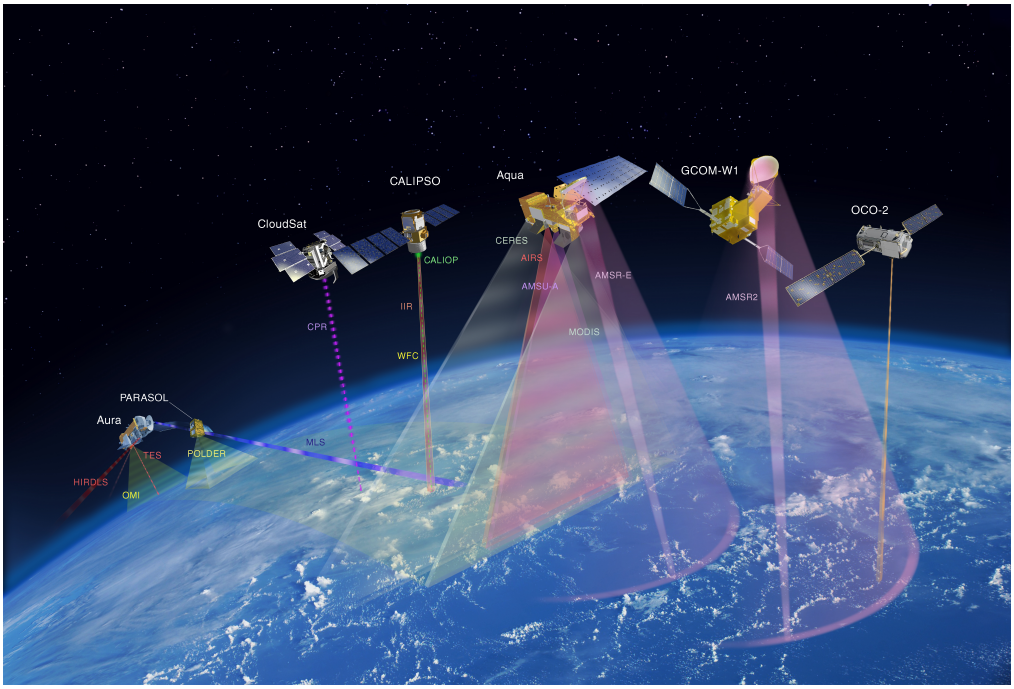

Figure 2.1: Artist's concept of the A-Train Constellation. The footprint of each of the A-Train's instruments is shown: active instruments aboard CALIPSO/CALIOP and CloudSat/CPR are indicated with dashed lines. This illustration color-codes instrument swaths based on observed wavelength ranges. Microwaves (observed by both AMSRs, AMSU-A, CPR, MLS) are represented by red-purple to deep purple colors; solar wavelengths (POLDER, OMI, OCO-2), yellow; solar and infrared wavelengths (MODIS, CERES), gray; other infrared wavelengths (IIR, AIRS, TES, HIRDLS) are represented by reds.

files from the surface to an altitude of about 40 km. AIRS has a spectral coverage from 3.7 to 15.4 microns and a spectral resolving power ($\lambda/\Delta\lambda$) of 1200. AIRS is a cross-scanning instrument with a nadir spatial resolution of 13.5 km. Calibrated radiances have an absolute accuracy of 3% or better (Aumann and Miller, 1995) and their uncertainty estimate is less than 0.2%. For the study of clouds the AIRS standard products include cloud top height, cloud fraction and cloud top temperature. These products have a key role in the study of radiative transfer in the atmosphere (Yue et al., 2007).

For their technical features AIRS and MODIS are of particular interest in this study and extremely useful in complementing the analysis of CALIPSO data. Other sensors on Aqua (not used here but potentially important in the study of clouds) are briefly described below.

CERES (Clouds and Earth's Radiant Energy System) is a broadband scanning radiometer intended to measure major elements of the Earth's radiation balance and aid climate change studies.

The AMSU (Advanced Microwave Sounding Unit) is a microwave radiometer designed to retrieve atmospheric temperature profiles, particularly in cloudy conditions.

HSB (Humidity Sounder for Brazil), provided by Brazil's National Institute for Space Research, is used to obtain humidity soundings in the atmosphere, for determining the liquid water content in clouds, precipitation and integrated precipitable water. HSB and AMSU measurements in the microwave are important to complement and enhance the AIRS measurements, particularly in presence of clouds.

2.1.2 CloudSat

CloudSat is an Earth System Science Pathfinder (ESSP) mission that studies clouds in detail to better characterize the role they play in regulating the Earth's climate. CloudSat carries a Cloud Profiling Radar (CPR) with a vertical resolution of 500 m. The main goal of this mission is to improve the quality of cloud parameterization with a consequent increase of the accuracy of weather forecasts and climate predictions. For this task the radar employs a signal in the upper microwave region (94 GHz) that it is not significantly attenuated by clouds, so that the instrument is able to detect about 90% of all ice clouds and 80% of all water clouds.

2.1.3 CALIPSO

CALIPSO (Cloud-Aerosol Lidar and Infrared Pathfinder Satellite Observation) is a joint NASA and CNES (Centre Nationale d'Etudes Spatiales) satellite mission with an on-board payload which includes an active lidar (CALIOP) and two imagers (WFC and IIR) with channels in both visible and infrared wavelengths.

CALIOP (Cloud-Aerosol Lidar with Orthogonal Polarization) is a two-wavelength polarization-sensitive lidar that provides high-resolution vertical profiles of aerosols and clouds with a pulse repetition frequency (PRF) of 20.16 Hz. It has a field of view of 100 μrad corresponding to a footprint of about 100 meters on the ground. The lidar makes use of three receiver channels: one measuring the 1064 nm backscattered signal and two channels measuring orthogonally polarized components of the 532 nm backscattered signal. Both wavelengths are utilized for the aerosols while for the clouds only the 532 nm produces data.

Data from the CALIOP lidar will be utilized in this work so a description of its products and of the lidar physics in general will be provided in Sections 2.3 and 2.2 respectively.

WFC (Wide Field Camera) is a fixed nadir-viewing imager with a single spectral channel covering the 620-670 nm region, selected to match band 1 of the MODIS instrument on Aqua. This camera is useful to have a visible image of the region sensed by CALIOP.

IIR (Imaging Infrared Radiometer) is a three-channel IIR provided by CNES (Centre National d'Etudes Spatiales) with algorithm development performed by the institute Pierre Simon Laplace (IPSL) in Paris. It is a nadir-viewing, non-scanning imager having a 64 km by 64 km swath with a pixel size of 1 km. The CALIOP beam is nominally aligned with the center of the IIR image. This instrument uses a single microbolometer detecter array, with a rotating filter wheel providing measurements at three channels in the thermal infrared window region at 8.7 μm, 10.5 μm and 12.0 μm. These wavelengths were selected to optimize joint CALIOP/IIR retrievals of cirrus cloud emissivity and particle size.

2.1.4 Other satellites of the A-Train

Here below a brief description of the other past, present and future components of the A-Train is provided for sake of completeness.

The Global Change Observation Mission-Water (GCOM-W1) "SHIZUKU" satellite aims to construct, use, and verify systems that enable continuous global-scale observations (for 10 to 15 years) of effective geophysical parameters attempting to explain global climate change and water circulation mechanisms. The GCOM-W1 will observe precipitation, vapor amounts, wind velocity above the ocean, sea water temperatures, water levels on land areas and snow depths with a microwave radiometer.

PARASOL (Polarization and Anisotropy of Reflectances for Atmospheric Sciences coupled with Observations from a Lidar) is a former A-Train component (until early december 2009 when its orbit was lowered), which takes measurements of the total and polarized light in several wavelengths and at different viewing angles. The instrument on board is the Polarization and Directionality of the Earth's Reflectances (POLDER) which has nine spectral bands in the visible and the near infrared part of the spectrum. Information on polarization in several directions can be very useful for characterizing clouds and aerosols in the atmosphere.

Aura contain four instruments that study the atmosphere's chemistry and dynamics. Aura is designed to investigate questions about ozone trends, air-quality changes and their linkage to climate change. Aura's measurements also provide accurate data for predictive models and useful information for local and national agency decision-support systems.

The Glory satellite consisted of three instruments. Its mission was designed to collect data on the optical, microphysical, and chemical properties, and spatial and temporal distributions of aerosols and clouds. Glory spacecraft failed to reach orbit after its liftoff on March 4th, 2011.

OCO-2 (Orbiting Carbon Observatory 2) is designed to provide space-based global measurements of atmospheric carbon dioxide (CO_2) with the precision and resolution needed to identify and characterize the processes that regulate this important greenhouse gas. With its three high-resolution grating spectrometers, data collected by OCO-2 could be combined with meteorological observations and ground-based CO_2 measurement to help characterize carbon dioxide sources and sinks on regional scales at monthly intervals for 2 years. The OCO-2 spacecraft is scheduled to join the constellation in 2014.

2.2 Lidar physics

The lidar (Light Detection And Ranging) is an optical remote sensing technology that measures properties of scattered light to obtain physical information on targets (i.e. cloud particles, aerosols and molecules). Lidar operates on the same principle of the radar, as they are both active instruments which make use of an electromagnetic signal to measure physical properties. The two sensors differ in the frequency of the signal since radars operate in the microwave region and lidars work in the solar part of the spectrum (mostly visible and near infrared). This allows lidars to use highly coherent and monochromatic beams of light. The lidar system measures the backscatter signal, that is the signal scattered at an angle π (or close) with respect to the direction of the incident beam.

When a parcel of air, that is a small volume containing a spectrum of molecules and/or particulates is accounted for, the scattering coefficient β_{sca} is defined as:

$$\beta_{sca} = \int_{\Delta z} \sigma_{sca}(z) \frac{n(z)}{\Delta z} dz \quad [\mathrm{m}^{-1}] \tag{2.1}$$

where σ_{sca} denotes the scattering cross section [m^2], n the number density of the scatterers [m^{-3}] and Δz a differential thickness (see also Liou (1986)) so that their fraction represents the particles size distribution (PSD). In the case of the lidar the backscatter coefficient β_{bs} usually is

$$\beta_{bs} = \beta_{sca} P(\pi, \phi, 0, \phi') \tag{2.2}$$

where $P(\theta, \phi, \theta', \phi')$ is the mean phase function of the scatterers' distribution, θ and ϕ denote the outgoing direction and θ' and ϕ' the incoming direction.

It is useful to remember that the backscatter coefficient is in general the sum of a parallel and a perpendicular component, as referred to the two directions of polarization. In the following, the use of the term backscatter coefficient is to be always intended as the total backscatter coefficient (i.e. the sum of the two components) where not otherwise specified.
A definition analogous to the one provided in Equation 2.1 can be given for the extinction coefficient β_{ext}:

$$\beta_{ext} = \int_{\Delta z} \sigma_{ext}(z) \frac{n(z)}{\Delta z} dz \quad [\mathrm{m}^{-1}] \tag{2.3}$$

where σ_{ext} is the extinction cross section in m^{-2}. In the case of CALIOP

this quantity is derived from the total backscatter coefficient (Young et al. (2008)).

An important indirect quantity is the "lidar ratio", that is the extinction-to-backscatter ratio. The lidar ratio is defined as:

$$S_P = \frac{\beta_{ext}}{\beta_{bs}} = \frac{\beta_{sca} + \beta_{abs}}{\beta_{bs}} \quad [\text{sr}] \tag{2.4}$$

where β_{abs} and β_{sca} are the particulate absorption and scattering coefficients respectively. Since it is very sensitive to particle size this quantity can be used to obtain information about the dimension of the scattering particle's size distribution. CALIOP data contain the initial and final lidar ratio. The initial lidar ratio is an initial estimate of the particulate extinction-to-backscatter ratio. These estimates are obtained averaging the values of every type of particulates' lidar ratios from data such as the one in Omar et al. (2005) or Cattrall et al. (2005). The CALIOP Scene Classification Algorithm (SCA) (Liu et al. (2005)) identifies the type of layer analyzed and assigns the corresponding initial lidar ratio. The final lidar ratio can be both derived using measured layer transmittance or set to the initial lidar ratio by the SCA algorithm (for more information visit the CALIPSO web-site[1]). By introducing the atmospheric transmittance $\mathcal{T}$ between the lidar and the distance r:

$$\mathcal{T}(0, r) = \exp\left(-\int_0^r \beta_{ext}(r')dr'\right) \tag{2.5}$$

with β_{ext} the extinction coefficient, it is possible to write the lidar equation as:

$$P(r) = \frac{1}{r^2} E_0 \xi \cdot [\beta_{bs,P}(r) + \beta_{bs,M}(r)]\, \mathcal{T}^2(0, r) \quad [\text{W}] \tag{2.6}$$

where $P(r)$ is the detected backscattered signal from the air parcel at a distance r, E_0 is the average laser energy for the single shot, $\beta_{bs,P}(r)$ and $\beta_{bs,M}$ are the backscatter coefficients for particulate and molecules respectively (see Young et al. (2008) for more details) and ξ is the lidar system parameter. This last quantity takes account of all the instrument properties (e.g. receiver area and optical efficiency, detector quantum efficiency, receiver field of view, ...). Because some of these factors vary with time, ξ is slightly variable and depends on the satellite position and height, degradation of the detectors

[1] `http://www-calipso.larc.nasa.gov/resources/calipso_users_guide/data_summaries/layer/index.php#final_532_lidar_ratio`

and thermal/mechanical effects. The corrections due to electronics are set prior to launch, the effects of degradation and environment characteristics, on the other hand, are constantly measured and corrected when necessary (see Hostetler et al. (2006)). Level 2 data (see Section 2.3), that we are going to use in this work, are calibrated.

Together with trasmissivity a very useful parameter to express the capability of a layer to extinguish electromagnetic radiation at a given wavelength is the optical depth (OD) τ:

$$\tau = \int_{z(p_1)}^{z(p_2)} \beta_{ext} dz' \tag{2.7}$$

where β_{ext} denotes the extinction coefficient and z is the height at a given pressure p. In the case of CALIOP the optical depth is computed from the product of the lidar ratio and the vertically integrated backscatter. According to Young et al. (2008) this quantity is often underestimated, particularly in low Signal-to-Noise Ratio (SNR) condition or in cases of overlapped clouds.

2.3 CALIOP products

The CALIOP data utilized in this work are the Level 2 (L2) cloud data products, which are divided in layer (CLay) and profile (CPro) products. The CLay content has column and layer descriptors. The column descriptors contain information on temporal and geophysical location and details on surface type, sunlight conditions and number of cloud layers. Each layer is then described by the layer descriptors, which provide information on spatial and physical characteristics of the scattering layers. The CLay parameters here used are: cloud top and base altitude (z_t and z_b), cloud optical depth (τ), latitude and longitude of the instantaneous field of view (iFOV), UTC time of measurement, layer midpoint temperature and the feature classification flags (see `http://www-calipso.larc.nasa.gov/resources/calipso_users_guide/data_summaries/layer/#feature_classification_flags`). The midlayer temperatures contained in the CLay data are derived from the GEOS-5 (Goddard Earth Observing System) model and provided by the GMAO (Global Modeling Assimilation Office) Data Assimilation System (`http://gmao.gsfc.nasa.gov/index.php`).

The CPro files provide information on the whole atmospheric column and, in particular, contain the measured vertical profiles of particulate backscatter

and extinction coefficients. The backscatter coefficient ($\beta'(z)$, including particulate and molecular components) is derived from the measured attenuated backscatter:

$$\beta_a(z) = \beta'(z)\mathcal{T}^2(z) \tag{2.8}$$

where $\mathcal{T}^2$ is the two-way transmittance. Note that symbols used in the present work do not correspond with those used in the CALIPSO documentation (references are given throughout the text) and caution should be taken to avoid possible confusion. The derivation of the particulate backscatter coefficient ($\beta(z)$) from the above equation requires estimation of additional quantities (i.e. multiple scattering factor) and ancillary data (i.e. molecular number density and ozone absorption coefficient profiles) whose calculation might lead to errors and uncertainties in the retrieved products, as discussed in `http://www-calipso.larc.nasa.gov/resources/pdfs/PC-SCI-202_Part4_v1.0.pdf`. In the present study it is assumed that any measurement uncertainty and error associated with cloud products retrieval do not systematically affect the shape of the BSP (and ETP).

The uncertainties associated with the particulate backscatter and extinction coefficients in the Level 2 data lead to estimate percentage errors of the order of 40–50% along the cloud body, both for backscatter and extinction coefficient. The percentage errors are usually larger (of a factor 2 or even 3) close to cloud base and top where the backscatter signal might be very low. All the errors are considered random and totally uncorrelated (`http://eosweb.larc.nasa.gov/PRODOCS/calipso/pdf/CALIOP_Version3_Extinction_Error_Analysis.pdf`).

Once the particulate backscatter is retrieved, the particulate extinction ($\sigma(z)$) at level z is obtained by multiplying by the appropriate particulate lidar ratio S_P:

$$\sigma(z) = S_P\beta(z) \tag{2.9}$$

Note that in the CALIOP data processing, to derive analytical solutions from the lidar equation, the lidar ratio is constant throughout a feature layer (i.e. within a cloud). As a consequence, backscatter and extinction profiles of the considered cirrus clouds have the same shape, thus the same results can be obtained studying either the ETPs or BSPs. The backscatter coefficient profile is derived from the 532 nm laser data. Its vertical resolution is 60 m (from ground level up to a height of 20.2 km). Horizontal resolution of CPro (and corresponding CLay) data is 5 km, obtained by measures of 15 iFOVs of about 80 m each. In addition, CLay files are also provided at two higher

horizontal resolutions: at 1 km, that will be used in the homogenization process of the CALIOP cirrus database (see Section 3.2.1), and at 333 m.

Chapter 3

Study of the CALIOP Database

The present study is focused on tropical and midlatitude areas. Three latitudinal belts are initially defined: tropics (30° S–30° N), midlatitudes North (30° N–60° N) and midlatitudes South (30° S–60° S). The distinction is done considering the different physical processes that characterize these regions, such as stronger convection in tropical zones, different mean circulation, diverse cloud formation processes (Holton, 2004; Lynch et al., 2002; Sassen et al., 2008). Data collected in polar regions (above 60° N and below 60° S) are excluded from the database since the quasi-polar orbit of the CALIPSO satellite causes oversampling of very high latitude areas.

The content of the following two chapters is also reported in the paper by Veglio and Maestri (2011).

3.1 Cirrus Cloud Database

A cirrus cloud database (CCD), consisting of data concerning high-level iced clouds only, is derived from the full database containing all the CLay and CPro files of year 2008 (about 20 000 files for a total of around 80 million FOVs). CALIPSO ETPs and BSPs are selected and stored into the CCD if all the conditions listed in Table 3.1 are met. These conditions are applied to ancillary data of the CLay files to obtain a CCD consisting of BSPs (and thus ETPs) of high-altitude, optically thin ice clouds over the ocean.

Cloud base threshold altitude is set at 5 km at both ML and at 8 km at tropics (TRO) similarly to what done in previous works (Eguchi et al., 2007; Nazaryan et al., 2008). Clouds with optical depth larger than 10^{-3} and

Table 3.1: Conditions used for the selection of clouds in the Cirrus Cloud Database.

	Condition	Value
(1)	Surface:	sea
(2)	Cloud Layer base:	
	TRO	$> 8\,\mathrm{km}$
	ML	$> 5\,\mathrm{km}$
(3)	Cloud Layer top:	$< 20\,\mathrm{km}$
(4)	Midpoint Temperature:	$<273\,\mathrm{K}$
(5)	Cloud Type and Phase:	ice clouds
	Feature Type	2 (cloud)
	Feature Type QA	3 (high confidence)
	Ice/Water Phase	1 or 3 (ice)
	Ice/Water Phase QA	≥ 2
(6)	Cloud Layer:	Upper layer
(7)	Cloud Optical Depth:	$0.001 < \mathrm{OD} < 2$

less than 2 only are selected. As in Martins et al. (2011) cloud layers with optical depth smaller than 10^{-3} are removed because they are considered to be below the threshold confidence of lidar data and can be attributed to noise. Maximum optical depth allowed is set at 2.0 so that the full cloud body is sensed by the lidar ray and total attenuation is not reached.

The selection of ice phase clouds only is obtained through the use of multiple requirements: altitude of base and top (conditions 2 and 3 of Table 3.1), midpoint temperature (i.e. the temperature at the geometrical middle-point of the cloud thickness, condition 4) and above all the use of CALIOP Feature Classification Flags (condition 5). As in Nazaryan et al. (2008) only those cloud layers from the CALIPSO data record that are identified by the CALIOP cloud-aerosol discrimination (CAD) algorithm as clouds with high level of confidence (Feature Type QA equals 3) are selected. To avoid the presence of supercooled water clouds in our reduced database further conditions provided by CAD algorithm and concerning the cloud phase are used: the Ice/Water Phase field of the Feature Classification Flags must be either randomly or horizontally oriented ice particles.

Requirement number 6 in Table 3.1 ("Cloud Layer" equals "upper-layer" cloud) is introduced to account for multiple-layer clouds. When more than

Table 3.2: Cirrus clouds cover obtained from the cirrus cloud database, CCD.

	Day	Night	Total
Midlatitudes North	36 %	35 %	36 %
Tropics	35 %	39 %	37 %
Midlatitudes South	32 %	30 %	31 %

one scattering layer in the same FOV is detected, only the first one (i.e. the highest) is considered, and its backscatter (extinction) profile is recorded into the CCD. This criterion allows the inclusion of the BSP of the upper layer of condensate into the CCD when conditions of multiple-layer clouds are found.

When all the conditions listed in Table 3.1 are met, the BSPs contained in the CPro file are copied in the CCD. Each selected profile is recorded together with the corresponding ancillary data taken from the CLay. Repetition of the same procedure for all the FOVs contained in the CPro files of year 2008 completes the CCD. The clouds contained in the CCD are simply referenced as cirrus clouds or cirri in what follows.

Some basic statistics concerning the frequency of occurrence of cirrus clouds selected for the CCD are given in Table 3.2. The table shows that, on average, cirrus clouds cover more that 30 % of ocean FOVs from 60° S to 60° N with a maximum in the tropical area. Similarly to what noted by Sassen et al. (2008), Martins et al. (2011) and Nazaryan et al. (2008) the occurrences are higher in the northern hemisphere than in the southern one. This feature is also found within the tropics where differences between the northern belt and the southern one are of the order of 10 %. Due to some differences in the selection criteria, the absolute values of the cirrus clouds frequency do not exactly match those found by previous authors; nevertheless the general features of the statistical ensemble are preserved, i.e., cirrus clouds during nighttime have higher occurrences in tropical areas and lower occurrences in the midlatitude belts with respect to what was found during daytime in the same areas, as in Nazaryan et al. (2008).

The main physical and optical characteristics of the cirrus clouds selected for the CCD are described by means of percentage distributions in Fig. 3.1 for tropics and midlatitudes and for nighttime and daytime separately. It is shown that at tropics the mean top altitude is 14.5 km during the day and 14.8 km during the night while at ML it is about 10.2 km and 10.4 km respectively for day and night. These values are in good agreement with those

found by Nazaryan et al. (2008) and Martins et al. (2011). The geometrical thickness distributions are highly peaked at 0.8 km at day and at around 1 km at night for both latitudes denoting the widespread occurrence of thin cirri. The mean thickness is larger during the night than at daytime with very similar values for both latitudes (about 2.1 km at night versus 1.6 km during the day). Distributions with higher and thicker cirrus clouds are then found during the night than at daytime. It is suggested that the nighttime-daytime differences might be related with the higher levels of daytime noise. In fact, if the backscatter signals near cloud top and base were below the noise level, the cloud boundaries detected by the algorithm will be closer to the center of the cloud than is actually the case. As a consequence, the detected cloud top heights will be lower and thicknesses smaller than is actually the case.The thickness distribution at tropics is in accordance with Martins et al. (2011) while at ML some differences are found, possibly due to the very stringent condition applied on cloud midlayer temperature (maximum at 233 K) by the cited authors. The OD distributions show the high predominance of optically thin cirrus clouds (especially during nighttime) and a monotonic and rapid percentage decrease from 10^{-3} to 2 optical depth. The lower-right panel of Fig. 3.1 shows the distributions of the midpoint cloud temperature. For the midlatitude case both day and night midlayer temperature distributions are almost equally spread around the mean value (226 K) while for the tropical case the distributions for night and day data show (again very similar and with a mean value of around 209 K) a higher degree of asymmetry and a longer tail toward the larger temperature with respect to the mode value.

3.2 Homogeneous Cirrus Cloud Database

Backscatter (and extinction) profiles contained in the CCD refer to cirrus clouds covering a wide range of vertical extents (from few hundreds m up to 8 km) and optical depths (from 10^{-3} to 2).

The cloud geometrical thickness is proportional to the integer number of the backscatter (or extinction) coefficient values used to describe the layer in the CPro files that have a vertical resolution of 60 m. On the other hand, the total layer optical depth influences the magnitude of the layer-backscattered signal. Since we are interested in deriving statistical features of the shape of the BSPs (and ETPs) and investigating if relations with some of the main atmospheric parameters (included cloud's OD and Δz) exist, data are sub-

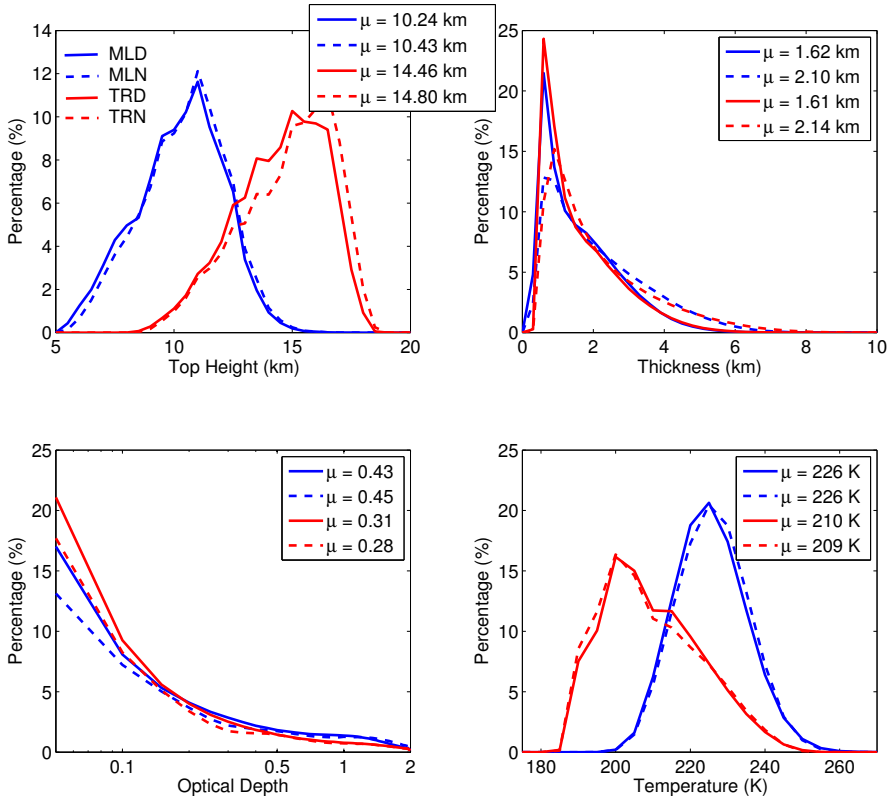

Figure 3.1: Top height (upper left panel), geometrical thickness (upper right), optical depth (lower left) and midlayer temperature (lower right) distributions for the cirrus clouds selected in the Cirrus Cloud Database (see Table 3.1). Midlatitude data are in blue and tropics in red. Dashed lines are for nighttime cirrus clouds (MLN and TRN) while solid lines are used for daytime (MLD and TRD). For each distribution the mean value μ is also reported. Lower left panel is in Logarithmic-Linear scale

jected to a process of rescaling and normalization. Thus a comparison among the shape of profiles, which originally would differ for the total amount of energy backscattered to the sensor and for the number of scattering levels, is made possible.

Moreover, a procedure that discards all the FOVs with non-uniform cirrus clouds geometrical features is also applied. The operation is performed to avoid the possibility that horizontal variations in cloud top and base altitude, within the 5-km resolution CALIOP data, might affect the averaging process of the shape of the BSPs.

The CALIOP parameter QC concerning the quality of the extinction retrieval (`http://www.calipso.larc.nasa.gov/resources/calipso_users_guide/data_summaries/layer/#extinctionqc_532`) is not utilized in this study. It is in fact demonstrated (detailed tests have been performed but results are not shown here) that the differences in mean BSPs obtained by averaging data of the HCCD with QC equal to 0 or 1 (highest quality retrieval) or alternatively with QC free to assume any possible value are of minor importance.

These operations, described in detail in the two following subsections, lead to the creation of a new database called the Homogeneous Cirrus Cloud Database (HCCD) over which the analysis of the BSPs (and ETPs) is performed.

3.2.1 Homogenization

With the term homogenization the operation of selecting cirrus clouds with horizontally homogeneous top and base altitudes is meant.

The 5-km horizontal resolution Level 2 data products (CLay and CPro) used in the present study are obtained by applying sophisticated algorithms (i.e. `http://www-calipso.larc.nasa.gov/resources/pdfs/PC-SCI-202_Part4_v1.0.pdf`, `http://www-calipso.larc.nasa.gov/resources/pdfs/PC-SCI-202_Part2_rev1x01.pdf`) to averaged Level 1, full resolution, attenuated backscatter profiles, in order to obtain high signal-to-noise ratios (SNR). Since horizontal inhomogeneities could introduce artifacts in the analysis of the shape of the BSPs, the non-uniform 5-km horizontal resolution FOVs are discarded from the database.

The criterion used to define the geometrical horizontal homogeneity within the 5-km horizontal resolution CALIOP FOVs is based on the analysis of cloud top and base height retrieval at higher resolution (i.e. 1 km). Cloud

top and base altitudes stored in the Level 2 CLay at 1-km horizontal resolution are collocated with the same products of the 5-km CLay files selected in the RD. For each 5-km FOV, the cloud top and base heights (z_t and z_b) are respectively compared to the mean cloud top and base heights ($\overline{z_t}_{1\,\mathrm{km}}$ and $\overline{z_b}_{1\,\mathrm{km}}$) obtained by averaging the five cloud top and base products of corresponding 1-km CLay files. The results are finally divided by the cloud thickness, as shown in the following equations:

$$\mathcal{Z}t = \frac{|z_t - \overline{z_t}_{1\,\mathrm{km}}|}{\Delta z} \tag{3.1}$$

$$\mathcal{Z}b = \frac{|z_b - \overline{z_b}_{1\,\mathrm{km}}|}{\Delta z} \tag{3.2}$$

It is assumed that a horizontally uniform cirrus cloud fills the observed 5-km FOV whenever both the conditions $\mathcal{Z}t < 0.1$ and $\mathcal{Z}b < 0.25$ are met. The condition on the cloud top homogeneity is more stringent than the one on cloud base since its derivation is performed on data with higher SNRs.

The number of profiles contained in the CCD and discarded after applying the requirement on the horizontal homogeneity is significant and corresponds to about 75 % at ML and 83 % at tropics, revealing that, on a 5-km horizontal resolution scale, less than one-fourth of cirrus clouds show homogeneous geometrical features.

3.2.2 Rescaling and normalization of Extinction and Backscatter Profiles

The rescaling process is obtained by using a linear interpolation. The original BSPs (and ETPs) are rescaled to a standard length of 60 points (I height indexes). This means that, regardless of the geometrical thickness of the cloud, the rescaled BSPs (ETPs) are described by 60 values of the backscatter (extinction) coefficient. The height indexes are equally spaced.

The backscatter coefficient at height index h, $\beta(h)$, assumes different values which are strongly correlated with the cloud-layer optical depth. A normalized backscatter coefficient, $\beta_n(h)$, is obtained by dividing the level-backscatter profile by the total area of backscatter profile (computed from cloud-base to cloud-top altitude). Since this operation is performed after the height rescaling at $I = 60$ equally spaced points, the total area is obtained by a simple summation. Using the trapezoidal rule the normalized backscatter

coefficient at level (height index) h is written as:

$$\beta_n(h) = \frac{\beta(h)}{\frac{\beta(1)+\beta(I)}{2} + \sum_{h=2}^{I-1} \beta(h)} \tag{3.3}$$

At this stage, normalized backscatter profiles from cirrus clouds with different ODs are comparable and stored in the final data set. In Fig. 3.2 an example of the normalization and rescaling process, for two randomly selected BSPs, is shown.

Along with the normalization procedure an additional data filtering process is applied to the database. The process is based on the analysis of $\beta_n(h)$. This quantity should be positive for all the 60 height indexes h, unless for data having a SNR smaller than 1 or for bad instrument calibration.

In this regard, BSP data derived from CPro files and selected in the CCD may show two kinds of problems: (1) profiles with some negative backscatter values and (2) profiles with some zero backscatter values between the cloud-top and cloud-base height. If one of the two cases occurs the profile is discarded from the final data set.

3.2.3 Statistical features of the Homogeneous Cirrus Cloud Database

The analysis of the shape of BSP is performed on the ensemble of $\beta_n(h)$ contained in the HCCD. The subscript n is omitted in the following, and for sake of simplicity, this quantity is called BSP. Since the shape of BSPs and ETPs is the same, only results concerning BSPs are shown. Cloud geometrical depths, BSPs (and ETPs) total areas (see Eq. 3.3) and all the other ancillary data are recorded in the final database, so that the original BSPs (and ETPs) might be reconstructed at any time.

The HCCD consists of about 1.5 million cirrus cloud cases: about 43 % of the total is found in the tropics and the remaining at ML (37 % in the ML South and 20 % in the ML North). In Table 3.3 the percentage of CALIOP FOVs selected for the HCCD, with respect to the total number of FOVs observed over the sea at the same latitudinal areas in 2008, is reported. Table 3.3 gives an idea of the occurrence frequency of horizontally homogeneous cirrus clouds over the ocean which are detected in approximately 8 % of the 5-km horizontal resolution CALIOP FOVs. Statistics for daylight and nighttime occurrence are also considered. With respect to those

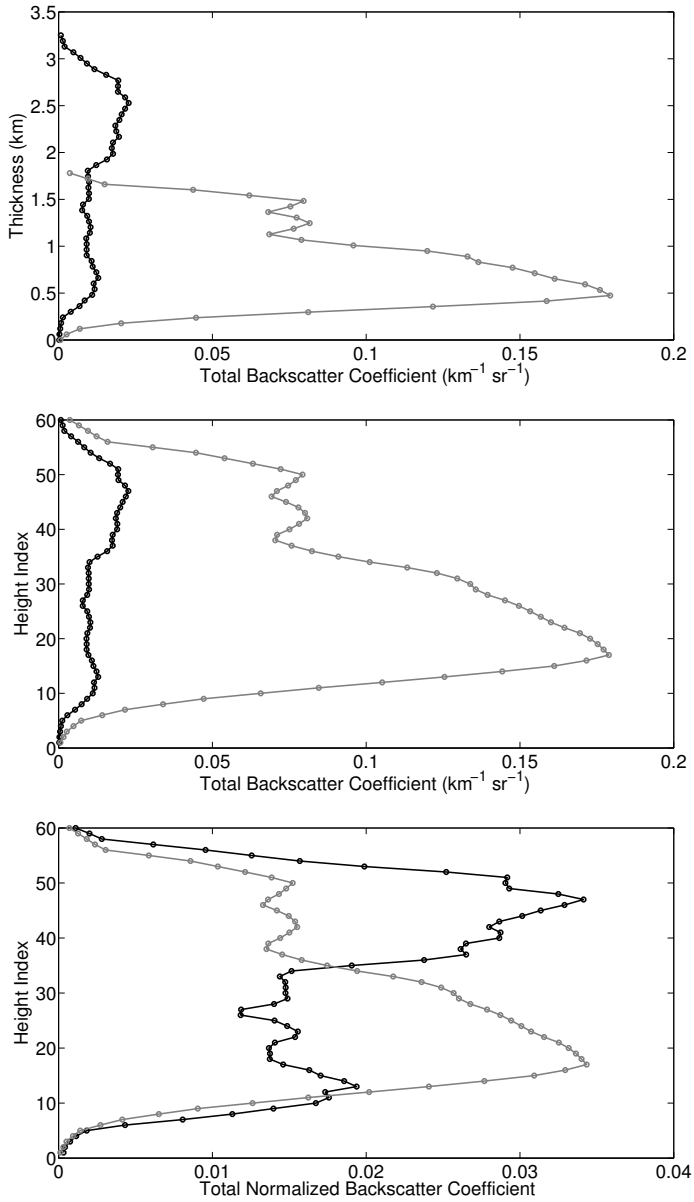

Figure 3.2: Pre-processing operations performed on two randomly chosen BSPs. Upper panel: CALIOP BSPs are compared without any manipulation. Middle panel: the backscatter profiles are rescaled to a standard number of points (60height indexes). Lower panel: the two BS profiles are normalized to unit area as functions of the height index.

reported in Table 3.2 and referring to the CCD (that concerns cirrus clouds in general), the occurrence frequencies reported in Table 3.3 are drastically reduced. In particular, high percentages of optically (and geometrically) thin cirrus clouds present in the CCD are excluded from the HCCD.

Table 3.3: Cirrus clouds cover obtained from the homogeneous cirrus cloud database, HCCD.

	Day	Night	Total
Midlatitudes North	8 %	10 %	9 %
Tropics	6 %	7 %	6 %
Midlatitudes South	8 %	9 %	8 %

This is also shown in Fig. 3.3, which highlights the general physical and optical features of the geometrically homogeneous cirrus clouds contained in the HCCD for tropics and ML and for day and nighttime separately. The frequency distributions of cloud top height (upper left panel) are very similar to those shown in Fig. 3.1. Only slight shifts toward higher altitudes at ML and toward lower altitudes at tropics for the HCCD are observed. The largest changes, with respect to what shown for the CCD, are found in the geometrical thickness and optical depth distributions. The occurrence frequencies of geometrically and optically thin cirrus clouds in the HCCD are strongly reduced with respect to what found for the CCD. The mean cloud Δz is 2.2 and 3.0 km for ML day and night respectively and 2.3 and 3.3 km for tropical day and night, which means at around a 50 % increase with respect to what was found considering all cirrus clouds. The ODs frequency distributions are also drastically changed and mean ODs are shifted to higher values (about 0.96 for ML and 0.83 for tropics). Some changes are also found in the midlayer temperature, which is increased (about 1 K for the ML and 6 K for the tropics) with respect to what found for the CCD.

In Table 3.4 some statistics concerning the occurrence of overlapped clouds are given for day and night. The table shows that, at midlatitudes, more than 50 % of the FOVs that are selected in the HCCD consists of non-overlapped clouds. The number increases at tropics and involves about two-thirds of clouds of the HCCD when day and night cases are considered together. Note that for the CCD the percentage of overlapped cirrus clouds is significantly higher (not shown here).

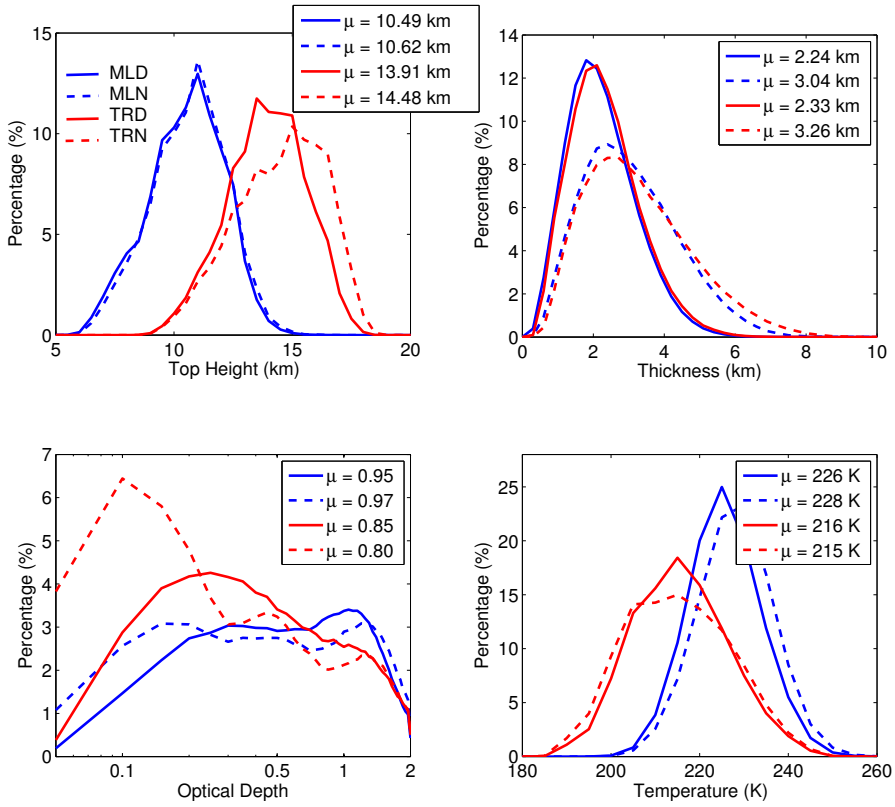

Figure 3.3: Same as in Fig. 3.1 but for the Homogeneous Cirrus Cloud Database (HCCD).

3.3 Statistical features of the two database

Table 3.4: Coud overlap in the HCCD.

# of layers in the FOV:	1	2	> 2
ML N day	66 %	20 %	14 %
ML N night	55 %	26 %	19 %
TRO day	70 %	20 %	10 %
TRO night	60 %	24 %	16 %
ML S day	62 %	22 %	16 %
ML S night	51 %	24 %	25 %

Chapter 4

Analysis of the CALIOP vertical backscatter profiles

A detailed statistical analysis of the shape of the BSPs is performed accounting for the whole HCCD (horizontally homogeneous cirrus clouds). The influence of cloud physical parameters (mainly geographical location, cloud optical depth, geometrical thickness and temperature) on cloud vertical features of the BSP is investigated. This requires the definition of a mean vertical BSP and, for each height index, a mean value of the backscatter coefficient is derived. Since the processes of averaging are performed on the full HCCD, which includes clouds with very different physical and geometrical properties, the problem of the shape of the distribution of data around the mean (for each altitude level) arises. For the present study, at each altitude level (height index), the definition of a mean backscatter (BS) value makes sense only if the data are approximately symmetrically distributed around a maximum value.

All the means obtained in this work are such that the distribution of the backscatter values at each height index is unimodal and approximately symmetric. As a consequence, a mean value of BS (at each level) can be defined unambiguously and used to derive the full average profile.

Definition of the Difference Index

To evaluate the results of the analysis, an index quantifying the distinction between two (mean) BSPs is also needed. A Difference Index, $\mathcal{I}_\Delta$, is then

defined as:

$$\mathcal{I}_{\Delta} = \frac{\sum_{h=1}^{I} |\beta(h) - \beta^{*}(h)|}{\frac{\beta(1)+\beta(I)}{2} + \sum_{h=2}^{I-1} \beta(h)} \cdot 100 \tag{4.1}$$

where $\beta(h)$ is a reference BSP and $\beta^{*}(h)$ is the BSP that has tobe evaluated against the reference one. I is again the total number of points along the cloud height (60). The difference index is preferred to other indexes (such as the squared differences) because of its simple interpretation. In fact, it represents the percentage value derived from the ratio of the area between the two BS profiles and the total area of the mean reference BSP. Equation (4.1) can be simplified noting that the denominator (that is the area of the reference BSP) is equal to unity, as a consequence of the normalization of all the profiles contained in the final database.

4.1 Annual and seasonal analysis

Due to appreciable differences found in the mean physical characteristics of cirrus clouds measured during night and daylight hours (Fig. 3.3), BSPs collected at nighttime and daytime are analyzed separately. Measurements obtained at midlatitudes and tropics are studied individually too.

Annual means of the shape of the BSPs are given as functions of the 60 height indexes: height index number 1 is cloud base and number 60 is cloud top. Results are plotted in Fig. 4.1 and show smooth curves with a single maximum BS value located close to cloud midlayer. Very similar profiles for tropics and ML, both at daylight and at nighttime, are observed, thus showing a minor influence of latitude on annual mean BSPs. Note that the distributions of geometrical thickness for homogeneous cirrus clouds at ML and at tropics are very similar while some differences are observed in the cloud top height, optical depth and temperature distributions (see back at Fig. 3.3).

In contrast, the differences between mean BSPs measured during the night (dashed curves in Fig. 4.1) and during the day (solid lines) are significant. A broader mean BSP shape in case of daylight cirri is observed with respect to nighttime. In terms of $\mathcal{I}_{\Delta}$ the differences are of the order of 10 % for both latitudes. Physical characteristics reported in Fig. 3.3 showed that the main differences between night and day distributions are found in the cloud geometrical thickness, suggesting a possible influence of this parameter on the shape of the CALIOP BSP.

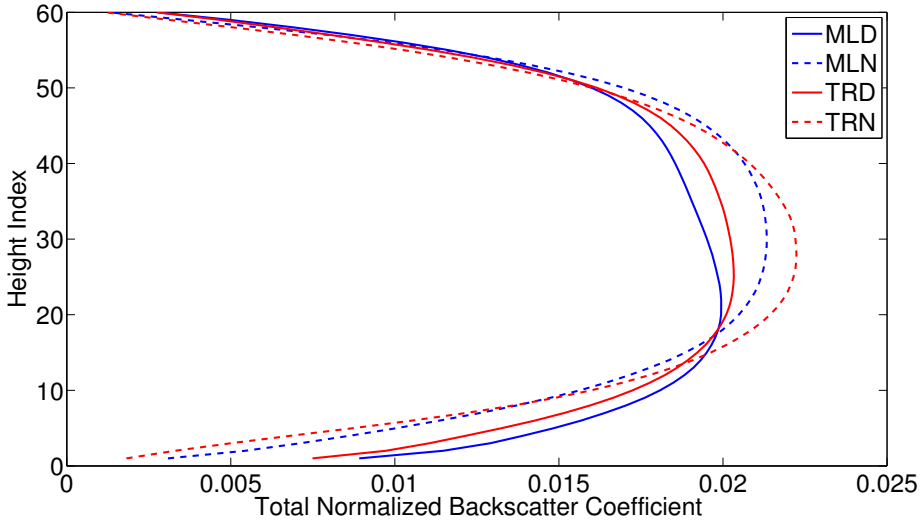

Figure 4.1: Annual mean backscatter profile for midlatitude (blue) and tropical (red) cirrus clouds at daytime (solid lines) and nighttime (dashed lines).

From Fig. 4.1 it is also observed that the mean value of the normalized BS coefficient measured at cloud base during night is lower than that measured during daylight hours. This result can be interpreted either as a CALIOP higher ability to detect cloud base during the night than day due to higher SNRs or as a physical signal that would mean that, on average, sharper cloud base edges are found during the day.

The averaging process is also applied to monthly data, around 25 000 cirrus clouds profiles per month. Results (not plotted here) show very little variability on the shape of the BSP with the period of the year. The maximum $\mathcal{I}_\Delta$ value found when monthly mean BSPs are compared to the corresponding annual means is less than 5.5 % at ML (North and South ML are studied separately in this regard to highlight the seasonal signal) and less than 2.7 % at tropics (for both North and South tropical belts).

Despite the small difference index, the two main climatic regions (ML and tropics) are studied separately in the next subsections that are focused on the investigation of possible relations among the shape of the BSP and cloud physical and thermodynamic parameters. Due to the minimal seasonal variability observed in monthly mean BSPs, all data presented in what follows

are averaged on a full year period.

4.2 Geometrical Thickness

In order to investigate the influence of the cloud geometrical thickness on the shape of the BSP, annual averages of the CALIOP BS are computed for six subsets of the HCCD regarding cirrus clouds with different vertical extensions (one interval every step of 1 km up to a value of 5 km and one interval for Δz larger than 5 km). The amplitude of the intervals is chosen so that at least 2000 profiles are selected for each subset. In Appendix A a methodology that derives the minimum number of profiles per subset, which is required to have a statistically relevant ensemble (for subsets of the whole HCCD), is described.

Results for midlatitudes and tropics are shown in Figs. 4.2 and 4.3 for nighttime and daytime respectively. It is observed that, for all the cases presented in the figures, the maximum of the BS profile is close to cloud top for thin cirrus clouds and moves towards cloud base as the cloud geometrical depth increases. For each panel of the figures, the difference indexes, which evaluate the diversity of each curve with respect to the mean BSPs (for midlatitudes and tropics and for night and day, as already shown in Fig. 4.1), are computed. Results show a great variability among the mean BSPs: $\mathcal{I}_\Delta$ is at maximum of about 38 % for midlatitudes and tropics during the night and 36 % during the day. The variability among mean BSPs of cirrus clouds of selected geometrical thickness intervals suggests a strong relation between cloud depth and the shape of the BSP.

The mean backscatter profiles plotted in Figs. 4.2 and 4.3 are analyzed as distributions along the height-index axis and their skewnesses are calculated. Results show that negative skewness values are found in case of night clouds with Δz less than 3 km both at tropics and ML, while positive ones are observed if the Δz is larger than 3 km. For the daylight case the geometrical vertical extent defining the ensembles with negative or positive skewness is 2 km both for midlatitude and tropical cirrus clouds. Note that a negative skewness value means a BS maximum placed in the upper part of the cloud while a positive one indicates a BS maximum in the lower part of the cloud.

Differences between BSPs of midlatitude and tropical data for cirrus clouds belonging to the same interval of geometrical thickness are minor but appreciable (difference indexes are about 6.5 % for daylight and 8.5 % for

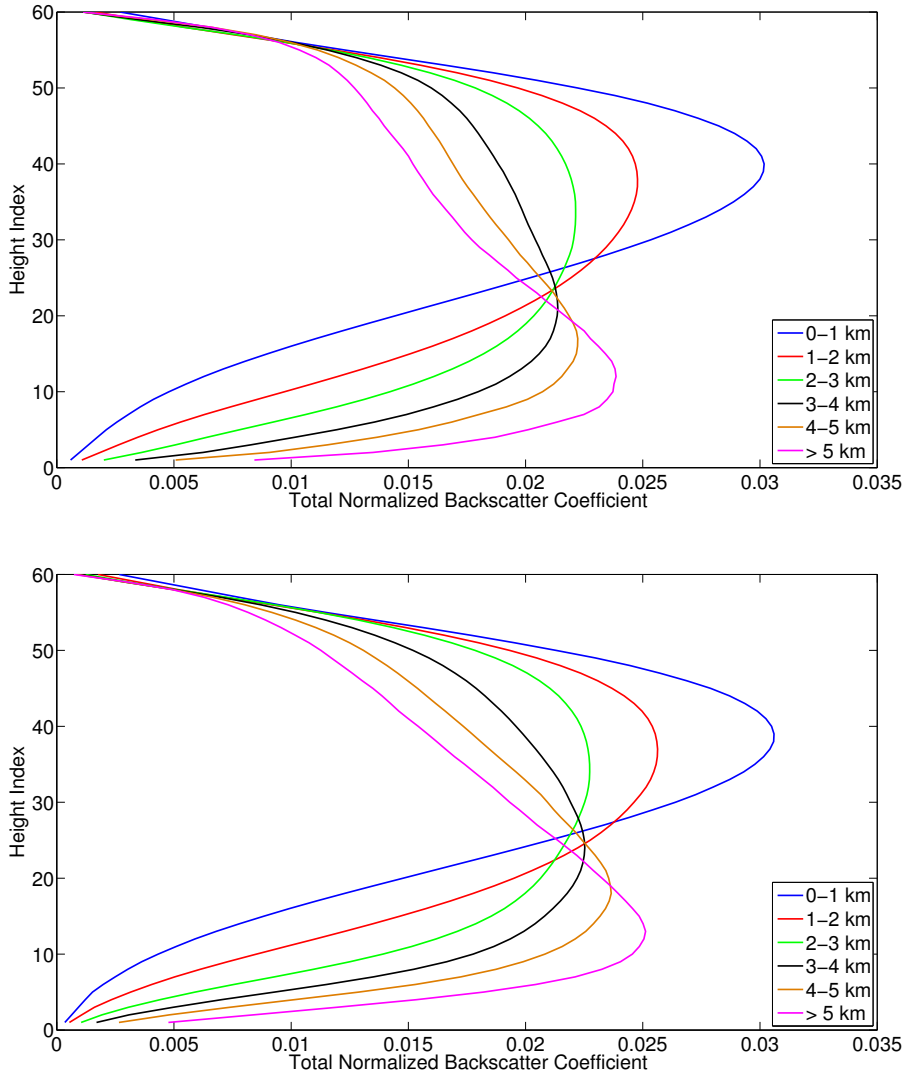

Figure 4.2: Cirrus clouds mean backscatter profiles for multiple thickness intervals. Data refer to nighttime. In the upper panel the backscatter profiles of midlatitude clouds are plotted as functions of height indexes. The lower panel shows profiles for the tropical case.

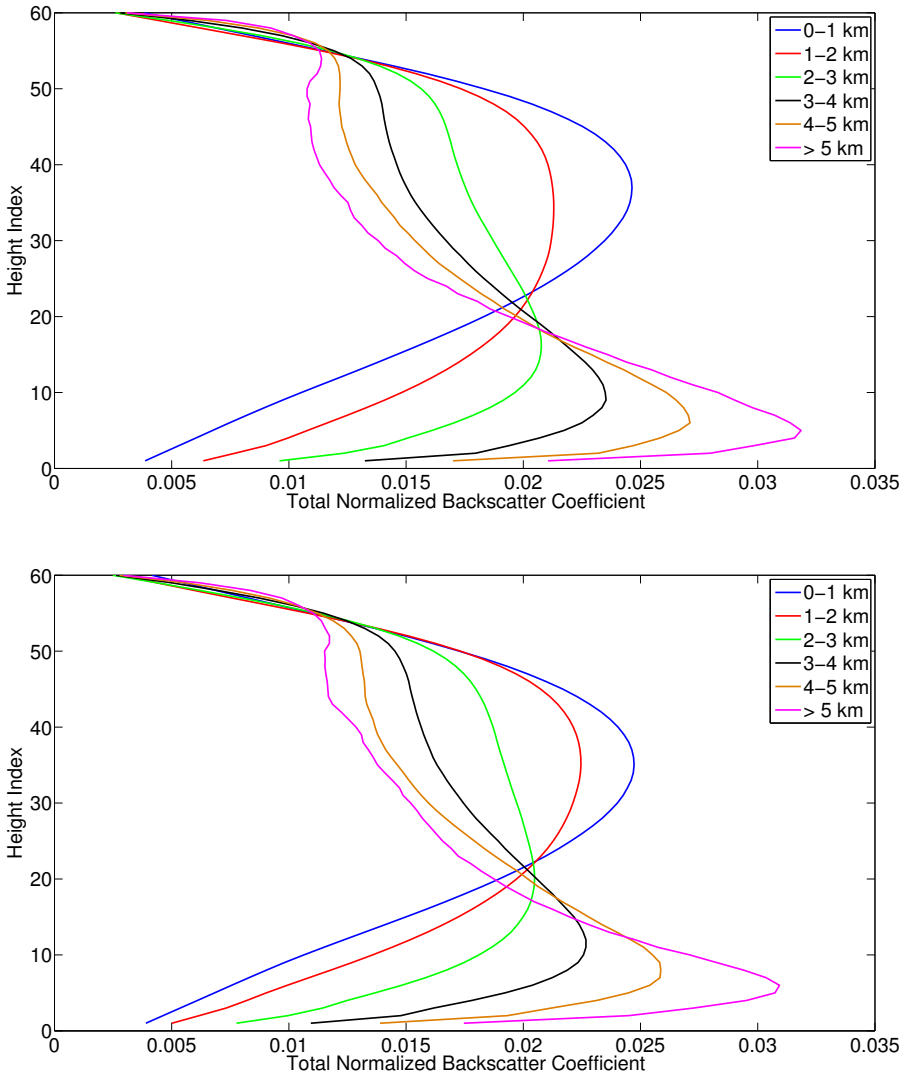

Figure 4.3: Same as Fig. 4.2 but for daylight hours.

nighttime data respectively). Differences of the same order of magnitude are found also when tighter intervals of geometrical thickness are considered (i.e. intervals of width of 0.5 km or less). Very narrow Δz intervals are used to avoid the possibility that different distributions of cloud depth within each interval might influence the results of the comparison among data collected at the two latitudes. The discrepancies found between midlatitude and tropical mean BSPs cannot, thus, be explained in terms of cloud geometrical thickness only and it implies that other parameters, characterizing differently midlatitude and tropical cirrus clouds, might influence the shape of the CALIOP BSP.

In our analysis only cloud bulk parameters, such as optical depth and temperature, are investigated while vertical variation of microphysical features (i.e., PSD or particles habit type) are not considered since no information is available for the cases analyzed in the present study. In this regard, note that, due to the environmental difficulties of collecting these kind of data, only rare and sparse measurements are accessible. Comparison between in situ data collected for tropical and midlatitude cirri show that PSDs measured in ice clouds associated with deep convection exhibit an exponential size distribution behavior, while, typically, midlatitude cirri display narrower PSDs (Baum et al., 2005a,b; Heymsfield and Miloshevich, 2003; Sassen et al., 2008). Nevertheless, it is the vertical variation of the PSD or of the particles' habit that might influence the shape of the BSP; unfortunately, in this regard, available data are few, for certain aspects in contrast among them and not easily interpretable in this context (Heymsfield and Miloshevich, 1995; Lawson et al., 2006). It is worth noting again that, in the CALIOP data processing, the lidar ratio is constant throughout a feature layer, meaning that variations of the PSD or the habit type are not accounted for.

Nighttime and daytime data show large discrepancies even when cirrus clouds within the same thickness interval are compared (dashed curves plotted in the panels of Fig. 4.2 with the corresponding solid lines plotted in Fig. 4.3). In this case the $\mathcal{I}_\Delta$ is of the order of 20 % for both latitudes. This again suggests that possibly different physical features characterizing the two cases might influence the shape of the BSP. The influence of optical depth and temperature on cirrus cloud BSPs is the topic of the next two subsections.

4.3 Optical Depth

Similarly to what was done for investigating the relation between cloud BSP shape and geometrical thickness, an analysis concerning the cirrus optical depth and the backscatter profiles shape is performed. The final database is divided into multiple subsets containing cirrus clouds with different τ. For each subset a mean BSP is computed at tropics and midlatitudes and for data collected during the night and day separately. Results (not shown here) are very similar to what obtained previously in the analysis concerning the geometrical thickness and BSPs relation. In fact, the maximum in the shape of the mean BS curve is close to the cloud top for clouds with very small τ and to the base for the optically thickest clouds of the ensemble (HCCD). In terms of skewness the BSP mean curves show negative values for OD values less than approximately 1.3 at night and 0.8 at day. Nevertheless, in the present analysis, the dependence between the cloud BSP shape and its optical depth is of minor intensity with respect to the one found for the geometrical thickness. In fact, $\mathcal{I}_\Delta$ computed for the mean BSP of each OD interval and the corresponding annual average is at maximum of 22 % (it was almost 40 % in the analysis concerning Δz). Furthermore, some exceptions are found to the rule describing the general behavior (BSP maximum moves toward cloud base as τ increases).

A correlation exists between cloud geometrical thickness and optical depth. An example of this is shown in Fig. 4.4 where cloud optical depth is plotted as function of cloud geometrical thickness for data collected in the tropical and midlatitude regions and during the day or at night (the four red and blue lines in the plot). The curves show a monotonic increase of the averaged OD value for any increase in the mean cloud Δz considered. The green line in the same figure is obtained for the whole FD without distinction between day and night or latitudinal belt. A parameterized formula that describes the green curve of Fig. 4.4 is given in Eq. (4.2):

$$\tau = a_1 \cdot \Delta z^b + a_2 \tag{4.2}$$

where $a_1 = -2.83$, $b = -0.1955$ and $a_2 = 3.28$.

The above τ-Δz relation simply parameterizes the mean OD value for a given cloud geometrical thickness when homogeneous and optically thin ($\tau < 2$) cirrus clouds are considered. Equation (4.2) holds for Δz varying from 0.5 to 5.8 km ($R^2 = 0.984$). The spread of the OD distribution around

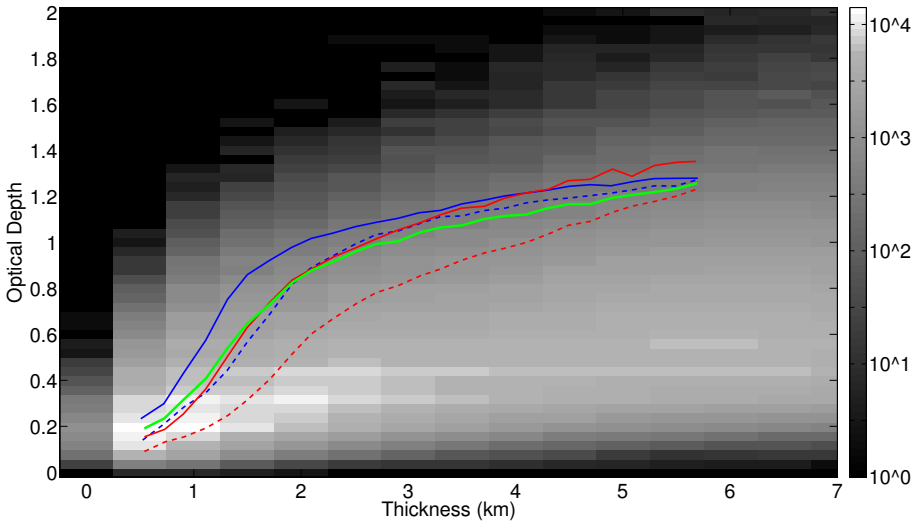

Figure 4.4: Optical depth of geometrically homogeneous cirrus clouds is plotted as a function of mean cloud geometrical thickness for ML (blue) and tropics (red) and for day (solid line) and night (dashed line). The green line is the weighted mean of the red and blue curves and represents the mean of the whole Final Database. The curves are plotted above the frequency of occurrence (in grayscale) for the FD as function of Δz and τ.

the mean for each geometrical thickness is provided by Eq. (4.3) ($R^2 = 0.973$):

$$\sigma_\tau = c_1 \cdot e^{d_1 \Delta z} + c_2 \cdot e^{d_2 \Delta z} \tag{4.3}$$

where $c_1 = 0.6138$, $c_2 = -0.0792$, $d_1 = -0.9944$ and $d_2 = -1.5090$.

In Fig. 4.4 the curves are superimposed on the frequency of occurrence of homogeneous cirrus clouds as function of the τ and Δz. The frequency of occurrence highlights the large number of cirrus clouds with geometrical depth between 1 and 4 km and gives an idea of the distribution of cirrus clouds OD as function of geometrical thickness and vice versa.

As a conclusion, since a relationship between mean BSPs and geometrical thickness exists it is plausible that also a relationship (even if weaker) exists between BSP shape and OD as a consequence of the $\tau - \Delta z$ dependence.

In order to verify that the shape of the BSP is mainly driven by cloud geometrical thickness and that the BSP-OD relation is only a second order effect, an analysis concerning the influence of OD value on the shape of the BSP must be applied to data from which the geometrical thickness dependence is removed (or at least limited). In this regard, the relation BSP-OD is investigated for cirrus clouds with nearly the same Δz but varying τ. In the upper panel of Fig. 4.5 the BSPs of midlatitude cirri during nighttime are computed for six optical depth intervals and for fixed geometrical depths (only clouds with vertical extension from 2.1 to 2.5 km are selected so that a large number of cases is accounted for). Results show a limited variability in the shape of the BSP with changing OD value. The largest value of $\mathcal{I}_\Delta$ found for the curves plotted in the upper panel of Fig. 4.5 is 15 %. It is observed that the maximum of the BSP curves slightly moves from top of the cloud toward the cloud base as τ increases. Also, the higher is the OD and the narrower is the distribution of the backscatter values around the maximum (and lower values near cloud top and base). This behavior is observed for both day and night profiles and for both the climatic regions.

As a comparison with the results shown in the upper panel of Fig. 4.5 the lower panel shows BSPs of midlatitude cirrus clouds at nighttime computed for varying geometrical thickness (six intervals) but nearly constant optical depth (0.8–1.0, so that the number of cases considered is maximized). It is demonstrated that a strong dependence between the shape of the BSP and the cloud thickness exists and that the maximum of the BSP curves shifts from cloud top to cloud base with increasing cloud geometrical depth. In this case the maximum $\mathcal{I}_\Delta$ among the curves is of 48 %. It is found that, for

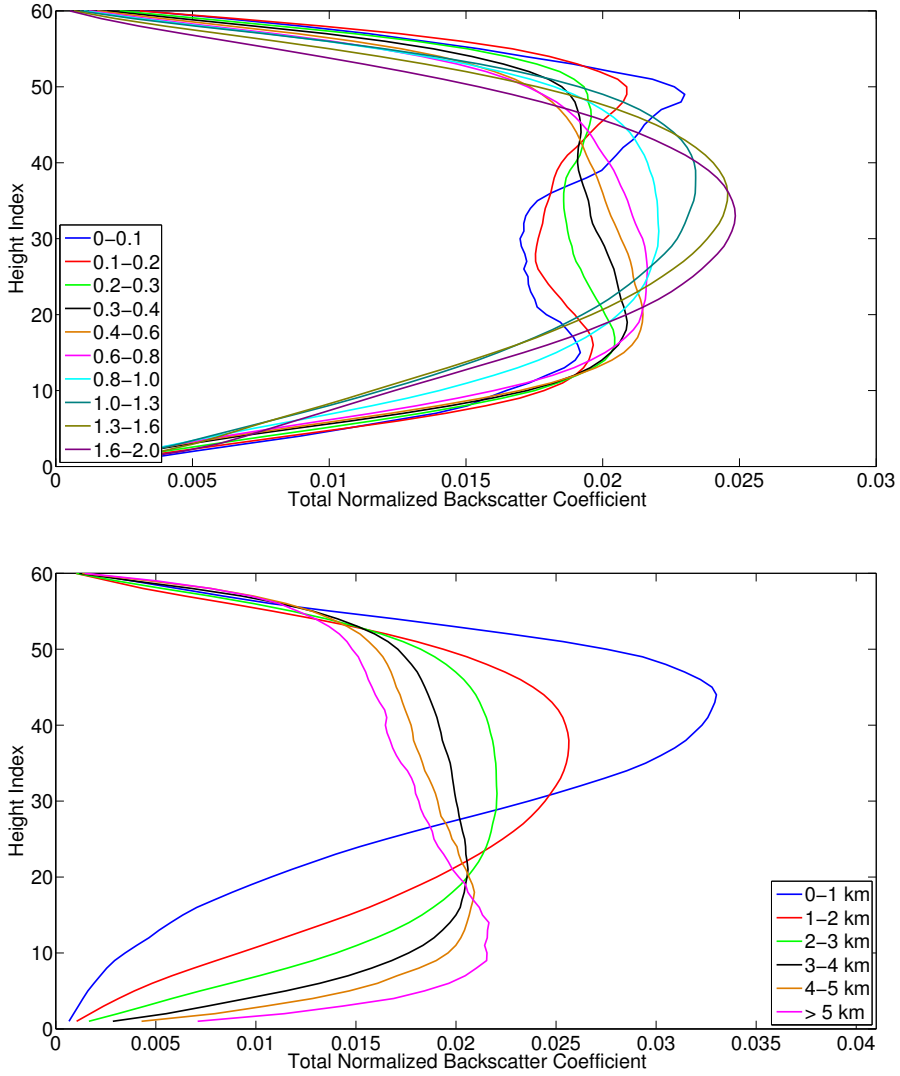

Figure 4.5: Upper panel: annual mean BSPs of cirrus clouds for varying optical depth and geometrical thickness between 2.1 and 2.5 km. Lower panel: annual mean BSPs for cirrus clouds with nearly the same optical depth (0.8–1.0) and multiple geometrical thicknesses. For both panels ML at nighttime are considered.

both latitudes and day and night, the difference indexes found when Δz is varied and τ is fixed are larger (by a factor between 1.5 and 3.2) than those found for varying optical depth intervals and fixed geometrical thickness.

Results show that the cirrus cloud optical depth has a smaller but appreciable influence on the shape of the BSP compared to geometrical depth.

4.4 Temperature

CALIOP Level 2 products contain temperature data derived from the GEOS-5 model and provided by the GMAO Data Assimilation System (`http://gmao.gsfc.nasa.gov/index.php`) which are exploited in the investigation of the influence of temperature on the shape of the cirrus clouds BSPs. An analysis of the effect of cloud temperature on BSP is performed by using the mid-layer temperature (or midpoint temperature) of the cloud that is defined as the temperature at the geometric midpoint of the layer in the vertical dimension (`http://www-calipso.larc.nasa.gov/resources/calipso_users_guide/data_summaries/layer/#layer_top_temperature`).

In Fig. 3.3 it was shown that similar distributions of midlayer temperature characterize diurnal and nocturnal data while some differences arise when latitude is accounted for, due to the higher tropopause at the tropical regions. Since a single temperature value is an acceptable approximation of the cloud temperature state only if geometrically thin clouds are considered, the analysis is limited to those clouds of the FD with vertical extension smaller than 2 km.

In Fig. 4.6 the annual mean BSPs for cirrus clouds with varying midlayer temperature is shown. Only the tropical case at daytime is considered since results are very similar for both regions and times of the day. Temperature intervals of 5 K are taken into account from 195 K to 245 K. Another interval comprises temperatures higher than 243 K and another one is for temperatures lower than 195 K. These last two intervals contain a very limited number of clouds. Results show that mean BSPs are only weakly dependent on temperature. It is observed that, on average, the maximum characterizing the backscatter coefficient normalized curve increases for a decreasing in the mid-layer cloud temperature (the BSP curve becomes more peaked). Some exceptions are anyway present. The effect is observed at both latitudes and at nighttime and daytime. The difference indexes ($\mathcal{I}_\Delta$) among the BSP curves of same latitude and time of the day (ML day, ML night, tropics day

and tropics night) but multiple midpoint temperatures have values that are mostly below 10 %.

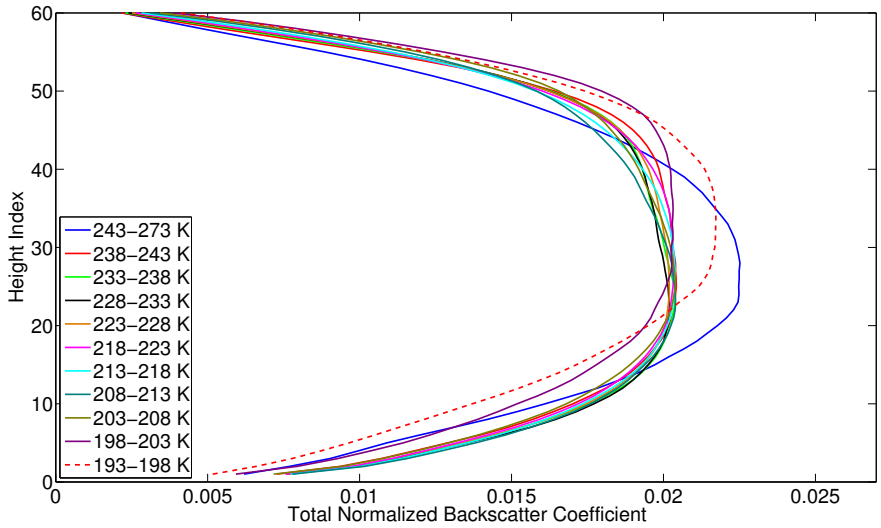

Figure 4.6: Mean BSPs for cirrus clouds with selected midlayer temperature intervals. Tropical regions at daytime are considered.

The above analysis cannot highlight possible variation in the shape of the BSP as a function of differences in the cloud temperature profile, but it only allows temperature to be considered as a bulk parameter.

In order to tackle possible effects of vertical temperature variations on the shape of BSP an investigation is performed which accounts for clouds with geometrical thickness between 4 and 4.5 km and analyzes separately cirri with large and small temperature gradients between the cloud top and bottom. For clouds with the above geometrical thickness the top and bottom temperature difference distribution is computed. Mean difference between cloud top and cloud bottom temperature is about 30 and 35 K respectively for ML and tropics. The cirrus clouds that fall below the first and above the third quartile of the top-bottom temperature difference distribution are compared for both latitudes and for day and night data separately. Results (not shown) do not highlight any significant temperature dependence except for a slight increase, in the daylight case, in the BSP maximum at the cloud base for data with the largest temperature gradient. The difference index

computed for BSPs with large and small temperature gradient is anyway very small and less than 8 % for all the situations considered.

It is thus concluded that the influence of temperature on the shape of mean BSPs, both at night and day, is of minor significance if compared to the effects related with the cloud geometrical thickness.

4.5 Fit of the profile

An analytical representation of mean BSPs measured by CALIOP is given, so that climatological shape of the BSPs of cirrus clouds in different conditions could be used by the reader.

The statistical analysis of BSPs has shown that the cloud geometrical thickness is the main parameter affecting the shape of the mean CALIOP BSP. It is found that a maximum in the mean BSP is placed near the top of the cloud for small Δz (less than 2 km at daytime and 3 km at nighttime) and moves towards the cloud base with increasing vertical extension. Also the cloud optical depth and temperature (even weakly) affect the shape of the mean CALIOP-measured BSPs. The main effect of these two quantities is to modify the intensity of the maximum of backscatter (relatively to levels near cloud base or top), which takes the highest values for the highest temperatures and the largest optical depths. Temperature and cloud optical depth produce second-order effects on the shape of backscatter profile and thus only the influence of cloud geometrical thickness is here considered.

Since the shape of BSPs for varying Δz shows very limited dependence on latitude (Figs. 4.2 and 4.3), only polynomial fittings for the day and night cases are provided.

Mean BSPs obtained for the night and day cases (tropics and midlatitudes are considered together) are fitted with analytical functions. The fitting function used is a two-variables (geometrical depth and height index), fifth-order polynomial:

$$\beta(\Delta z, h) = \sum_{j=0}^{4} \left(\Delta z + \frac{p_{0j}}{p_{1j}} \right) p_{1j} h^j + p_{05} h^5 \tag{4.4}$$

where the h variable assumes integer values from 1 to 60 and describes the vertical variation of β for a cloud with geometrical thickness equal to Δz. Thus, given the cloud top altitude (z_t), the quantity derived in Eq. (9) describes a cirrus cloud normalized BS at height z. The altitude z is simply

Table 4.1: Polynomial coefficients for mean backscatter profiles fitting (Eq. 4.4).

Coeff.	Day	Night
p_{00}	-7.2×10^{-3}	-4.5×10^{-3}
p_{01}	2.2×10^{-3}	5.37×10^{-4}
p_{02}	-5.46×10^{-5}	5.57×10^{-5}
p_{03}	6.37×10^{-7}	-1.69×10^{-6}
p_{04}	-2.17×10^{-10}	1.55×10^{-8}
p_{05}	-7.98×10^{-11}	-7.86×10^{-11}
p_{10}	6.6×10^{-3}	1.5×10^{-3}
p_{11}	-2.53×10^{-4}	5.69×10^{-4}
p_{12}	-9.16×10^{-6}	-4.17×10^{-5}
p_{13}	3.36×10^{-7}	1.04×10^{-6}
p_{14}	-2.31×10^{-9}	-6.92×10^{-9}

derived from:

$$z = z_t - \Delta z + \frac{h-1}{59}\Delta z \tag{4.5}$$

In Table 4.1 the polynomial coefficients for the fit of the mean BSPs of night and day cirrus clouds are given. The fit is such that in any case the $\mathcal{I}_\Delta$ computed for the analytical and climatological mean BSP curves is less than about 6 %.

4.6 From mean backscatter profiles to ice-water-content profiles

One of the important aspects of computing mean BSPs lies in the strict relation between the profile of the backscatter (and extinction) coefficient and the distribution of ice mass along the cloud vertical dimension. The IWC profile largely affects the cloud weighting function and it is thus fundamental for the derivation of the radiative fields and the computation of the energy balance of cloud layers (Maestri and Rizzi, 2003a). Hence, climatological information on IWC vertical distribution can potentially improve both the radiative forward models simulations of cloudy fields and inversion algorithms dedicated to the retrieval of cloud properties.

In this regard, the radiative impact of using IWC derived from the mean measured BSPs instead of vertically constant IWC is evaluated for a simple and typical case. Before that it is shown that, under certain conditions, which represent a fairly good approximation of reality, proportionality between the vertical profiles of the backscatter coefficient and the IWC profile exists. If this is the case, the mean BSPs (i.e. the fitting functions described in Eq. 4.4) can be exploited in forward or inverse radiative transfer models to define the distribution of the ice mass along the cloud vertical dimension thus providing a more realistic description of the cloud structure.

More importantly, the dependence of BS coefficient due to particle size variation is less than that due to IWC. As an example we have computed (not shown here) the backscatter coefficient of a mixture of particles such as that reported in Bozzo et al. (2008), which is typical of midlatitude cirri. The effective dimensions used span the 16–300 μm range. Results show that the minimum and maximum of the backscatter coefficient are within a factor of four. That means that the effect of particles size fluctuations along the vertical on BS coefficient is of second-order importance with respect to variations in the IWC which, on the other hand, can affect the same radiometric parameter up of several orders of magnitude. This supports the assumption that the shape of the PSD is constant along the cloud thickness in the context of the present research.

For each cloud layer (identified by its height z_i), the particulate backscatter coefficient of an air volume (or volume particulate backscatter coefficient, $\beta(z_i)$, [(m^{-1} sr^{-1})]) can be written as:

$$\beta(z_i) = \int_{r_{\min}}^{r_{\max}} P(\pi, r) \cdot \sigma_{sca}(r) \cdot n(r, z_i) dr \tag{4.6}$$

where $P(\pi, r)$ is the value of the phase function of the particle with effective dimension r at a scattering angle of 180 degrees, $\sigma_{sca}(r)$ is the particle scattering cross section [m^2] and $n(r, z_i)$ is the particle size distribution [#/(m^3 m)] at level z_i with a total particle number concentration equal to $N(z_i)$ [#/m^3].

Considering the scattering cross section per unit mass (i.e., the particle-mass-scattering cross section $k_{sca}(r)$ [$\mathrm{m}^2\,\mathrm{kg}^{-1}$]) a mean mass-scattering cross section can be defined as:

$$\overline{k_{sca}} = \frac{\int k_{sca}(r) n(r, z_i) dr}{\int n(r, z_i) dr} \tag{4.7}$$

where the integration is performed over all the particles effective dimensions. Under the assumption of having the same PSD shape in all the cloud layers (i.e. $n(r, z_i)/N(z_i)$ does not depend on z_i), the mean mass scattering cross section becomes a layer independent quantity. For the same conditions, it is possible to define a mean phase function at the backscattering angle:

$$\overline{P(\pi)} = \frac{\int P(\pi, r) \cdot k_{sca}(r) \cdot n(r, z_i) dr}{\int k_{sca}(r) \cdot n(r, z_i) dr} = \frac{\int P(\pi, r) \cdot k_{sca}(r) \cdot \frac{n(r, z_i)}{N(z_i)} dr}{\overline{k}_{sca}} \quad (4.8)$$

which is also a layer independent quantity. Similarly, a mean scattering cross section is defined as:

$$\overline{\sigma_{sca}} = \frac{\int \sigma_{sca}(r) n(r, z_i) dr}{\int n(r, z_i) dr} \quad (4.9)$$

Thus the (volume) backscatter coefficient is re-written in terms of mean quantities:

$$\beta(z_i) = \overline{P(\pi)} \cdot \overline{\sigma_{sca}} \cdot N(z_i) \quad (4.10)$$

Since a simple relation between the mean scattering cross section ($\overline{\sigma_{sca}}$) and the total ice-water-content of the i-th layer (i.e., IWC(z_i) [kg m^{-3}]) exists:

$$\overline{\sigma_{sca}} = \frac{\overline{k_{sca}} \cdot \mathrm{IWC}(z_i)}{N(z_i)} \quad (4.11)$$

the volume backscatter coefficient of the i-th layer is written as:

$$\beta(z_i) = \overline{P(\pi)} \cdot \overline{k_{sca}} \cdot \mathrm{IWC}(z_i) \quad (4.12)$$

At visible wavelengths, the single scattering albedo of a distribution of pristine ice crystals is equal to one and the mass-extinction cross section $k_{ext}(r)$ can be used in place of $k_{sca}(r)$. The volume backscatter coefficient is then:

$$\beta(z_i) = \overline{P(\pi)} \cdot \overline{k_{ext}} \cdot \mathrm{IWC}(z_i) \quad (4.13)$$

The cloud total optical thickness, τ, as a function of the ice-water-content is:

$$\tau = \sum_{i=1}^{n} k_{ext}(z_i) \cdot \mathrm{IWC}(z_i) \cdot \delta z_i \quad (4.14)$$

where δz_i is the geometrical depth of the i-th cloud layer.

Using the definition of Ice-Water-Path (namely the ice content in the whole cloud depth, $[\mathrm{kg\,m^{-2}}]$):

$$\mathrm{IWP} = \sum_{i=1}^{n} \mathrm{IWC}(z_i) \cdot \delta z_i \tag{4.15}$$

and recalling the assumption of having the same PSD shape at each cloud layer, the optical thickness is:

$$\tau = \overline{k_{ext}} \cdot \sum_{i=1}^{n} \mathrm{IWC}(z_i) \cdot \delta z_i = \overline{k_{ext}} \cdot \mathrm{IWP} \tag{4.16}$$

Using Eq. (4.13) and Eq. (4.16) it is easily found that:

$$\mathrm{IWC}(z_i) = \frac{\mathrm{IWP}}{\tau \cdot \overline{\overline{P(\pi)}}} \cdot \beta(z_i) \tag{4.17}$$

Equation (4.17) highlights that a (linear) proportionality exists between the backscatter coefficient and the IWC when the PSD shape (and same particle mixture of habits and orientation) is assumed constant along the cloud vertical extent. The constant of proportionality depends only on total ice content and optical thickness (bulk properties) and on the mean phase function at the backscattering angle. Thus, climatological IWC profiles can be derived by exploiting the polynomial functions given in the previous section.

Chapter 5

The COBRA Experiment

A better knowledge of the vertical properties of clouds, can lead to better results when both forward and inverse radiative transfer calculations are performed. In this sense, the work described in the previous Chapter can be considered the first step of a more detalied study of the ice clouds. This Chapter discusses some of the issues that are encountered when dealing with radiative transfer in presence of cold clouds in the infrared and FIR, using spectrally resolved infrared data extending to the FIR measured at the surface of an Alpine mountain site (Testa Grigia, 3480 m a.s.l.) in Northern Italy.

The content of this Chapter is the result of a work in cooperation with L. Palchetti and G. Bianchini of the Institute of Applied Physics "Nello Carrara" – CNR in Florence and P. Di Girolamo, G. Masiello, C. Serio and D. Summa of the school of engineering of the Università degli Studi della Basilicata and will be submitted in the near future.

5.1 Radiative Transfer Simulations in the FIR and the Role of Scattering

5.1.1 Scattering and Absorption Processes in the FIR

In the spectral region between 800 and 1000 cm^{-1} radiative transfer in presence of ice crystals is mainly driven by absorption and emission processes, whilst scattering plays a minor, though not negligible, role. This spectral region has been in fact frequently exploited for cloud studies by satellite

and ground based remote sensing sensors. In particular, information about the optical depth and effective dimensions are derived from high spectral resolution measurements that exploit the large radiance sensitivity to cloud parameters in the main atmospheric window (i.e. Maestri and Holz, 2009).

The minimum in the absorption coefficient of ice at around $450\,\mathrm{cm}^{-1}$ opens new perspectives for the remote sensing of ice clouds since, as already mentioned in the introduction, the optical properties of ice crystals show that scattering effects become significant in the FIR.

Due to the reduced opacity, in fact, the radiance signal originates deeper within the cloud (i.e. lower in the atmosphere for a satellite viewing point) compared to typical IR wavenumbers (i.e. 600–$2600\,\mathrm{cm}^{-1}$) and therefore additional information is possibly available. For the same reason, the FIR channels might be potentially very useful to derive optical features of clouds with large optical depths. Naud et al. (2001) states that "the FIR bands ($410\,\mathrm{cm}^{-1}$ and $550\,\mathrm{cm}^{-1}$) present a serious advantage for particle size identification in thick clouds [...] and they can characterise large particles better than 11-12 μm". Along the same line of research Yang et al. (2003) shows that for ice clouds whose optical depths is larger than 8, the brightness temperature difference between 250 and $410.2\,\mathrm{cm}^{-1}$ is sensitive to the effective particle size.

The sensitivity to crystal habit can be easily computed in the IR main window by keeping fixed the total cross sectional area of the crystals within the PSD, since radiative transfer is mainly driven by emission/absorption processes. In the shortwave band (SW) the radiance sensitivity can be evaluated by keeping fixed either the total IWC or the cloud OD since scattering is dominant. However the evaluation of radiance sensitivity to crystal habits in the FIR is a particularly difficult problem since both absorption and scattering play an important role and, in addition, radiance is strongly affected also by the water vapor profile.

To evaluate the relative importance of scattering and absorption in our geometry, a set of radiative transfer simulations is performed. The atmospheric parameters are those measured during the field experiment, that are described later in the text. Three different effective diameters are used to define the particle size distributions (PSD), but all have same cloud optical depth, equal to 1.3 at $900\,\mathrm{cm}^{-1}$. The downwelling radiance at the surface over the REFIR-PAD spectral coverage is computed in two ways: in the first case (F solution) scattering is fully accounted for, within the cloudy layers; in the second case (Absorption approximation, A) the radiative transfer within

the cloud is performed considering the gaseous and crystals emission/absorption processes only. The difference (at the REFIR-PAD resolution) between the F solution and the A approximation is an estimate of the importance of the scattering processes as discussed by Maestri and Rizzi (2003b). Results in terms of BT absolute difference and radiance percentage differences are shown in Figure 5.1. Both panels highlight the importance of scattering in the FIR, and indicate that the differences generally increase as the effective diameter of the PSD decreases.

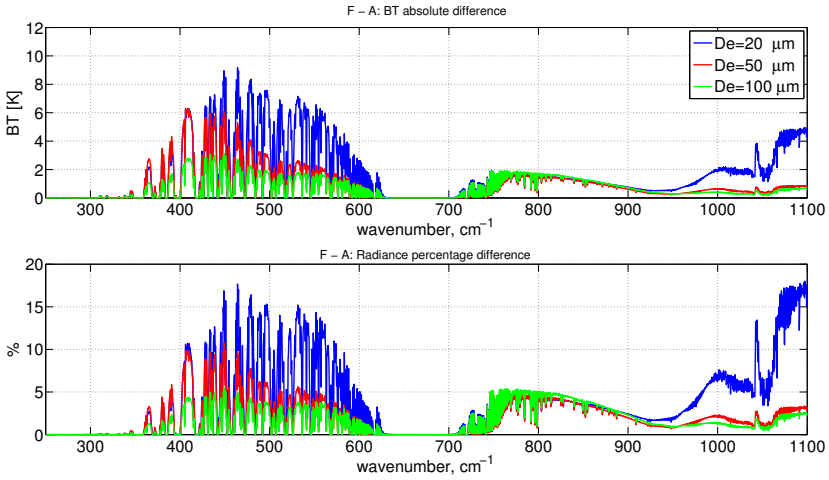

Figure 5.1: Spectral absolute BT difference and radiance percentage difference for the F and A type of simulations (see text for details) in presence of three different types of PSD within the cirrus cloud with IR optical depth 1.3. The solution is for downwelling radiance at the ground.

It is also clear that differences are only weakly dependent on the assumed PSD in the 800–1000 cm^{-1} interval, which means that the spectral features of the radiance field in that spectral interval are driven by the absorption processes as explained by Maestri and Holz (2009). Finally, the large deviations in the FIR imply that spectral radiances can be potentially very useful to derive additional information on the PSD.

5.1.2 On the reconstruction of the scattering phase function of ice crystals in the IR

When scattering processes play a relevant role, the description of the ice particles phase function must be accurate.

Both the forward (RTX) and inverse (RT-RET) models used in the present work are based on a doubling and adding algorithm (see for example Evans and Stephens (1991)) to simulate the multiple scattering effects within the clouds. This kind of algorithm requires the description of the particles phase function through a truncated series of Legendre polynomials (i.e. Liou (1992)). Examples of scattering phase functions for a PSD composed of a mixture of habits, as defined by Bozzo et al. (2008), are given in Figure 5.2, upper panel. The sequence of Legendre coefficients is plotted in the lower panel. The largest coefficients are those that mostly contribute to the reconstruction of the phase function through the Legendre series. Their number becomes larger with increasing wavenumber and PSD effective dimension. In case the effective dimension is of the order of 120 μm the number of the Legendre coefficients significantly different from zero is much larger than 60 for any of the wavenumbers considered in the study. All the computations of the

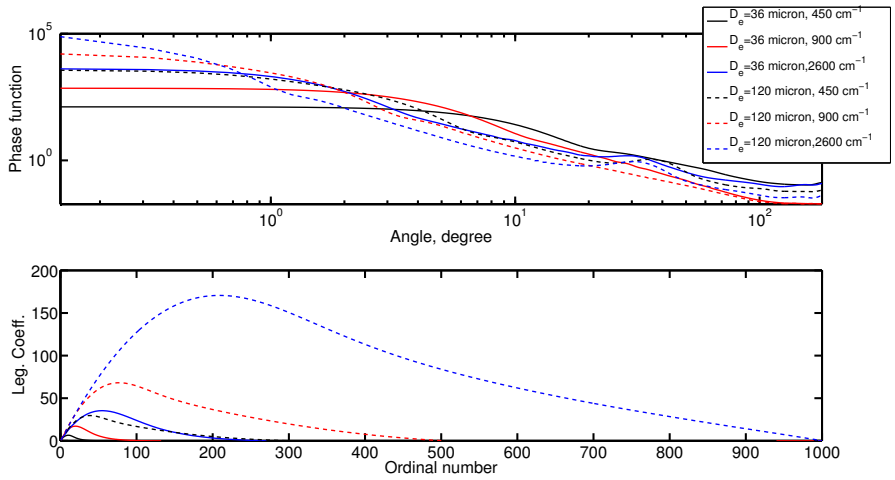

Figure 5.2: Upper panel: Example of phase functions at three different IR wavenumbers and for two different types of PSD composed of a mixture of ice habits as reported in the text. Lower panel: Legendre expansion coefficients of the corresponding phase functions.

Legendre coefficients shown here and used for the radiance field simulations are done assuming phase functions that are defined on a gaussian integration grid of 36 000 points. The definition of the phase function at a very high angular resolution allows stable computations of the highest order Legendre coefficients that otherwise would be affected by numerical instabilities (i.e. in case low angular resolution such as every 0.1 degree is assumed).

At solar wavelengths (not shown here) the forward peak of typical ice crystals phase functions is mostly confined within few tenth of one degree around the forward (0°) scattering angle. To improve the representation of the phase function, methodologies like Potter (1970), the delta-M method (Wiscombe, 1977) that modify the phase function peak, and the extinction and scattering coefficients, are often applied. In the IR, the phase function forward lobes are generally much broader than at short wavelengths. Nevertheless, the range from the highest peak to the deepest trough spans several orders of magnitude, especially for large particles, making the phase function representation still complicated. Methodologies like the delta-M method quoted above cannot be rigorously applied in the IR, due to the wide forward lobe of the phase function. Thus, the correct description of the scattering processes relies on the use of a large number of Legendre coefficients (nc). This 'rule' has not always been followed, as the scattering processes have been often considered of lesser importance, and generally infrared high spectral resolution computations are performed using 65 or less Legendre coefficients.

The value of nc defines the distance of the reconstructed phase function from the original one. An example is reported in the upper panel of Figure 5.3 which shows the percentage difference between the original phase function of a PSD with D_e=120 μm at 450 cm^{-1} and the reconstructed ones using various nc. The largest discrepancies are obtained for $nc = 61$ and are highly oscillatory. For each nc value the largest relative differences are found at 180°, i.e. at backscatter, while largest absolute differences are found in the forward peak for all cases. In the lower panel of the same Figure (5.3) the mean over angle percentage differences are shown for PSDs with effective dimensions of 36 and 120 μm, at 450 cm^{-1} (dirty window in the FIR) and at 900 cm^{-1} (in the main IR window where usually cloud properties are retrieved). In all cases the mean differences decrease (or stay approximately the same) as nc increases. Within radiative transfer codes, nc is related to the number of zenith angles for each hemisphere (nz) at which the radiance integrations are performed. In case a Gauss-Legendre quadrature is used the relation is: $nc = 4 \cdot nz - 3$. The time required to compute the radiance/flux solution increases rapidly

with nz, and a compromise between accuracy and computational time is needed.

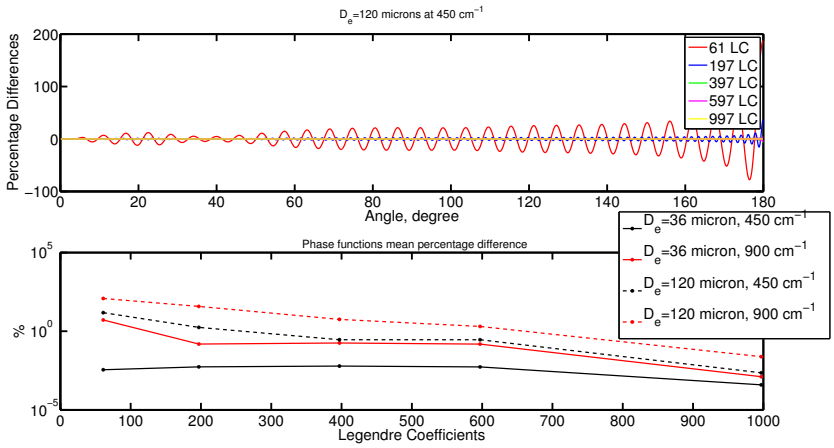

Figure 5.3: Upper panel: percentage differences between the original phase function and phase functions re-constructed by using a truncated Legendre series with a varying number of Legendre coefficients. The case of a PSD with D_e=120μ m at 450 cm^{-1} is shown. Lower panel: All angles mean percentage differences between original and reconstructed phase function as function of the number of Legendre coefficients used. Four different combinations of PSDs and wavenumbers are shown as reported in the legend.

In search of a relationship between downwelling radiance and nc, various simulations are performed for a cloud with an optical depth of 1.3, same PSDs and wavenumbers used in the lower panel of Figure 5.3. The simulation using $nc = 997$ ($nz = 250$) is assumed to be the reference. The absolute difference between the results for various nc and the reference is shown in Figure 5.4.

Largest discrepancies of the order of 0.1 mW/(m^2·sr·cm^{-1}) or about 1 % of the signal, correspond to the smallest number of Legendre coefficients used which, in our example, is $nc = 61$. The discrepancies decrease with increasing nc, and for 397 coefficients (100 zenith integration angles) the discrepancy between the reference simulation is less than 0.05 % for all cases. Note that (as it will be described in paragraph 4) the radiometric error of REFIR-PAD is in the range 0.1–4.0 mW/(m^2·sr·cm^{-1}) in the 200–1100 cm^{-1} spectral interval.

Typically IR high spectral resolution radiative transfer computations are

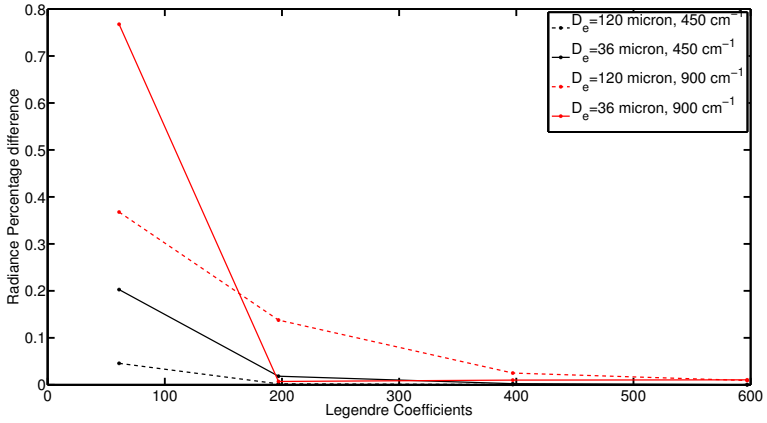

Figure 5.4: Absolute difference in the downwelling radiance at the ground between simulations made using a variable number of Legendre coefficients for the reconstruction of the phase function and the reference simulation obtained exploiting 997 Legendre coefficients. Two wavenumbers are shown: 450 and 900 cm^{-1}.

run using $nz = 16$ which means 61 coefficients are used for the phase function reconstruction. From what is shown, this number is insufficient for accurately describing ice crystals when downwelling radiance computations and non-opaque clouds are considered, since the signal arriving at the sensor originates almost entirely from the (colder) cloud body and from backscatter of the (warmer) surface emitted radiance.

The differences shown in Figure 5.4 are strictly dependent on the atmospheric and cloud properties used. In particular the percentage values increase for clouds with optical depths in the range 0.6–1.2 and for dry atmospheric conditions.

In order to limit the code computational errors to less than few tenths of the radiometric error all the simulations performed in this study will be done using 397 Legendre coefficients.

5.2 Experiment/Field campaign

As already mentioned into the introduction section, despite the great impact of the fundamental rotation band of H_2O in the far infrared on the Earth

energy budget and climate (Clough et al., 1992; Mertens et al., 1999)), the spectral range 17 to 50 μm of the atmosphere infrared emission was largely unexplored until recent years (Tobin et al. (1999, 1996)).

In order to fill this lack, the Earth COoling by WAter vapouR emission (ECOWAR, Bhawar et al. (2008)) campaign was set up, which took place in the Italian Alps in March 2007. This campaign allowed us to observe the emitted atmospheric infrared emission in the widest spectral range ever measured before and opened up the way to a more vigorous period of field experiments in the far infrared (Delamere et al., 2010; Green et al., 2012; Turner and Mlawer, 2010).

5.2.1 Instrumental Set-Up

The experimental set up of the ECOWAR campaign has been presented and discussed into details in Bhawar et al. (2008). For the benefit of the reader, here we limit to summarize what is important for a proper understanding of the present work.

The campaign took place in the Italian Alps from 3 to 17 March 2007 in two measurement sites approximately 7 kilometres apart: Cervinia (45°56′ N, 7°38′ E, 1990 m); Testa Grigia (45°56′ N, 7°42′E, 3500 m).

Two far infrared spectrometers were deployed at the campaign site, which were capable of measuring atmopsheric spectral radiance within the spectral region 17 to 50 μm with a sampling rate better than 0.5 cm^{-1}. The Interferometer for Basic observations of the Emitted Spectral radiance of the Troposphere (I-BEST) (Serio et al. (2008a)), was operated from Cervinia, whereas the Radiation Explorer in the Far InfraRed - Prototype for Applications and Development (REFIR-PAD) was operated from Testa Grigia.

In addition, in order to properly characterize the thermodynamic state of the atmosphere, ancillary information were measured by : 1) a conventional radiosonde system, VAISALA system (RS92k sonde); 2) a Raman Lidar capable of simultaneously getting temperature, water vapor, aerosol and clouds optical properties (e.g., see Section 5.2.3); 3) a Ground-Based Millimeter-wave Spectrometer (GBMS, Fiorucci et al. (2008)) for observations of precipitable water vapor (PWV). The Radiosonde and the Lidar systems were located at Cervinia station, while the microwave radiometer was deployed at the Testa Grigia Station.

The analysis shown in this paper refers to the REFIR-PAD observations. For this reason more details of this instrument will be shown on purpose in

section 5.2.4. Next section is devoted to how the thermodynamical atmospheric state was determined and colocated with REFIR-PAD observations.

5.2.2 Atmospheric state determination

The atmospheric state vectors co-located with REFIR-PAD observations have been build up using the temperature and water vapor radiosonde profiles. In addiction, we also used the precipitable Water vapor measured by GMBS.

During the morning of the 9 March 2007, two radiosondes were launched from Cervina station. The first was launched at 9:01 GMT and it flew until 10:29 GMT (see Fig. 5.5). The second radiosonde was launched at 11:19 GMT and flew until 12:50 (see again Fig. 5.5).

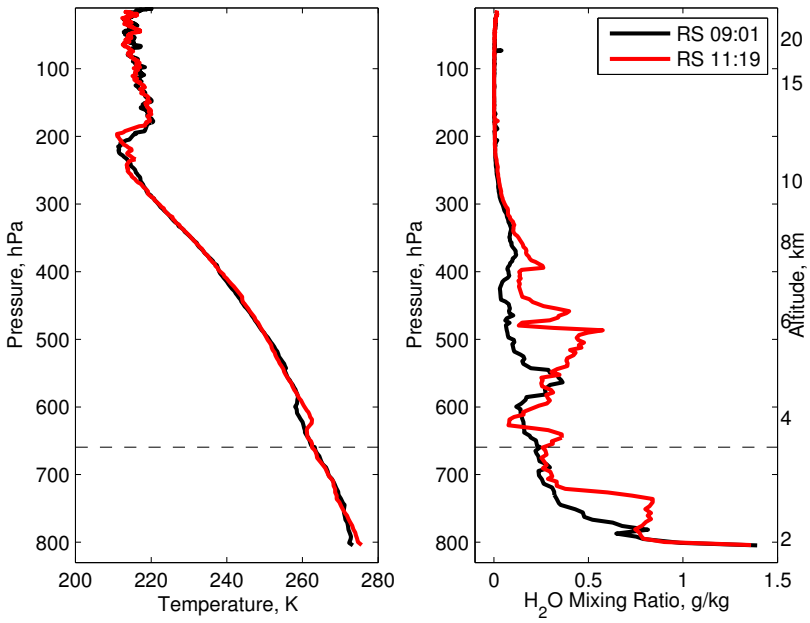

Figure 5.5: Temperature (left panel) and Water Vapor (right panel) profiles recorded by the Radiosondes started from Cervinia station at 9:01 GMT (in black) and 11:19 GMT (in red). The dashed lines indicate the altitude of Testa Grigia station.

The GBMS made almost continuously precipitable water vapor obser-

vations from 6:00 to 11:35 GMT (21 observations) and from 15:00 to 17:00 GMT (8 observations). Radiosonde and GBMS observations are summarized in Fig. 5.6.

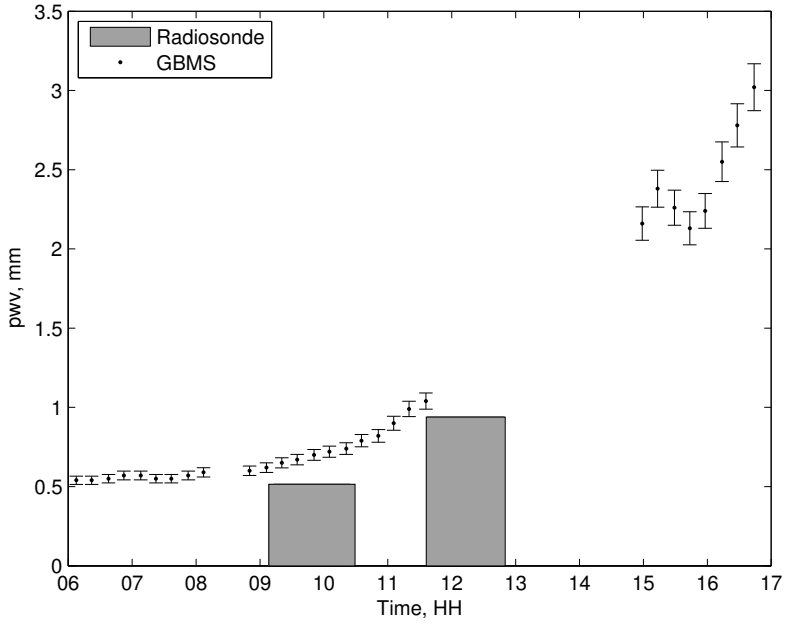

Figure 5.6: Precipitable Water Vapor as function of the time. Black dots indicate the GMBS measurements, Grey boxes indicate the Radiosonde measurements.

To properly co-locate in time and space radiosonde and REFIR-PAD observations a series of operations were performed over temperature and H_2O radiosonde profiles. First, both profiles were scaled to the altitude of REFIR-PAD. Second, the temperature profiles were adjusted to take into account for the local environment around REFIR-PAD. This adjustment has been described at length in Esposito et al. (2007) and (Masiello et al., 2012) and consists in adjusting the temperature profiles until we reach a spectral consistency with the REFIR-PAD spectrum in the most intense portion of the CO_2 band at 15 μm. In fact, the spectral radiance measured in this portion of the CO_2 band is due to the emission of the local environment which is seen from the instrument through its field of view. Note that REFIR-PAD was not directly deployed in the open atmosphere. It was sealed in a plexiglas

envelope, which partly insulated it from the environmental condition of the outdoor air.

Finally, to make up for the dry bias effect (Turner et al., 2003) of VAISALA RS92k humidity sensor, the mixing ratio profile of water vapour was scaled to the time colocated GBMS total column observations.

5.2.3 Lidar setup and data analysis

The University of BASILicata Raman Lidar system (BASIL) was deployed in Cervinia (Lat: 45°55'57" N, Long: 7°37'42" E, elevazione: 1990 m) in the frame of the Earth COoling by WAter vapor Radiation (ECOWAR) experiment (Bhawar et al., 2008; Serio et al., 2008b). During ECOWAR, BASIL operated between 4 and 16 March 2007, collecting approximately 100 hours of measurements. Quick-looks of the data are available on the ECOWAR Website (`http://www2.unibas.it/gmasiello/cobra/index.htm`) and data can be directly requested to the authors of this paper.

The major feature of BASIL is represented by its capability to perform high-resolution and accurate measurements of atmospheric temperature and water vapour, both in daytime and night-time, based on the application of the rotational and vibrational Raman lidar techniques in the UV (Bhawar et al., 2011; Di Girolamo et al., 2006, 2004, 2012a,b, 2009a). Besides temperature and water vapour, at the time of this field deployment BASIL provided measurements of the particle backscattering coefficient at 355 and 532, of the particle extinction coefficient at 355 and of the particle depolarization at 355 (Di Girolamo et al., 2009b; Griaznov et al., 2007; Maestri et al., 2010).

Data from BASIL are used in this paper to estimate the cirrus cloud optical depth. Cirrus cloud optical depth can be estimated from the elastic lidar signals, which show attenuation due to the presence of the cloud. The amount of this attenuation can be converted into optical depth if the atmospheric density profile is known. Specifically, a molecular signal can be calculated from the atmospheric density profile, taking into account molecular extinction and range attenuation (Di Girolamo et al., 1994). The elastic lidar signal is fitted to the molecular signal in a aerosol-free region below and above the cirrus cloud. The normalization factors for these two regions, respectively k_1 and k_2, are used to determine the cloud optical depth, OD_{cloud}, through the expression:

$$\mathrm{OD}_{cloud} = \frac{1}{2} \ln \frac{k_1}{k_2} \tag{5.1}$$

For the purpose of this paper the elastic lidar signals at 532 nm are considered. The atmospheric density and molecular extinction profiles are obtained from the radiosonde data, this latter based on the assumption of Rayleigh scattering for the molecular component of the atmosphere. 27 radiosondes were launched simultaneous to the lidar operation during ECOWAR. The normalization height above the cirrus cloud is selected approximately 3-4 km above the cirrus top height to minimize effects associated with multiple scattering. In fact, for a similar case study, Mona et al. (2007) showed that in the case of BASIL (field of view= 0.55 mrad) a cloud optical depth overestimate of 11 % can result from neglecting the effects of multiple scattering. The random error affecting the lidar-based cloud optical depth measurement increases with the increasing optical depth values. For the cases reported in this paper the error varies from 0.05 (for the lowest OD_{cloud} values) to 0.2 (for the highest values).

5.2.4 descrizione del Refir-pad e degli errori

REFIR-PAD (Radiation Explorer in the Far InfraRed – Prototype for Applications and Developmet) is a Fourier transform spectroradiometer (FTS) designed to perform accurate measurements over the broad spectral range of the thermal atmospheric infrared emission, including the far infrared (FIR) portion, using uncooled detectors Bianchini et al. (2006). It was developed at IFAC-CNR to demontrate the feasibility of the space-borne FTS designed within the REFIR EU project Palchetti et al. (1999)-Palchetti et al. (2005). REFIR is a novel space mission devoted to collect a complete and accurate long-term data sets of the radiation emitted by Earth in the FIR Rizzi et al. (2001).

REFIR-PAD uses a Mach-Zehnder configuration with two input ports and two output channels. One input port is used to observe the atmosphere for looking at the unknown scene to be measured and the second one for looking at internal reference blackbody (BB) sources, which allow the access and the control of the instrument self-emission Bianchini et al. (2009). At the output ports, signals are acquired with two uncooled DLATGS (deuterated L-alanine-doped triglycene sulfate) pyroelectric detectors. This configuration optimizes the performances for room temperature operations and maximizes the reliability of the calibration in particular for long lifetime applications. The instrument has simple mechanical and electrical interfaces, light weight (55 kg) and low power consumption (about 50 W average) for an easy in-

tegration for field observations in ground-based campaigns Bianchini et al. (2007) and on board stratospheric platforms Palchetti et al. (2006)-Palchetti et al. (2007). For the ground-based observations performed at Testa Grigia, the instrument was installed outside the station in a Plexiglas box, to avoid extreme thermal excursions and wind disturbances. More details of this experiment are reported in Bhawar et al. (2008)–Fiorucci et al. (2008)–Bianchini et al. (2011).

The main instrument parameters of REFIR-PAD for this campaign are shown in Table 5.1. The measurement port looks at the scene through two folding mirrors, one of each is inside the instrument and allows also the radiometric calibration by observing the two internal reference BB sources, one hot (HBB) at about 80 °C and one cold (CBB) at about 18 °C. A second folding mirror below the viewing port, is external the instrument and allows to look the atmosphere at the zenith direction.

Table 5.1: Main characteristics of REFIR-PAD.

Beam splitter type	Broadband Ge-coated Mylar
Operating spectral bandwidth	100-1400 cm^{-1}
Operating spectral resolution	0.5 cm^{-1} (double-sided interferogram)
Field of view	133 mrad
Detector system	2 room temperature pyroelectric (DLATGS)
Acquisition time per measurement	64 s
Calibration measurements per sequence	2 for HBB and 2 for CBB
Zenith observations per sequence	4
Sequence duration	10 min
Spectrum average duration	5 min

Measurements of 64 s acquisition time are taken in sequences of 4 calibrations (2 measurements looking at the HBB and 2 looking at the CBB) and 4 atmospheric zenith observations. Each sequence lasts about 10 minutes, including delays among single measurements and produces a 5-minute averaged spectrum of the observed scene. The instrument was operated for a total of 61 hours in 11 days, with daytime and nighttime measurements and

under widely varying meteorological conditions both in terms of water vapor concentrations and cirrus clouds presence. As an example, spectra acquired under clear sky and cirrus clouds conditions are shown in Figure 5.7. Water vapor absorption and measurement conditions limit the useful range to about 250 – 1100 cm^{-1}.

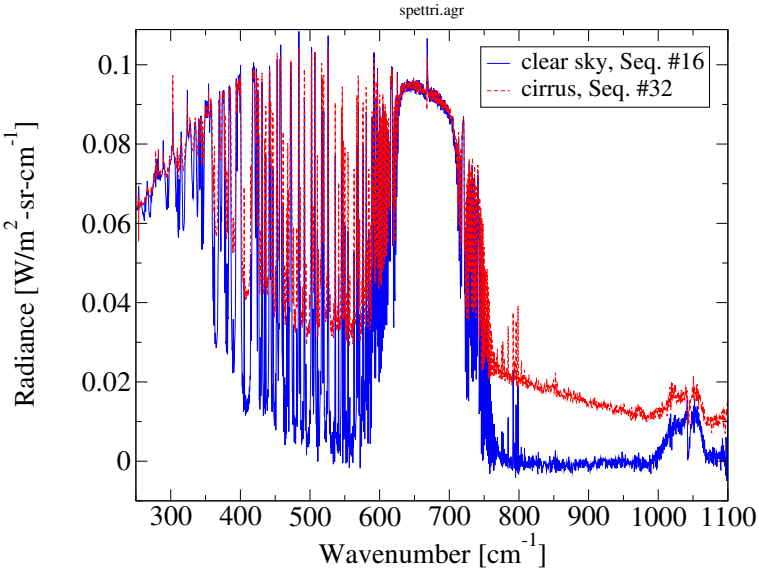

Figure 5.7: REFIR-PAD spectra measured under clear sky and cirrus clouds conditions.

Frequency and radiometric calibration of spectra are performed following the procedure outlined by Bianchini and Palchetti (2008). The radiometric error on each averaged spectra has been calculated by taking into account both the instrument measurement error and the error of the mean, which contains possible scene variations. Instrument error is composed of two parts. The first one, called noise equivalent spectral radiance (NESR), comes from the detector noise (random error component) and produces independent fluctuations for each spectral element. The second one comes from the radiance uncertainty with which the reference BB sources are known (systematic error component), and produces a calibration error (Cal Err). Both instrument error components have been extimated by the error propagation in the calibration procedure, whereas the error of the mean has been calculated by the standard deviation (σ) of the averaged spectra Bianchini and Palchetti

(2008). Figure 5.8 shows the error estimates for the clear sky and cirrus cloud conditions.

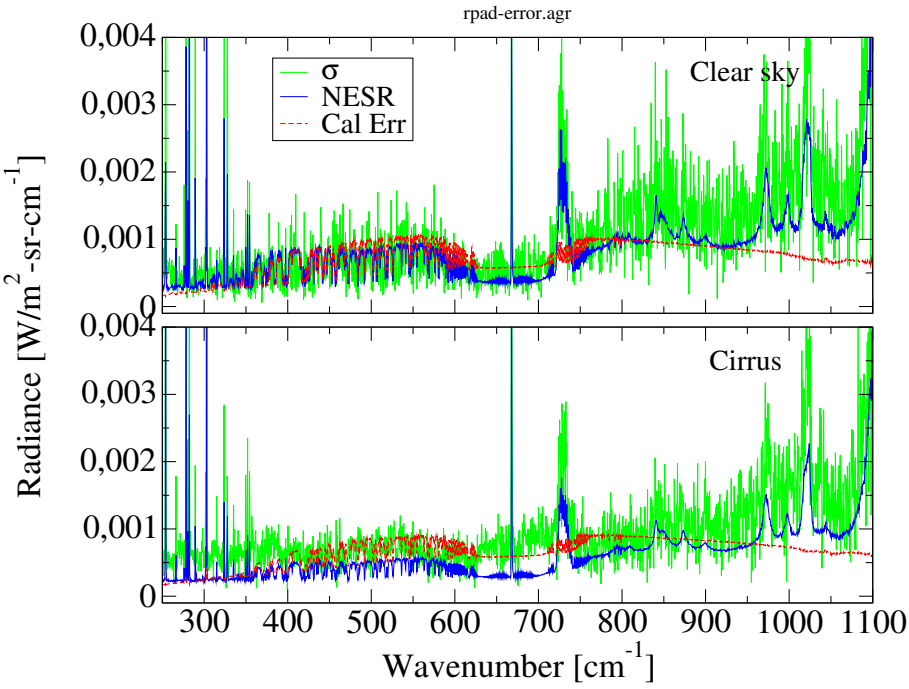

Figure 5.8: REFIR-PAD radiometric error measured under clear sky and cirrus clouds conditions.

5.3 Cloudy fields analysis

5.3.1 Methodology

On day 9 March 2007, in Testa Grigia Italian Alps station on Testa Grigia (3480 m a.s.l., 45.933° N, 7.7° E), REFIR-PAD collected data from about 07:25 UTC to 13:50 UTC with the exception of a gap of about 40 minutes starting at around 11:50 UTC. The measurement conditions showed clear sky until around 09:00 UTC. From that time, the BASIL Raman Lidar, located in Breuil-Cervinia (at 1990 m a.s.l., 45.933° N, 7.6° E) at about 5 km from Testa Grigia, revealed the appearance of a thin cirrus cloud that persisted for all the rest of the measurement session. Until 11:50 UTC (corresponding to the

first part of the measurements of the REFIR-PAD) the cirrus cloud optical depth measured by the lidar was very small, less than 0.3. After 12:30 UTC, in correspondence of the second interval of measurements of REFIR-PAD, the lidar derived optical depths show a rapid increase, with values close to unity.

The present study analyzes a subset of the REFIR-PAD data collected on 9^{th} of March and focuses on the last part of the measurement session that ranges from 12:30 UTC to 13:50 UTC. For this period of time the cloud signal is the highest. Each REFIR-PAD measurement, that is the average of four scans of about 64 s each looking at the scene (other four scans look at the calibration BBs), will be referred as 'FOV'. On a total of 31 FOVs observed by REFIR-PAD during the whole day, the analysis is here restricted to the last eight FOVs.

The methodology used in the analysis of the REFIR-PAD data collected in cloudy conditions can be summarized in five main steps as follows:

1. Determination of the temperature and gas concentration profiles
2. Computation of the gaseous optical depths
3. Retrieval of the cloud optical depths and PSDs from Refir-Pad spectral radiances in the main atmospheric IR window (800–1000 cm^{-1})
4. Simulation of the REFIR-PAD downwelling radiances in cloudy sky over the whole measurements spectral coverage (250–1100 cm^{-1}) based on retrieved cloud parameters
5. Evaluation of the residuals between simulations and data in the FIR part of the spectrum and sensitivity studies

The temperature and water vapor profiles are derived using a fit methodology as described in section 5.2.2 which exploits radiosondes and GBMS data. Ozone profile is derived from the GBMS measures taken on 7^{th} of March from the Testa Grigia station. The CO_2 concentration is set equal to 387 ppmv at all levels according to the climatological value. Typical ML model concentration profiles of methane, carbon monoxide and of other minor species active in the IR part of the spectrum are also used (Anderson et al., 1986).

From temperature and gas profiles the gaseous optical depths are computed with the model LbLRTM (Clough et al., 2005). A modified version

of the LbLRTM release 11.3 is used, in which new coefficients for the water vapor continuum absorption are inserted as described by Serio et al. (2008b).

5.3.2 Retrieval of cloud properties

The cloud properties retrieval code RT-RET (Maestri and Holz, 2009) is utilized for the derivation of the cloud optical depths and effective dimensions from REFIR-PAD radiances in the 820-960 cm^{-1} spectral interval only. A mixture of habits typical of ML cirrus clouds (Bozzo et al., 2008), whose optical properties have been already tested in the wavenumbers range 650-2700 cm^{-1} (Maestri et al., 2010), is assumed as a-priori information. RT-RET is applied to each one of the FOVs considered in the analysis (corresponding to FOVs from 24 to 31 of the day of measurements). A plot of the retrieved optical depths is given in Figure 5.9. The Figure shows that the cirrus cloud optical depth is increasing with time consistently with the lidar results, also reported in the plot for comparison. In the Figure, REFIR-PAD derived SW optical depths are plotted, so that a direct evaluation of the optical depth values against those derived from the lidar is made possible. The conversion between IR and SW optical depths is provided thanks to the microphysical information (PSD) that is derived by RT-RET too.

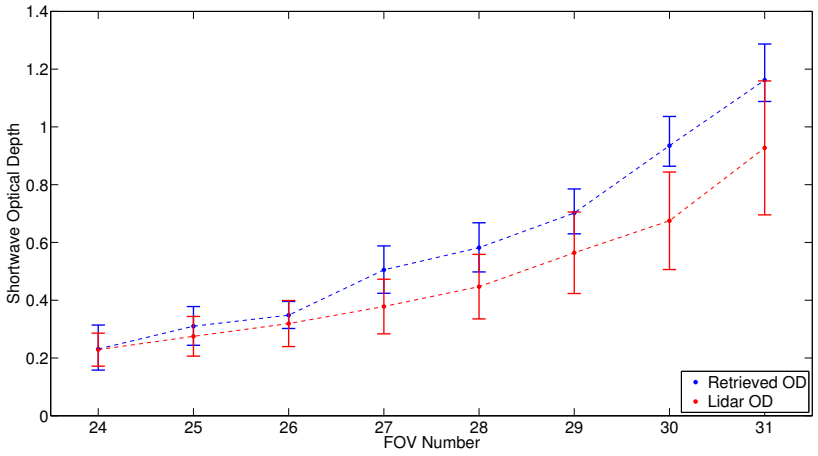

Figure 5.9: REFIR-PAD retrieved optical depths (blue line) and associated retrieval uncertainties. In red the BASIL derived optical depths are also reported for comparison.

A modified version of RT-RET, with respect to the one used in (Maestri et al., 2010) is properly arranged for this study in order to minimize the uncertainties due to the assumptions on cloud physical properties. The new version accounts for the possibility to assume a uniform ice distribution along the cloud vertical extent (as in the old version) or, alternatively, an ice vertical distribution derived from a statistical analysis. In this second case the IWC distribution is derived from the vertical backscatter profile and parameterized as a function of the cloud geometrical thickness as shown by (Veglio and Maestri, 2011). This option is adopted in the present work to allow a more realistic description of the cloud properties. In Figure 5.10 the climatological profile of the backscatter coefficient of cirrus clouds is compared to the averaged backscatter profile measured by the BASIL lidar during the 12:30-13:40 UTC interval whose mean geometrical depth is 4 km. Backscatter values are re-scaled to the same vertical length and normalized to their integral values. Both profiles show a maximum in the backscatter value close to cloud bottom. A second maximum is observed in both cases in the upper part of the cloud. The consistency between the two curves suggests that typical cirrus cloud conditions are present during the experiment. The climatological profile is used within RT-RET for this case study due to the large statistic from which it is derived and from the fact that the lidar is anyway 7 km distant from the REFIR-PAD measurement site and thus is not exactly representative of the REFIR-PAD observed scene. Numerical tests have shown improvements in the derivation of cloud optical depth and effective dimensions up to 10 %.

The cloud thickness is derived from the lidar data and thus undergoes a spatial offset with respect to the REFIR-PAD measures. An estimation of the uncertainties related with an incomplete knowledge of the heights of the cloud boundaries is accounted for in the retrieval process and errors are evaluated. As demonstrated by Maestri and Holz (2009), the uncertainties on cloud thickness and altitude are the largest source of error in IR cloud properties retrieval algorithms applied to both up-looking or down-looking sensors. Total uncertainties associated with the RT-RET optical depth retrieval are shown in Figure 5.9 as error bars. The uncertainties shown in the Figure account for code and data errors and for errors associated with the a-priori assumptions made in the retrieval (such as the already mentioned cloud boundaries altitudes, surface temperature, etc.). Note that the retrieved optical depth is derived from retrievals performed independently on a number of about 15 single REFIR-PAD channels, each one affected by a

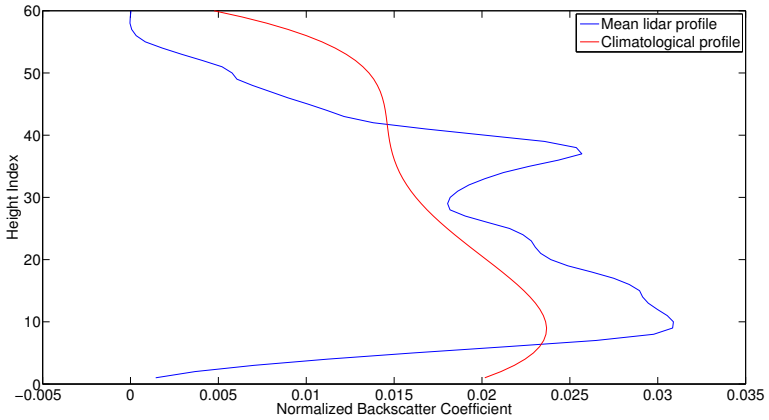

Figure 5.10: Climatological and BASIL backscatter profiles. The climatological value is derived from (Maestri and Holz, 2009) by assuming a cloud with geometrical depth equal to 4 km. BASIL backscatter profile is obtained by averaging the backscatter profiles measured from the Breuil-Cervinia station during the 12:30–13:40 UTC time interval. The profiles are rescaled to the same vertical length and normalized.

different level of noise and calibration error. When the cloud is optically very thin (i.e. for FOV 24), and the REFIR-PAD signal in the main windows is very low, the code-data errors are predominant while for the optically thickest layers (i.e. for the last three FOVs) the emission processes become more important and the assumptions made on the heights of the cloud top and bottom position are critical. In this last case the uncertainties associated with the cloud height and geometry are the largest source of error.

5.3.3 Testing of ice cloud optical properties in the FIR

RT-RET derived cloud parameters (optical depth and effective dimension) are exploited to run forward simulations of the observed cloudy scenes over the whole REFIR-PAD spectrum. Since cloud parameters are retrieved using a limited numbers of channels within the 820–960 cm^{-1} spectral interval, while the forward simulations are run over the 100–1100 cm^{-1} bandwidth, both the accuracy of the retrieval methodology and the consistency of the cloud optical properties can be evaluated. Forward simulations are performed by using the RTX radiative transfer code (Rizzi et al., 2007) that is based

on the same algorithm used in RT-RET so that the computational errors are minimized and the inverse and direct computations are coherent.

In Figure 5.11 the spectral difference between simulations and the REFIR-PAD data are shown for all the eight FOVs considered. For each FOV, the spectral residuals (blue curves) within the 820–1000 cm^{-1} interval are smaller than the spectral uncertainties (red curves) that, as said, account for both the instrument measurement errors and the errors of the mean containing possible scene variations. This is an expected result since 15 channels in the 820–960 cm^{-1} interval are used to perform the retrievals from which the optical and microphysical properties of the cloud are assumed in the forward simulations. Residuals in the FIR, for most of the cases, show the largest discrepancies between simulations and data. Only for FOV number 24, corresponding to the REFIR-PAD measure at time 12:30 UTC when the cloud optical depth is the smallest, the FIR simulation minus data are almost completely within the total uncertainty with the exceptions of some spikes present in the measurement at localized wavenumbers.

For any assumed temperature profile the residuals in the FIR are due to the assumption on both cloud features and water vapor's profile and total content. In particular, the higher is the water content in the atmosphere (and/or the cloud optical depth) and the higher is the downwelling radiance detected at the ground. Water vapor signal is stronger in the center of the roto-vibrational lines but it also affects all the REFIR-PAD channels in the FIR. The cloud signal is mostly detected in the so called FIR "dirty windows" corresponding to REFIR-PAD channels within 250 and 600 cm^{-1} where the radiance signal is not saturated by water vapor. Within dirty windows the cloud and water vapor signals both contribute to the measured downwelling radiance; in turn they depend on atmospheric and cloud temperature profiles.

Note that FOV 24 is the closest, in terms of temporal offset, to the latest launch of the radiosonde and supposedly the assumed atmospheric temperature and humidity profiles are very similar to the conditions of the atmospheric column encountered during the observations performed by REFIR-PAD. Since the measured cloud optical depths are very small for the first FOVs, it is supposed that the cloud properties evaluation in the FIR is better performed in the last FOVs where the cloud signal is the largest. For these cases some discrepancies are observed between data and simulations especially in the 350-500 cm^{-1} bandwidth.

In the upper panel of Figure 5.12 the mean discrepancies between simulations and REFIR-PAD measures are plotted for selected micro-windows

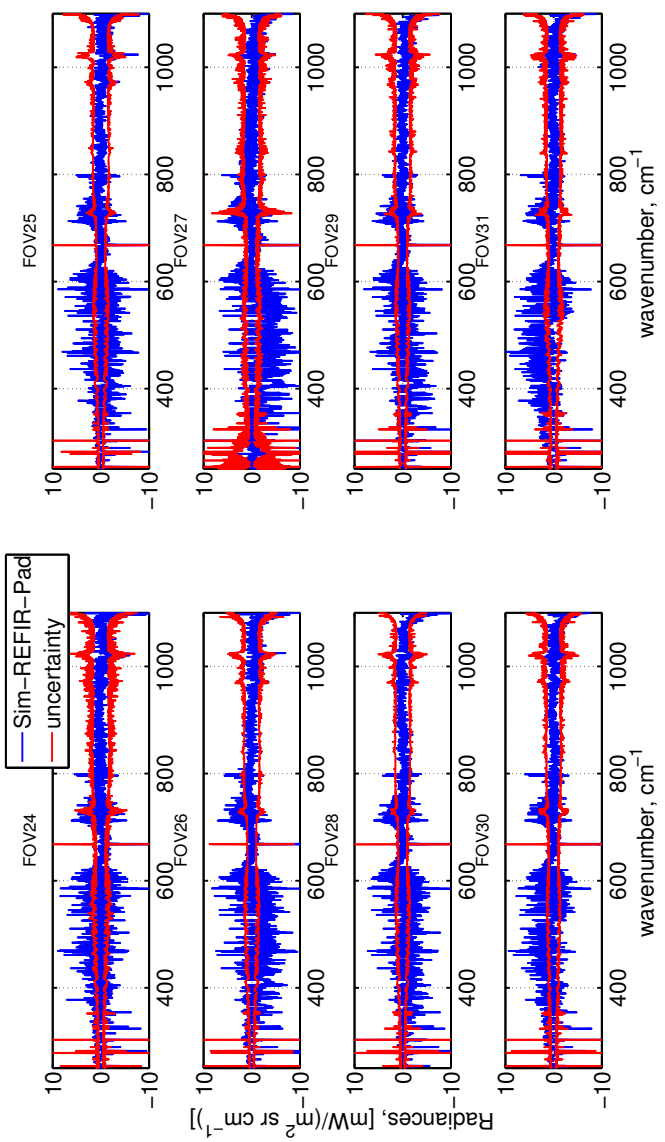

Figure 5.11: Spectral difference between forward simulations of REFIR-PAD downwelling radiances and data as a function of the wavenumber. Results from all the eight FOVs are shown and ordered for rows.

in the FIR. The mean discrepancies are plotted as functions of the observed FOV (i.e of the cloud optical depth that increases during the time of measurements). For each FIR micro-window the radiance is an average of nine channels around a central wavenumber value that is reported in the Figure's legend. The error bars are the mean uncertainties associated to the REFIR-PAD measures within the micro-windows. The results are plotted with a slight offset along the x-axis in order to make the plot readable and to allow the evaluation of the uncertainties. The discrepancies found in the main atmospheric window channels (820 to 960 cm^{-1}) are not shown since they are very low and much smaller than the total mean uncertainty of the bandwidth.

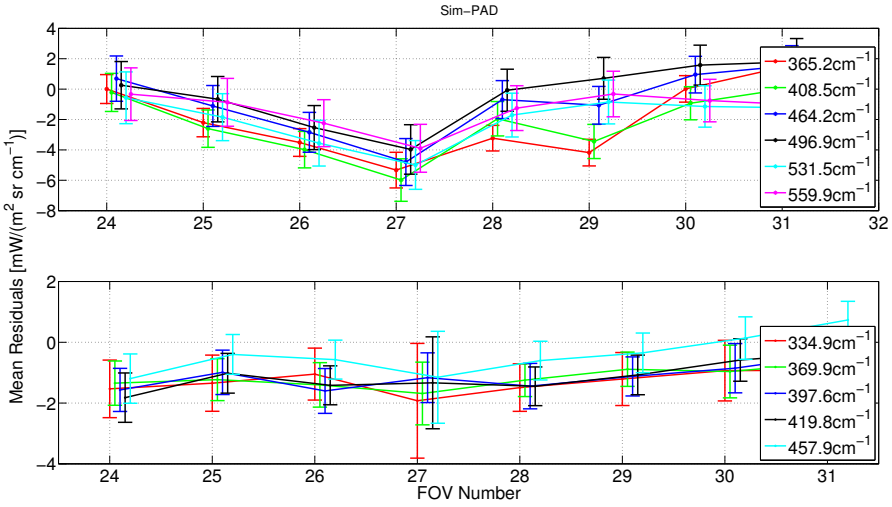

Figure 5.12: Upper panel: Mean residuals between simulations and data for selected micro-windows in the FIR (see Legend) as function of the FOV (i.e. measured optical depth). Error bars represent the mean total uncertainties associated to the residuals within each FIR micro-window.

The shape of the curves is very similar for each micro-window channel. A good agreement between simulations and data is found for FOV 24 and a general worsening of the simulations is observed for FOV 24 to 27 (all the curves show decreasing negative discrepancies). The last four FOVs (from 28 to 31) show the largest spreads within the curves of the differences between simulation and data. For these FOVs the discrepancies range between 2 and -2 $\mathrm{mW/(m^2 cm^{-1} sr)}$, except that for FOVs 28 and 29 (optical depth is

around 0.7) for which channels at 365 and 408 cm^{-1} reach values between -2 and -4 $mW/(m^2 cm^{-1} sr)$. These two channels are those that show the overall worst performance. Note also that channels at 365 and 408 cm^{-1} are those where the effect of water vapor is the largest since the measured values of the downwelling radiance in clear sky is the highest for all the FIR micro windows considered (not shown).

Similarly to what shown in the upper panel of Figure 5.12, the lower panel of the same Figure shows the discrepancies between simulations and data for selected water vapor highly absorptive channels. As in the case of FIR micro windows, the very absorptive bands are an average of radiance values around a central wave-number (reported in the legend). The differences between simulations and data are shown in order to evaluate the degree of accuracy of the assumptions in the temperature and water vapor profiles used for the radiative transfer simulations. In fact, assumed temperature and water vapor profiles strongly influence the computed downwelling radiance at wavenumbers where water vapor absorption lines are present. For very strong absorption lines, as those selected here and shown in the lower panel of the Figure, the sensitivity to water vapor concentration is quite low for typical atmospheric values since opacity is reached for even small water vapor mixing ratios. Thus, for these channels, radiance is mostly influenced by temperature profile at levels close to the measurement apparatus.
Results show a general underestimation of the downwelling radiance of the order of -1 $mW/(m^2 cm^{-1} sr)$ that gives an idea of the uncertainty associated to radiance simulations due to the assumption on the temperature and (to a lesser extent) water vapor profiles close to the ground station.

5.3.4 Sensitivity studies

Since residuals between forward simulations of the downwelling radiance and REFIR-PAD data in the FIR spectral range are, in most cases, larger than the total uncertainties associated to measurements, an in depth investigation concerning the reasons for such discrepancies is required. The simulated radiance is affected by: (i) a priori assumptions on cloud parameters that are based on climatological information but might result inadequate for the present situation and (ii) an incomplete or inaccurate knowledge of the atmospheric state.

As it concerns the a priori information, the main assumption regards the ice cloud particle habits. In order to evaluate the radiance sensitivity to the

assumed cloud particle shape, PSDs containing a different type of habits with respect to the previously used (a mixture of ice habits typical of ML cirrus clouds) are now assumed. Since the ML mixture is mostly a combination of bullet rosettes, aggregates and droxtals, the whole process summarized in Section 5.3.1 is now performed again assuming that the particles composing the cloud layers are pristine hexagonal columns. Note that hexagonal columns are only the 5 % component (in mass) of the ML mixture.
In Figure 5.13 the residuals between forward simulation based on retrieved parameters assuming PSDs made of ice columns or of a mixture of habits are compared. Three micro-windows in the FIR are shown. The sensitivity to the assumed habits depends on the spectral channel considered and is larger for the most transparent windows while it is always less than $0.9\,\mathrm{mW/(m^2cm^{-1}sr)}$ for the $365\,\mathrm{cm^{-1}}$ channel that is the less transparent window among those selected. At $559\,\mathrm{cm^{-1}}$ the difference between the simulations performed with the two assumptions on crystal shapes is larger than $1\,\mathrm{mW/(m^2cm^{-1}sr)}$ even when the cloud is optically very thin (about 0.4 optical depth at FOV 27). The differences increase with increasing optical depth for the cases encountered in the present study. The assumption of pristine hexagonal columns results in larger values of the simulated radiance that, in most of the cases, corresponds to a decrease in the simulation-data residuals values. The result is anyway not conclusive since for some cases (FOVs) the simulation worsens independently of the selected micro-window.

As discussed above, the atmospheric state parameters that mostly influence the computed radiance fields are the temperature and water vapor profiles. The uncertainties associated with the temperature profile (close to ground station) have been estimated in the previous section, hence we focus here on the radiance sensitivity to water vapor profile in presence of ice layers. For the case FOV 27 a new simulation is performed that accounts for an increase in the relative humidity value of 10 % at all atmospheric levels with respect to the standard simulation where the assumed profile is derived from a combination of radiosonde and radiometer data. In Figure 5.14 the differences in the radiance values between the 2 simulations are shown, in blue, for six FIR micro-windows (the same ones used in Figure 5.11) and for the main atmospheric window 820-960 $\mathrm{cm^{-1}}$. The results show that the differences are larger (in absolute value) than $1.5\,\mathrm{mW/(m^2cm^{-1}sr)}$ for the less transparent windows and diminish to 0.5 $\mathrm{mW/(m^2cm^{-1}sr)}$ at 559 $\mathrm{cm^{-1}}$. A comparison with Figure 5.13 highlights that the sensitivity to water vapor relative humidity is the highest where the sensitivity to cloud particle

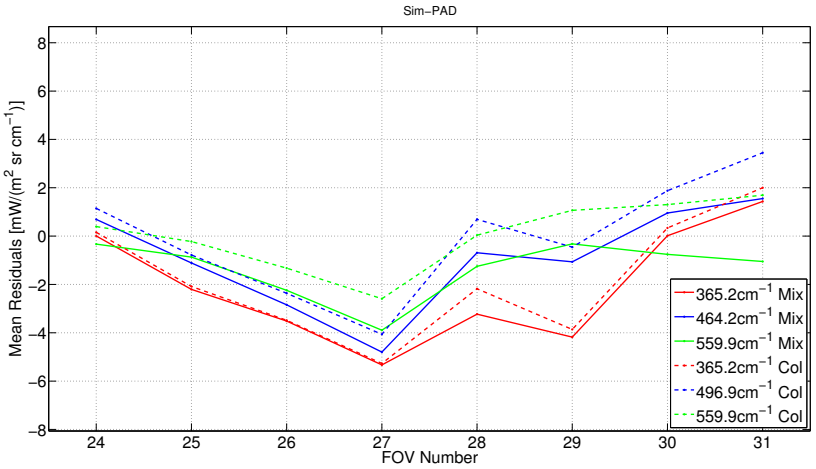

Figure 5.13: Mean residuals between simulations and data for selected micro-windows in the FIR (see Legend) as function of the FOV (so for increasing measured optical depths). Results are for a mixture of particles habits and for pristine solid columns.

habits is the lowest and vice-versa. Nevertheless, for most of the cases, the differences found between the two simulations are not sufficient to explain the residuals between data and simulations shown in Figures 5.12 and 5.13. On the same Figure 5.14, the radiance differences that a satellite sensor, with the same REFIR-PAD spectral resolution, would detect observing the same scene of FOV 27 are reported in red. The very low values of the differences highlight the low sensitivity to changes in water vapor profile, mostly due to the fact that the cloud is high in the atmosphere and its signal would reach the satellite sensor without passing layers with relevant absorption/emission from water vapor. It is then demonstrated that a satellite view configuration would be of great advantage for the study of the optical properties of ice clouds in the FIR.

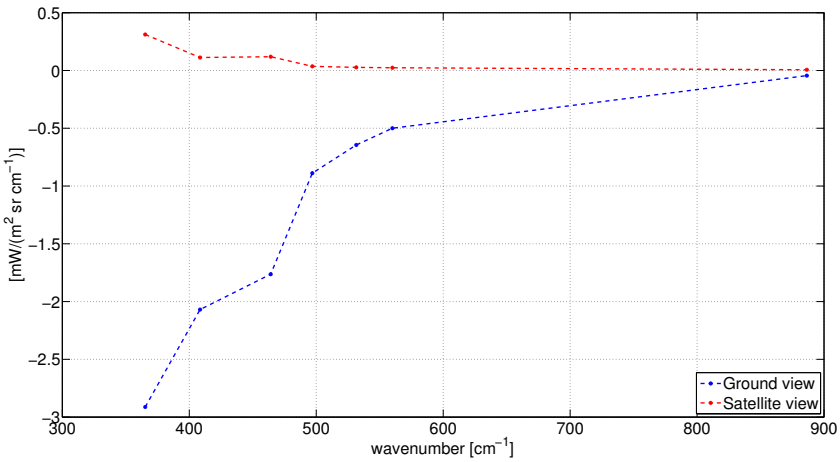

Figure 5.14: Sensitivity to a change of 10 % in the relative humidity profile in selected micro-windows within the FIR and in the main atmospheric window. Results for upwelling (in red) and downwelling (blue) radiances are reported. The atmospheric and cloudy conditions are those of FOV 27.

Chapter 6

Testing of a new hyperspectral infrared retrieval

It has already been stressed in the introduction how important can be having simultaneous measurements of the same scene from different sensors that cover different portions of the electromagnetic spectrum. Furthermore, in the previous Chapter it has been shown how it is possible to combine the results derived from CALIOP with high resolution infrared radiances to obtain more precise retrievals of cloud properties and forward simulations. Also having ancillary information on the state of the atmosphere, namely atmospheric profiles of gaseous concentrations, water vapor and temperature resulted to be a crucial point in order to reproduce accurately the measured radiances.

In this Chapter a step forward is attempted, extending the idea of simultaneous measurements to a global perspective, using some of the instruments that fly in formation on the satellites of the A-Train constellation. Thus, a collocation procedure is described and, in the last sections, an application for the testing of fast physical retrieval is presented.

6.1 Creation of a collocated dataset

The collocation process has to take into account and solve some complications due to the fact that this procedure involves diverse sensors, which in general have different geometries of observation and fly on different spacecrafts, resulting in various spatial resolutions and sampling rates. In the following sections a description of how these complications are unraveled in

order to obtain a data set of AIRS-CALIOP-MODIS collocated products will be provided.

Prior to delve into the details of the collocation process it is useful to provide an overview of FOV sizes and sampling times of the different sensors used, together with other information, extendings some of the details presented in Section 2.1.

AIRS (Atmospheric Infrared Sounder: is a high spectral sounder which operates in the infrared region of the electromagnetic spectrum. Every two seconds it scans the ±49.5 degree angle, which corresponds to a nominal swath width of approximately 1650 km. The full swath contains 90 infrared footprints with a resolution varying from 13.5 km at nadir angle to 41 km x 21.4 km at the extremes of the swath. The AIRS data are provided every six minutes in granules containing 135x90 along track by cross track FOVs.

MODIS (Moderate Resolution Imaging Spectroradiometer): is a cross-track scanning spectroradiometer with 36 bands at key wavelengths in the visible and infrared regions. With its ±55 degrees scanning angle it achieves a 2330 km swath. Its spatial resolution is 1 km at nadir, with the exception of bands 1 and 2 that are provided at 250 m and bands 3 through 7 at 500 m. MODIS granules are produced every five minutes containing 2030x1354 along track by cross track FOVs.

CALIOP (Cloud-Aerosol Lidar with Orthogonal Polarization): is a two-wavelength (532 nm and 1064 nm) polarization-sensitive lidar with a footprint of about 100 m. Its products are provided at three different horizontal resolutions that are 333 m, 1 km and 5 km. The CALIOP data are made available every half orbit, corresponding to approximately 45 minutes and contain about 65 000 FOVs at full resolution.

6.1.1 The collocation procedure

In order to match the different satellite data, a procedure that takes into account the different spatial resolutions and sampling times is developed. A schematic representation of the whole process is shown in Figure 6.1. The first step is done by coupling the AIRS data with either MODIS or CALIOP, thus creating two distinct data sets, named AIRS-CAL (CALIOP and AIRS

data) and AIRS-MOD (MODIS and AIRS data). The coupling of the AIRS-CALIOP and AIRS-MODIS pairs is performed by using the methodology developed by Nagle and Holz (2008). This method allows to combine measurements from two instruments, defined respectively as "master", that is the instrument onto whose footprint the measurements of a second sensor are to be projected, and the "slave", that is the instrument whose measures are projected onto the master footprint. In this work AIRS is considered the "master".

The input data of the AIRS-MOD and AIRS-CAL algorithms are selected so that the couples have a temporal overlap. The selection of the input couples is performed by a procedure developed for this purpose, and applied at the beginning of these two scripts. The pairing algorithm reads the time stamp of an AIRS file and then looks for MODIS or CALIOP files that overlap with that AIRS granule. Since the sampling times are different, it is possible to have, for instance, two AIRS files associated to one MODIS file, or vice versa. This situation holds also for CALIOP that, on average, matches with eight AIRS files.

Once a pair is selected, the appropriate script (AIRS-MOD or AIRS-CAL) reads the input couple and produces (using the Nagle and Holz (2008) methodology) an output file containing a list of index pairs. These index pairs indicate the position of all the matching data whitin those input files, that will be used in the following steps in order to extract the data. This procedure is repeated until all the three data sets are read and matched. The final result of this step is the production of two separate data sets, one for AIRS-MODIS and the other for AIRS-CALIOP. The data used in this step are AIRS L1, MODIS MOD03 and CALIOP L1 products, that all contain the coordinates at the full resolution of the sensor.

In the next step these two data sets are merged and then used to extract the data from the satellite products and eventually create the final collocated database. The AIRS-CAL-MOD script is developed for this task. The merging procedure operates similarly to the pair selection method described before. The files of the two data sets that present a temporal overlap are coupled and merged into a single file that contains index triplets, that are the reference indexes for the three instruments, like the index pairs contain the reference for two instruments. In this step, a further complication is introduced by the CALIOP data. In fact, the L1 products used for the creation of the references have a 333 m resolution, but the L2 products are provided also at 1 km and 5 km horizontal resolutions. This issue is solved simply

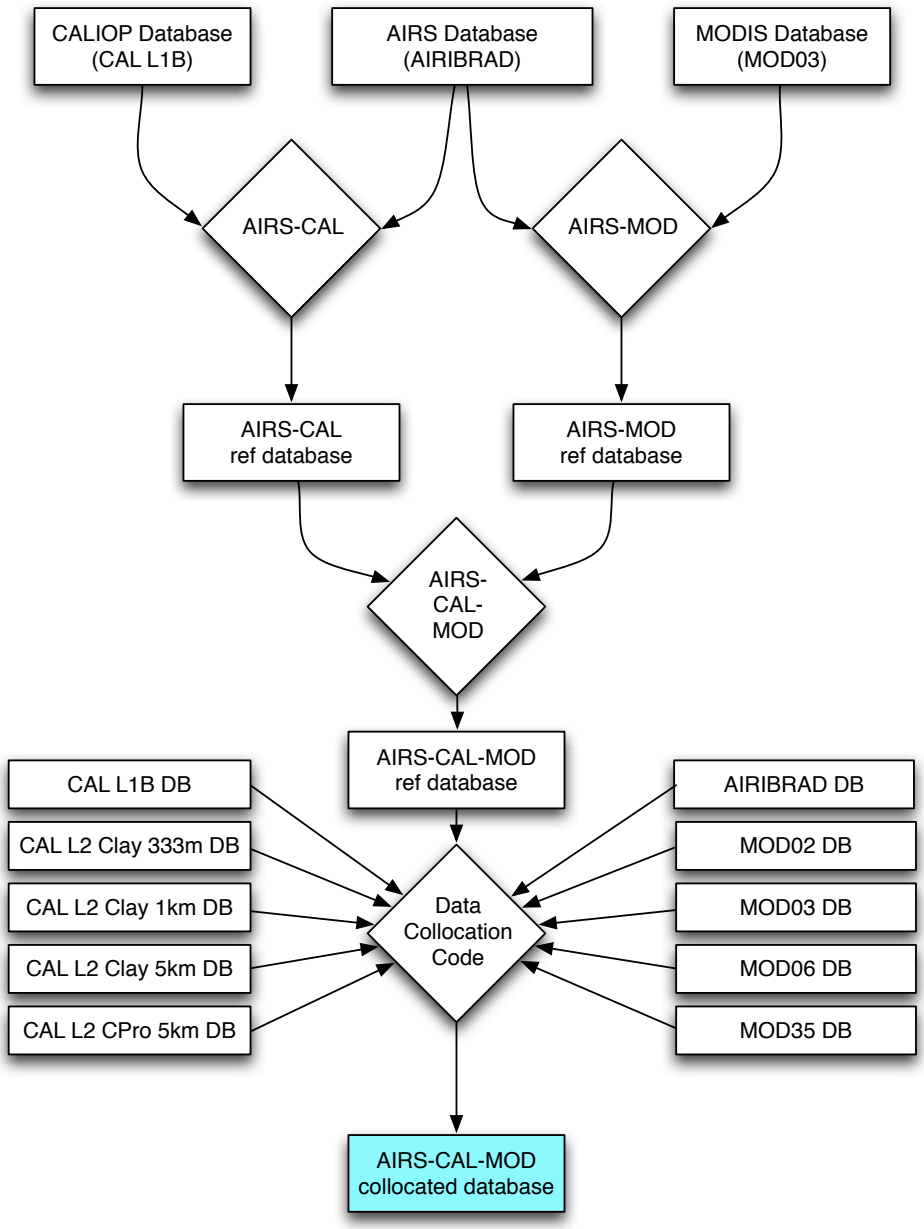

Figure 6.1: Scheme of the collocation procedure. The rectangular boxes represent the data set, the diamond boxes are for the algorithm names.

introducing a conversion factor when the AIRS-CALIOP database is read, depending on which resolution is considered.

To produce the collocated database, the index triplets data set (AIRS-CAL-MOD) is then used in the last step to extract the data from the satellite products. The data collocation code, in order to match data from different instruments, averages every product onto the AIRS footprint, in order to provide a single value for each quantity extracted from the original data.

In Figure 6.2 an example of the structure of a sample collocated FOV is shown. Within an AIRS footprint (blue circle) the MODIS FOVs (red circles) and the CALIOP swath (black line) are collocated. The black diamonds represent the CALIOP data at 1 km horizontal resolution. It is to note that this figure, produced with real data, is a simplified representation and does not take in consideration the exact shape of the FOVs, that should be slightly elongated in non-nadir footprints, as it is this case.

Along with the original data products, averaged at the AIRS footprint size, some additional products are introduced. A brief description of what is stored in the collocated database, with a particular regard to the new products is reported in the following section.

6.1.2 Data utilized

In a final collocated file more than 130 variables are stored. Here a brief description of the data used in the collocation process, and what is extracted to produce the collocated database is provided.

The infrared radiances, the land fraction and some satellite information (such as coordinates, time and scanning angle of the instrument) are extracted from AIRS L1 files.

CALIOP variables are mostly derived from the CLay at the three resolutions. A large part of the data contained in the L2 CLay is imported, averaged at the size of the AIRS footprint, into the collocated products. Together with the mean values, also the corresponding standard deviations are computed, in order to preserve some of the information at the original resolution. Among the many variables extracted from the CLay those used in this work are cloud top and base altitude, optical depth, lidar ratio, midpoint temperature, number of cloud layers. Moreover, from these quantities some other useful variables are derived. First of all the CALIOP cloud fraction at the three resolutions is computed. This quantity is simply the fraction of cloudy CALIOP shots, with respect to the total, within an AIRS footprint.

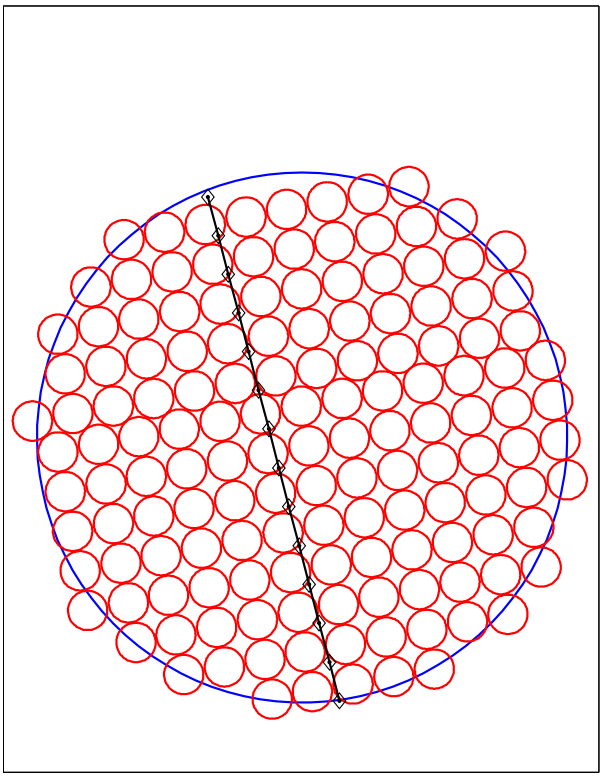

Figure 6.2: Example of a collocated scene. The AIRS footprint (blue circle) with the MODIS FOVs (red circles) inside and the CALIOP swath (black line). The black diamonds are the 1 km resolution CALIOP data.

Other quantities, such as the distance between two adjacent cloud layers or the cloud thickness, are added for convenience, even if they could be easily derived when the data are utilized. From the L2 CPro files the vertical profiles of backscatter and extinction coefficients and the extinction QC are extracted. From the extinction profile some bulk parameters are derived, such as the position of the maximum of extinction and its relative position within the cloud layer (i.e. a value between 0 and 1 is provided where the two extremes represent the cloud bottom and top respectively). The extinction profile is also used to compute the weighting function of the atmospheric column.

The MODIS data are extracted from four different products, that are MOD02, 03, 06 and 35. The MOD02 provides the visible and infrared radi-

ances in the 36 channels of the instrument. For every channel the average of the radiance on the AIRS footprint is computed, together with its standard deviation, and recorded in the collocated products. The standard deviations computed at this stage are then used to determine the homogeneity of the scene, as explained in Section 6.3.

The MOD03 products, that are used in the first step of the collocation process, are the geolocation products. They contain spacecraft position and altitude, sensor orientation and sun position. Only latitude and longitude are extracted from these data.

The MOD06 cloud products make use of visible and infrared channels to retrieve physical and radiative properties of clouds. The quantities used in this study, among all recorded in the collocated products, are the cloud particle phase and effective radius, optical thickness and cloud top height. In addition to the original data also the water phase fraction and effective dimensions are computed. These quantities represent the fraction of liquid or frozen water with respect to the total and their corresponding effective radius.

The MOD35 cloud mask products contain information on the observed scene such as the cloud presence and type with the corresponding level of confidence, and the surface type. As explained in the MODIS ATBD for the MOD35 products (Ackerman et al., 2006), this information is derived using a series of visible and infrared thresholds and consistency tests to specify confidence that an unobstructed view of the Earth's surface is observed. The MODIS cloud fraction is derived from these variables and stored in the collocated products. The MODIS cloud fraction, analogously to what described for the CALIOP case, is the ratio between the total cloudy FOVs and the total FOVs within an AIRS footprint. All the data used in this work belong to the new Collection 6 (Baum et al., 2012) that should be released to the public soon.

In Table 6.1 a list of all the data used is reported with a brief description.

6.2 The dual-regression retrieval algorithm

The dual regression retrieval algorithm is a fast physically based method developed to produce retrievals of cloud and surface properties from satellite high spectral resolution radiances in the infrared region in both cloudy and clear sky conditions. Here a brief description of the basics of this algorithm is

Table 6.1: List of data used.

Name	Description
AIRIBRAD:	AIRS Level 1B calibrated radiances
MOD02	MODIS Level 1B calibrated radiances
MOD03	MODIS geolocated products
MOD06	MODIS cloud products
MOD35	MODIS cloud mask
CAL L1B	CALIOP Level 1B calibrated single shot profiles
CAL L2 CLay 333 m	CALIOP layer cloud products at 333 m resolution
CAL L2 CLay 1 km	CALIOP layer cloud products at 1 km resolution
CAL L2 CLay 5 km	CALIOP layer cloud products at 5 km resolution
CAL L2 CPro	CALIOP profile cloud products

provided, in order to introduce some concepts used in the following sections that discuss about the testing of some outputs of the code, namely the cloud top height.

The dual-regression retrieval algorithm, developed by Smith et al. (2012), is a physical-statistical method developed for real time processing of hyperspectral radiances from satellite data, able to retrieve atmospheric profiles (temperature, humidity, ...) as well as surface and cloud properties (cloud top height, optical thickness, ...). This algorithm is able to process data from the AIRS spectrometer and the IASI and the most recent CrIS interferometers.

The "physical-statistical" definition represents the double nature of the code. On one hand the statistical aspect is due to the dependence of the solution on the statistical properties of radiances, atmospheric profiles and both cloud and surface properties that are contained in a statistical training dataset. On the other hand, the physical aspect indicates the fact that the radiances of the statistical dataset, corresponding to specific atmospheric profiles and cloud and surface parameters (Zhou et al., 2005), are computed offline using a physical radiative transfer code for nine cases (i.e. one clear sky and eight cloudy conditions).

The dual-regression (DR) algorithm makes use of the principal component analysis for two types of eigenvectors (empirical orthogonal functions), called "clear-trained" and "cloud-trained". Both eigenvectors contain retrieved quantities such as surface skin temperature, surface emissivity EOF coefficients (EOFCs), carbon dioxide (CO_2) concentration, cloud-top alti-

tude, effective cloud optical depth, and atmospheric temperature, moisture, and ozone profiles above the cloud and below thin or broken cloud. As the name suggest the clear-trained regression makes use of the surface and atmospheric parameters to radiances computed for clear sky condition, while the cloud-trained regression does the same but for cloudy sky conditions.

The cloud top height, which is the quantity analyzed in the following of the Chapter, is derived by comparing the temperature profiles retrieved by the clear-trained and by the cloud-trained dataset. In this way the so called "thermal cloud top" is defined. This quantity represents the altitude below which the clear-trained temperature retrieval remains colder than the cloud-trained temperature profile or the model-analysis temperature profile from the National Centers for Environmental Prediction (NCEP) Global Data Assimilation System (GDAS). The choice between the cloud-trained and the model profiles is done depending on which profile is warmer than the clear-trained temperature profile. For high clouds (i.e. above 300 hPa) a further condition on the relative humididty is used. The cloud top height for clouds above 300 hPa is then chosen to be the highest altitude between the thermal cloud top described before and the highest altitude (above 300 hPa) where the relative humidity profile of the clear-trained retrieval exceeds the 70 % threshold.

For a complete and detailed description of the algorithm and its mathematical basis see Smith et al. (2012).

6.3 the comparison among DR, MODIS and CALIPSO

Two separate tests are performed on the dual regression retrieval: the first one investigates the ability of the DR algorithm to detect clouds with respect to MODIS; the second one compares the cloud top height retrieved by the DR algorithm with both the CTH measured by CALIOP and with the CTH provided by the MODIS cloud products. Both these tests are performed on a data set of 12 days of the month of january 2010 containing about 600 000 FOVs.

Prior to starting the investigation it is necessary to refine our database, selecting only the FOVs that contain a high cloud. For this reason a set of conditions (see Table 6.2) is applied to the data set. A preliminary selection

is done imposing that: (1) CALIOP cloud fraction must be equal to one (i.e. CALIOP detects a cloud in each FOV within the corresponding AIRS footprint); (2) the detected optical depth is above the noise threshold, that is, higher than 10^{-3} (see Section 3.1 and again (Martins et al., 2011)); (3) a cloud base above 5 km limits the inclusion of thick low level water clouds and (4) the condition on the extinction QC (Quality Check) grants us that the lidar penetrates the whole body of the cloud without being completely attenuated.

Table 6.2: Conditions for the DR test.

	Condition	Value
1.	CALIOP Cloud Fraction	1
2.	Optical Depth	$> 10^{-3}$
3.	Cloud Base Height	$> 5\,\mathrm{km}$
4.	Extinction QC	≤ 4
5.	MODIS Cloud Fraction	1
6.	Variance of $L_{11\mu\mathrm{m}}$	$< 10\%$

Since the CALIOP swath only covers a small portion of the AIRS footprint, an additional condition (5) on the MODIS cloud fraction is imposed, in order to have a completely cloudy scene. Similarly to what is done before for CALIOP, the MODIS cloud fraction must be one (i.e. AIRS footprint completely cloudy according to MODIS) or the FOV is discarded. The sixth and last condition in the table filters out all the scenes for which the MODIS radiance in the infrared window (9-11μm, MODIS channel 31) have a variance larger than 10 %. This last condition is applied because, as explained in Section 6.1.2, the non-AIRS data are averaged on the size of the AIRS footprint, but the averaging has sense only if the quantities involved don't change significantly. In fact, the operations performed to obtain such quantities are, in general, the result of non-linear calculations, hence, simply taking the mean of a quantity, could be a source of errors in our analysis.

The database obtained by applying the first four conditions of Table 6.2 is used to test the ability of the dual regression retrieval algorithm to detect clouds, and compare its ability to the MODIS one. For this part of the test, only single layer clouds are considered. This choice is made to avoid the possiblity that, in presence of a cloud overlap, a thick low cloud is detected

instead of the thin one above it. The database derived from the use of the conditions 1-4 of Table 6.2 is called Non-Homogeneous Database (NHDB) in the following of the Chapter.

The detection ability of the DR algorithm is investigated considering CALIOP as the reference. Hence, the detection ability is simply determined by the percentage of the clouds detected by CALIOP (condition: CALIOP cloud fraction equal to 1) that are also seen by the DR algorithm. It is worth noting that, for this purpose, only the identification is taken into account; this means that even if a cloud is seen at an altitude lower than its actual position (determined by CALIOP) it is still considered a positive detection. The same reasoning is applied to the MODIS case, where the detection is considered when the MODIS cloud fraction is equal to one.

In Figure 6.3 the percentage of clouds detected as function of the optical depth is shown for the dual regression retrieval algorithm (blue curve) and for the MODIS cloud products (red curve). From the figure it is possible to observe that the DR algorithm has a higher detection rate for very small optical depths (lower than 0.2), while for values of ODs larger than about 0.7 the percentage is almost 100 %.

Despite this apparent improvement by the DR retrieval in the detection of the optically thinnest clouds, it is to note that this higher ability could be caused by the lower spatial resolution of the sensor, that is, comparing one single AIRS FOV against those 150 or more of MODIS. In fact, having a MODIS cloud fraction equal to one means that all the about 150 FOVs within the AIRS footprint have to be cloudy, that is a far more stringent condition, particularly when optically thin clouds are considered.

After this preliminary investigation, one of the output products of the dual regression algorithm is analyzed. Once again the CALIOP data are used as the reference. The quantity selected for this analysis is the cloud top height. This choice is motivated by the fact that CALIOP measures this quantity with high accuracy and because obtaining other variables than cloud top height from passive instruments is more complicated.

The database used for this analysis, which is called Homogeneous database (HDB), is produced by applying all the conditions of Table 6.2. These more stringent conditions narrow down our ensemble that contains slightly more than 20 000 FOVs, about a third of all the high clouds identified in the NHDB (see Table 6.3).

For each FOV selected applying all the conditions of Table 6.2, the cloud top height difference (ΔCTH) between CALIOP and the DR retrieval (CAL-

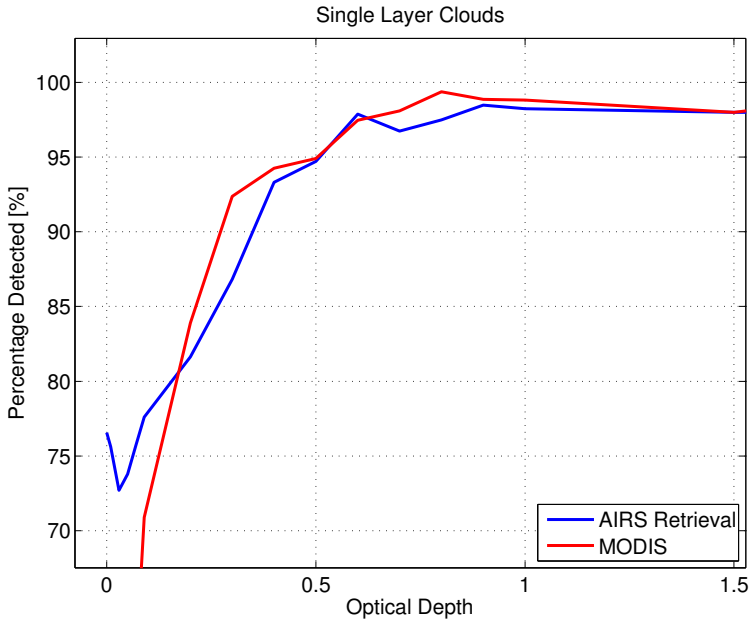

Figure 6.3: Plot of the detection ability for the Dual Regression retrieval (blue curve) and the MODIS data (red curve) for single layer clouds.

RET), and between CALIOP and MODIS (CAL-MOD) is computed, for single layer and multiple layer cases separately. The ΔCTH distributions are shown, using 250 m bins, in Figure 6.4 for single layer clouds (upper panel) and multiple layer clouds (lower panel). Some considerations can be done examining the distributions. Starting from the single layer case, it can be noticed that the mode of the CAL-RET distribution is higher with respect to the CAL-MOD and closer to the zero value, this means that a higher number of clouds are detected at the correct altitude by the dual regression algorithm. Moreover the tails of the distributions indicate the presence of overestimation

Table 6.3: Number of Cloudy FOVs for the two database.

	NHDB	HDB
Single Layer Clouds	12535	2420
Multiple Layer Clouds	44519	20147
Total Clouds	57054	22567

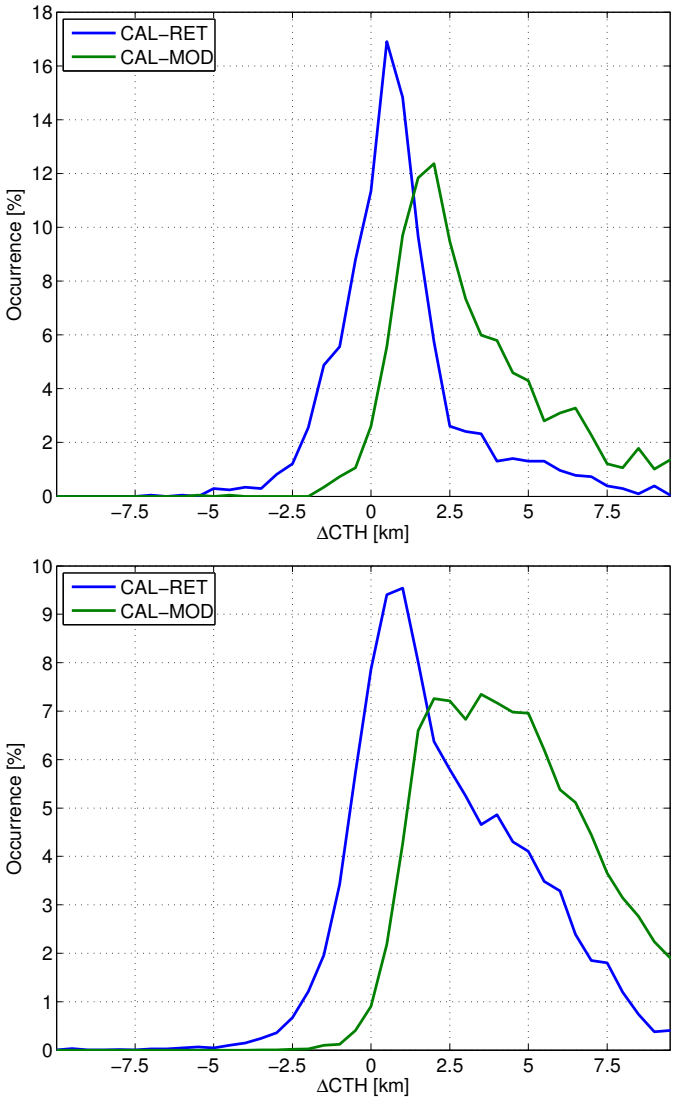

Figure 6.4: Distribution of occurrence of ΔCTH for CALIOP minus the dual regression retrieval (blue curve) and CALIOP minus MODIS (green curve) for single layer clouds (upper panel) and multiple layer clouds (lower panel).

(left side) and underestimation (right side) of the cloud top height by the two methods, thus allowing further considerations. The CAL-MOD distribution shows a higher underestimation of the CTH, that is however present also for

the CAL-RET case. In addition, the dual regression algorithm exhibits a significant percentage of overestimated cloud top height.

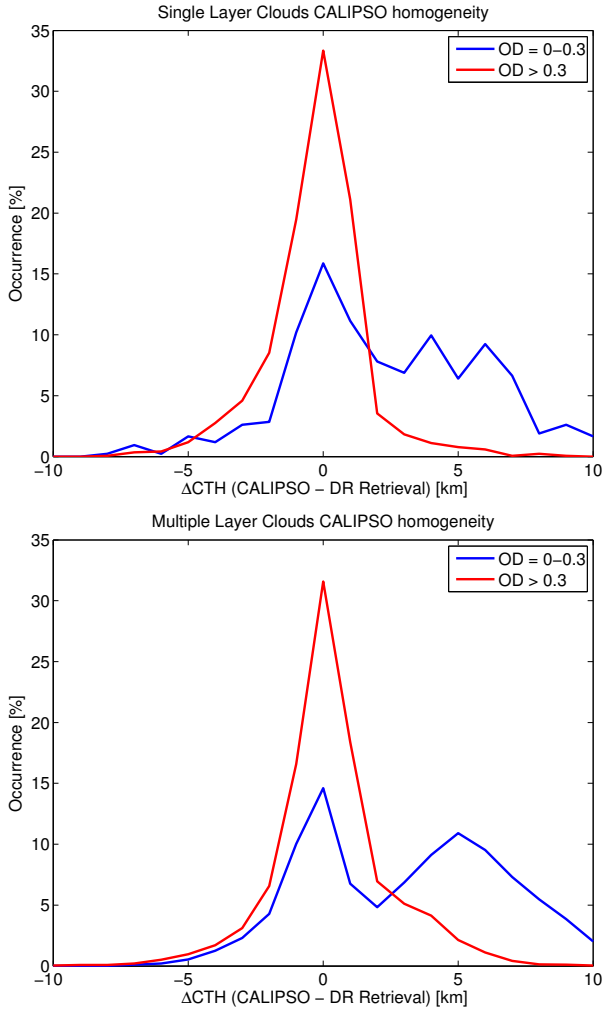

Figure 6.5: Distribution of occurrence of ΔCTH for CALIOP minus the dual regression retrieval with optical depth less than 0.3 (blue curve) and larger than 0.3 (red curve). The upper panel is for the single layer clouds, the lower panel for multiple layer clouds.

A more detailed analysis is thus performed, aiming at understanding what causes the wrong determination of the position of the cloud top for the dual

regression retrieval. The first parameter examined for this purpose is the optical depth, that could be considered the main responsible for the underestimation. The analysis on the optical detph is performed dividing the data set in two OD intervals, one below 0.3, the other above, and then plotting the ΔCTH distribution for the two subsets. The results (see Figure 6.5) show that the largest portion of underestimation occurs for small optical depths. This fact can be explained considering that the signal measured by the sensor can be a composition of emission of the ice cloud under investigation and of the underlying clouds or surface, when an optically thin source is considered. In fact, in such a situation, a passive sensor will measure a higher radiance (that is, a lower cloud top) because of the contribution of warmer sources, that can be a warm cloud or the surface, below the cloud studied.

A variation in the homogeneity condition is also taken into account, in order to avoid that a too permissive condition could lead to the underestimation highlighted in Figure 6.4. At this regard the distributions of ΔCTH are computed again, progressively reducing the homogeneity by 2% steps. The results are shown in the upper panel of Figure 6.6. It is to note that the higher occurrence of underestimated cloud top heights for the most homogeneous case (2% homogeneity, blue curve) can be explained observing the optical depth distributions for the various homogeneity conditions (lower panel of the same figure). The lower panel of Figure 6.6 shows that the highest occurrence of optically thin clouds is found for the most homogeneous case, once again confirming that the optical depth and the underestimation are strictly related.

In addition, also other quantities are taken into account, such as latitude, cloud thickness, and temperature, and analzyed to study if they could be responsible for the underestimation of the CTH. From the analysis, non reported here, emerged that the underestimation cannot be explained by latitude or temperature, while a little influence seems present when the cloud height is considered as can be seen in Figure 6.7. The Figure shows the distribution of the ΔCTH (y-axis) for every bin of cloud geometrical thickness (x-axis) in steps of 0.25 km for the multiple layer clouds case. The color scale represent the occurrence fo each bin. Similar results are found also for the single layer case, not shown here. However, it has been already shown (see Section 4.3) that a correlation exists between geometrical thickness and optical depth. An investigation is performed on the geometrically thin clouds that are underestimated by the DR algorithm and it is confirmed that these clouds are also optically thin.

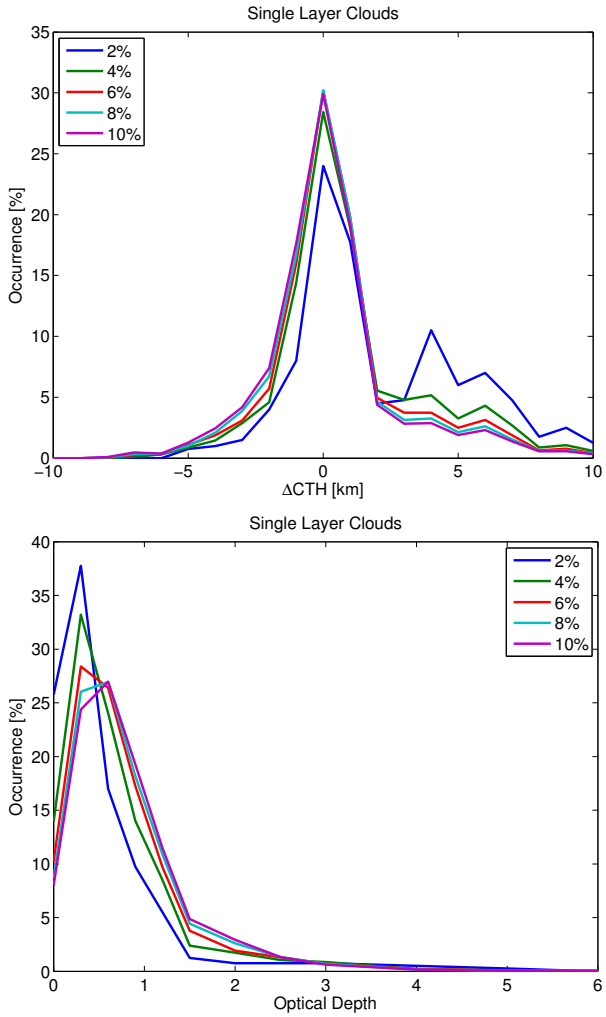

Figure 6.6: Upper panel: distribution of occurrence of the ΔCTH (CALIOP minus DR retrieval), for different levels of homogeneity as reported by the percentages in the legend. Lower panel: distribution of occurrence of the optical depth for the same homogeneity levels of the upper panel.

The overestimation, on the other hand, that is present only for the dual regression algorithm, it is difficult to explain physically and suggests that some issues could be present in the retrieval. As explained in the previous section, the DR algorithm uses two different methodologies (clear and

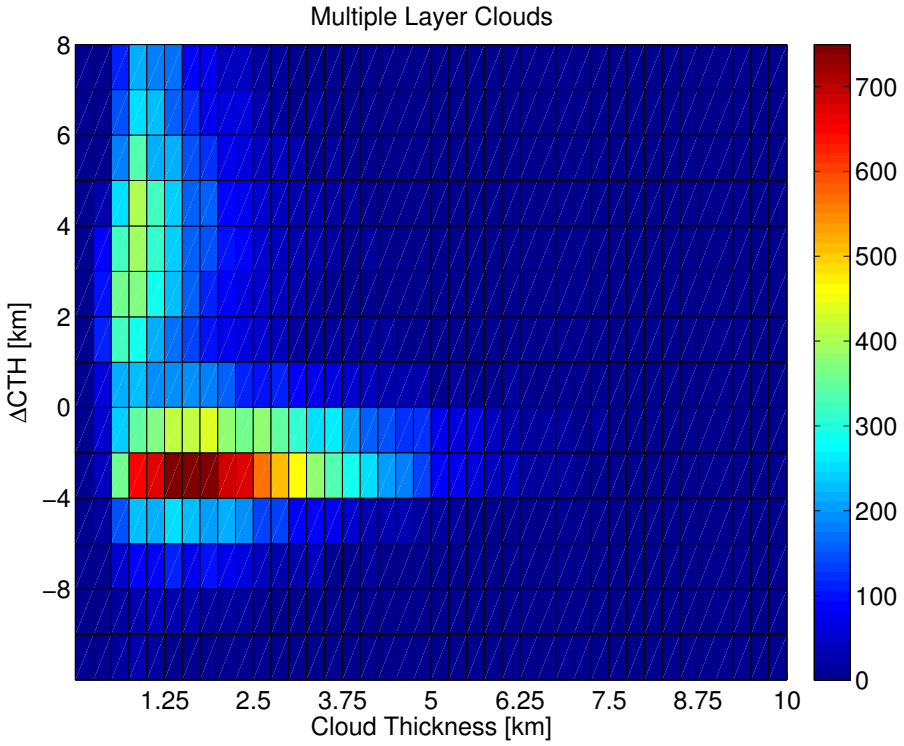

Figure 6.7: Distribution of occurrence of ΔCTH for varying cloud thickness in the multiple layer case. The color scale indicates the counts for each bin.

cloudy temperature profiles comparison and water vapor threshold) to retrieve the cloud top height. The test performed here aims at determining if the overestimation is originated by issues present in one of the two methods. Hence, the code is forced to retrieve the cloud top height with either the temperature profiles comparison or with the relative humidity threshold. The plots in Figure 6.8 show that using the relative humidity threshold results in a large occurrence of overestimation, meaning that the threshold probably needs to be redefined. However also the temperature profile method has a non negligible fraction of overestimation cases.

Recently the issue in the code has been isolated and fixed, and an updated version of the dual regression algorithm is now available (personal communication).

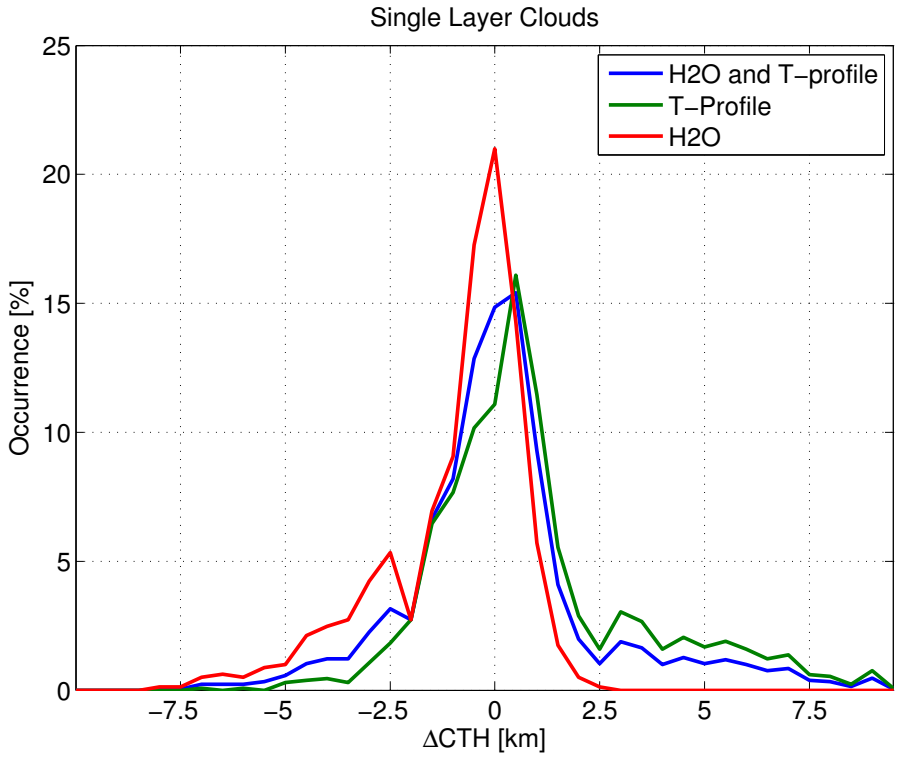

Figure 6.8: Distributions of occurrence of ΔCTH when the dual regression algorithm is forced to use the thermal cloud top (green curve) or the relative humidity threshold (red curve). The blue curve represents the distribution of occurrence fo the standard output of the retrieval, without forcing neither of the two methods.

Chapter 7

Conclusions

7.1 Summary

Vertical variations of cloud features (especially mass) sensibly impact on the clouds and atmospheric energy balance. In particular, cirrus cloud properties along the vertical dimension are poorly known and a better representation of their physical and optical characteristics will be advantageous both for (among others) the derivation of cloud products by inverse algorithms and for forward modeling radiative transfer computations.

The present work aims at contributing to a better knowledge and understanding of the characterization of the ice cloud properties along their vertical extent and shows how this knowledge can be applied to improve inverse and forward radiative transfer calculations. More specifically, one of the goals of this thesis is to provide a statistical analysis of satellite measured backscatter and extinction profile in presence of cirrus clouds. A detailed examination of the shape of vertical backscatter profile (BSP) of ice clouds in the upper troposphere of tropics and midlatitudes is then performed. The results of this analysis are then utilized to perform forward and inverse radiative transfer calculations to test our ability to simulate the far infrared scattering properties.

Measurements collected by the CALIOP lidar on-board of the Cloud-Aerosol Lidar and Infrared Pathfinder Satellite Observations (CALIPSO) during the year 2008 over the oceans are considered. A data set is built containing clouds with maximum optical depth of 2, so that the full cloud vertical extent is characterized by CALIOP measures and possible total at-

tenuation effects on the backscatter signal are avoided. Cirrus cloud covered fields of view are selected even if multilayered clouds are detected, provided that the cirrus is the highest cloud sensed by CALIOP. The number of cases accounted for covers more than 33 % of all the CALIOP fields of view (with spatial resolution equals to 5 km) from 60° S to 60° N, denoting a widespread presence of high, thin, iced layers over large part of the ocean's globe.

Among these cases, only those with nearly homogeneous cloud top and base altitude (derived from an analysis at the higher spatial resolution of 1 km) are considered for the investigation of the shape of CALIOP backscatter and extinction profiles. The selection of horizontally homogeneous cirrus clouds only is performed to avoid possible artifacts in the definition of climatological BSPs. Homogeneous cirri are present in the 6–9 % of the CALIOP 5-km fields of view that is about one-fourth of all the detected cirrus clouds. For the first time, distributions of physical features of homogeneous cirrus clouds are provided for tropics and midlatitudes and daytime and nighttime and compared to the whole ensemble of cirri.

The selected BSPs are first vertically rescaled to a standard length and to a specific number of points and then their areas (from cloud-base to cloud-top altitude) are normalized. In this way, a comparison among the shapes of BSPs that differ in the number of scattering layers and in the total amount of energy backscattered to the lidar is made possible.

Midlatitude and tropical data, such as daylight and nighttime measurements, are analyzed separately due to distinctive mean cloud physical characteristics. In particular, it is observed that horizontally homogeneous tropical cirri have higher mean top height and midpoint temperature, and lower optical depth with respect to midlatitude ones. Distributions of geometrical thickness are very similar at the two latitudes, but differ from day and night showing frequently larger depths for the nighttime case.

Annual means of BSPs are very similar for tropics and ML while noticeable differences are found when daylight and nighttime data are compared. The monthly averages of the shape of the BSPs are all very similar and the dependence on the time of the year is then neglected.

The relationship between the shape of the measured BSPs and cloud and environmental physical parameters (such as cloud optical depth, geometrical thickness and temperature) is investigated. Possible influences of the instrument and retrieval algorithms on the shape of the BSPs (i.e., possible attenuation correction errors in deriving backscattering and extinction coefficients) are not accounted for, but the reader should be aware of this

possibility.

It is found that the cloud geometrical thickness is the main parameter affecting the shape of the mean CALIOP BSP. Specifically, cirrus clouds with thin geometrical thicknesses (less than 2 or 3 km depending on the period of the day) show that a maximum in the normalized BS profile is placed near cloud top. As the cloud geometrical thickness increases the maximum of the mean BSP curve is shifted towards the cloud base. Nighttime and daytime data show some differences even when cirrus clouds within the same thickness are compared, suggesting that possibly different physical features characterizing the two cases might influence the shape of the BSP.

Similarly to what was found for the geometrical thickness also the optical depth analysis shows that the maximum in the shape of the mean BS curves is close to the cloud top for clouds with very thin optical depth and to the base for the optically thickest clouds of the database. It is observed that a monotonic geometrical thickness – optical depth dependence characterizes the ensemble of cirrus clouds under study. In this regard, a parameterization that derives mean optical depth (and its standard deviation) as function of the cloud geometrical thickness is provided.

To minimize the cloud geometrical thickness – optical depth dependence, mean BSPs are computed for cirrus clouds with nearly constant geometrical thickness and multiple optical depth intervals. Results show limited variability of the mean BSPs compared to that found when mean BSPs of cirrus clouds with constant OD and varying geometrical thickness are computed.

The effects of cloud temperature and of temperature gradients within the cloud on the shape of the BSPs are also investigated. Results show a smaller influence of the temperature parameter with respect to the geometrical thickness.

It is observed that the BSP maximum slightly increases as the cloud temperature decreases and as the optical depth increases.

Analytical functions are provided to fit the mean BSPs so that climatological backscatter profiles can be easily used in forward or inverse models. It is, in fact, demonstrated that under certain (realistic) assumptions, which are consistent with assumptions made in the CALIOP retrieval algorithm, the mean backscatter (and extinction) profile is linearly proportional to the cloud IWC profile. Since temperature and cloud optical depth produce second-order effects on the shape of backscatter profile and since the shape of BSPs for varying geometrical thickness shows very limited dependence on latitude, the BSP parameterization in terms of varying geometrical thickness

is given for day and night data only.

The parameterization of the ice-water-content distribution is implemented into the cloud properties retrieval code RT-RET, that is utilized for the derivation of the cloud optical depths and effective dimensions from REFIR-PAD radiances in the main infared window (820-960 cm^{-1}). A mixture of habits typical of midlatitude cirrus clouds is assumed for the retrieval. The derived optical depths, for the eight REFIR-PAD FOVs studied, are consistent with those derived by a lidar distant about 7 km from the measurements site.

The use of a realistic vertical distribution of ice content aims at the reduction of the uncertainties related with the radiative transfer computations. Another aspect that can affect the calculations is the representation of the scattering phase function. For this reason, this parameter is provided with high accuracy by using a truncated series of Legendre polynomials with a large number of coefficients.

The RT-RET derived parameters (i.e. optical depth and effective dimensions) are used to run the forward simulations of the observed cloudy scenes over the whole REFIR-PAD spectrum. It is shown that for each FOV the difference between the simulations and the measurements is always within the spectral uncertainties for the 820–1000 cm^{-1} interval. Only for the FOV number 24, where the optical depth is the smallest, the differences between simulations and measurements are almost completely within the uncertainties also in the FIR.

The differences between the simulations and the REFIR-PAD measurements are also investigated in six selected far-infrared micro-windows for all the FOVs. Again a good agreement between simulation and data is found for FOV 24 and a worsening of the simulation is observed for FOV 24 through 27. The FOV from 28 to 31 shows the largest spread among the various micro-windows and the simulations minus data differences range between -4 and 2 $\mathrm{mW/m^2cm^{-1}sr}$.

Differences between the simulations and the measurements are performed also for five selected water vapor highly absorptive channels. The results show a general underestimation of the downwelling radiance of the order of -1 $\mathrm{mW/m^2cm^{-1}sr}$ that can provide an idea of the uncertainties associated to radiance simulations due to the assumption on temperature and water vapor profiles close to the ground station.

A sensitivity study is conducted on the cloud particle shape. For this reason a particle size distribution containing hexagonal columns is used as

a priori assumption in the RT-RET retrieval. The assumption of pristine hexagonal columns results in larger values of the simulated radiance that, in most cases, corresponds to a decrease in the simulation–data difference value. The result is anyway not conclusive since for some FOVs the simulation worsens independently of the selected micro-window.

The sensitivity of the simulation to a variation of relative humidity is investigated. For the FOV 27 a new forward simulation is performed with an increase in the relative humidity value of 10 % at all atmospheric levels with respect to the standard simulation. The results show a difference between the two simulation with a maximum value of 1.5 $\mathrm{mW/m^2cm^{-1}sr}$ for the less transparent windows. It is observed that the sensitivity to water vapor relative humidity is the highest where the sensitivity to cloud particle habits is the lowest and vice-versa. Nevertheless, for most cases, the differences between the simulations are not sufficient to explain the residuals between data and simulations.

The radiance differences that a satellite sensor, with the same REFIR-PAD spectral resolution, would detect observing the same scene of FOV 27 are computed. The results show very small differences, that are mostly due to the fact that the cloud is high in the atmosphere where the absorption/emission from water vapor is of minor extent. This demonstrates that a satellite view configuration would be of great advantage for the study of the optical properties of ice clouds in the far infrared.

In the end, the problem of merging data products from different satellite-borne sensors with diverse geometries of observation is discussed. A procedure that puts together the products of AIRS, MODIS and CALIOP is developed and applied to about two weeks of data.

The collocated dataset is then exploited to perform some preliminary tests on a new hyperspectral infrared retrieval and compare its results with those of the MODIS cloud products (MOD06). Initially it is shown that the detection ability of the dual regression algorithm, is higher for the optically thinnest clouds (i.e. optical depth less than 0.1) than that of MODIS.

The ability of the dual regression algorithm to retrieve the cloud top height is analyzed considering the value of this quantity provided by the CALIOP products as the reference. For this purpose the distribution of the cloud top height differences between CALIOP and the DR algorithm are computed. The results show that the dual regression algorithm in general is able to detect the CTH with more accuracy than the MODIS cloud products. It is however higlighted the presence of overestimation as well as underestimation

of the cloud top height in both single and multiple layer cloud scenes.

The undestimation is shown to be of minor entity with respect to the MODIS case and it is mainly caused by the optically thinnest clouds, namely those with optical depth lower than 0.3. The overestimation on the other hand, almost absent in the MODIS data, cannot be explained physically and could indicate an issue within the dual regression algorithm. This issue is investigated by the group that developed the code and a new version is recently made available.

7.2 Open problems and future works

The work described in this thesis extends the knowledge of some aspects of the study of ice clouds, presenting for the first time a study on their vertical features. Furthermore also the scattering properties in the far infrared part of the electromagnetic spectrum are investigated for these clouds. Both these aspects at the moment are poorly explored, nevertheless they are important for improving the comprehension of scattering processes within ice clouds.

The results described in Chapter 4, concerning the vertical properties of cirrus clouds, can be used, as shown for a case study in this thesis, to improve both direct and inverse radiative transfer calculations.

Moreover, the statistical CALIOP backscatter profiles can be used to validate the general circulation models by looking if the vertical distribution of ice content within cirrus clouds is reproduced according to what observed by the lidar.

The importance of having simultaneous measurements of the same scene in different regions of the electromagnetic spectrum has been stressed and motivated many times in this work. The development of a methodology for the collocation of satellite products can provide a new and valuable tool for the future studies on clouds. The availability of a collocated data set that covers diverse portions of the electromagnetic spectrum can be useful for the analysis and improvement of retrieval techniques.

The analysis performed on the dual regression algorithm is just a starting point of possible future investigations that could highlight which are the most difficult conditions to perform a retrieval and thus where the largest efforts are to be addressed for improving the results.

Furthermore, a collocated data set can be exploited in the intercomparison between sensors whose products and measurements have been proven

reliable and new sensors, such as, for instance, the most recent Cross-track Infrared Sounder (CrIS), that still requires some tuning before their data can be made available with a good confidence on their quality.

Appendix A

Definition of the minimum number of elements defining the data subset

In Sect. 4.1 it is shown that the variability among measured profiles can be very large. Nevertheless, averages performed over sufficiently large subsets (i.e. over one month of data or one season) converge to well defined mean curves.

It is our goal to find how many profiles (N) are needed to obtain a mean profile which is representative of an ideally infinite set of data of the same type. The problem arises when the full data set under study (the HCCD) is divided into smaller subsets and statistical analysis are performed on a limited number of profiles. The question that we are trying to answer in this Appendix is the following: is the subset well representative of an ideally infinite number of backscatter profiles of cirrus clouds with similar characteristics?

The minimum number of profiles, N, which is accepted in order to apply a statistical analysis, is computed with the following methodology. Given the full data set of cirrus BS profiles, the number of elements required to obtain a mean BSP "sufficiently close" to the one derived from the entire data set is evaluated. A sufficient closeness among the means (of the subset and of the full extended database) is defined through the $\mathcal{I}_\Delta$ which must be less than 1 %.

The mean of the subset is computed as:

$$\langle \beta_s(z_i) \rangle = \frac{1}{N} \sum_{j=1}^{N} \beta_j(z_i) \tag{A.1}$$

where the N BSPs are selected randomly within the whole data set. The value found in equation A1 is computed M different times ($M = 1000$ in our case), i.e. for M (1000) distinct subsets of N randomly selected profiles. Each time the mean of the subset is compared to the mean of the entire data set and an $\mathcal{I}_\Delta$ is computed. Then the average of the difference index is computed:

$$\langle \mathcal{I}_\Delta \rangle = \frac{1}{M} \sum_{m=1}^{M} \mathcal{I}_{\Delta,m} \tag{A.2}$$

The entire procedure is iterated. N is increased at each step until the value of $\langle \mathcal{I}_\Delta \rangle$ is less than 1 %.

This methodology, applied to the cirrus cloud data set used in this work, provides a value for N that is of the order of 1500. This will be the minimum number of profiles in our subsets that is required to perform averaging operations.

Appendix B

Quality check on cirrus database

The extinction retrieval Quality Check (QC) was not used for data selection of this work. The exclusion of this flag is however justified by the following analysis.

First of all the percentage of the profiles of the HCCD which have extinction retrieval QC = 0 or 1 is computed. The values vary from a minimum of 48% for midlatidues in daylight to a maximum of 71% at tropics during night. In Table B.1 the occurrence is shown for all the cases.

Table B.1: Occurrence of QC=0 or 1 profiles in HCCD.

Region and Period	Percentage
Midlatitudes Day	48%
Midlatitudes Night	59%
Tropics Day	62%
Tropics Night	71%

Then the distributions of occurrence as function of geometrical thickness (and total cloud OD) for the 4 cases (MLD, MLN, TRD and TRN) of the HCCD are compared with the corresponding distributions for profiles flagged QC = 0 or 1 only (MLDQC, MLNQC, TRDQC and TRNQC). Results show that the main differences arise for the largest geometrical depths and optical thicknesses (as expected due to degradation of the backscatter signal for those cases). In Figure B.1 the distributions of occurrence as function of the

geometrical thickness are shown for the midlatitudes and tropics in the upper and lower panel respectively.

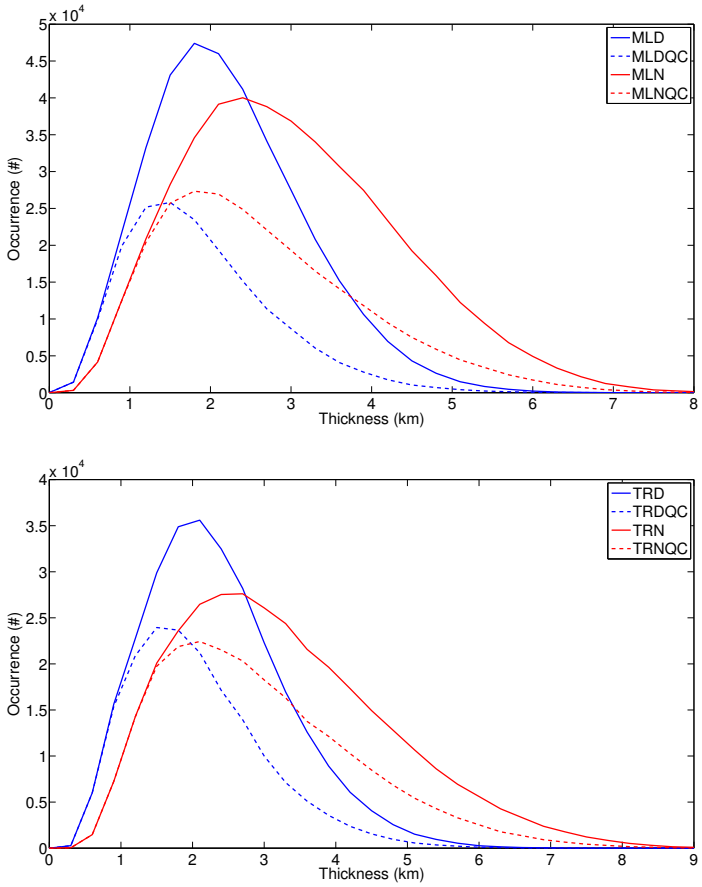

Figure B.1: Distribution of occurrence as function of the geometrical thickness for the midlatitude region (upper panel) and tropical region (lower panel). In both panels the blue curves are for the daytime case and the red curves for the nighttime case. Solid lines represent the distributions for the homogeneous cirrus cloud database (HCCD), dashed lines represent the HCCD with the restrictions on the Quality Check (QC = 0 or 1 only).

A comparison between mean BSP, obtained from the HCCD, before and after the use of the QC condition was then performed. For each region and period of the day it was found that the mean BSPs don't change significantly.

The highest value of the difference index is about 7%. In Table B.2 the difference index, computed as the difference HCCD without QC minus HCCD with QC, for all the cases is shown.

Table B.2: Difference indexes between databases without and with the use of the QC flag.

Region and Period	Difference Index
Midlatitudes Day	7%
Midlatitudes Night	2%
Tropics Day	5%
Tropics Night	3%

In Figure B.2 the results for the midlatitude and tropical cases are presented in the upper and lower panel respectively.

The same comparison was then performed for a subset containing only clouds of the HCCD with OD > 0.6 and DZ > 2 km. The percentage of the profiles having OD > 0.6, $\Delta z > 2$ km and QC $= 0$ or 1 is about 36%. In Table B.3 the percentages for each region and period of the day are reported with the corresponding difference indexes computed similarly to what done for the Table B.2.

Table B.3: Occurrence of cirrus clouds with the use of the QC flag.

Region and Period	Occurrence	Difference Index
Midlatitudes Day	25%	4%
Midlatitudes Night	38%	7%
Tropics Day	35%	4%
Tropics Night	46%	8%

Since these differences are very small it is reasonable to conclude that for the considered data set the QC flag is of minor importance. Moreover, the same results also suggest that the differences found in Table B.2 (again very small) are mostly due to a change in the frequency distributions of the new subsets (MLDQC, MLNQC, TRDQC and TRNQC) rather than to a different quality of the BSPs of the MLDQC, MLNQC, TRDQC and TRNQC subsets.

It is to note that, reducing the HCCD to BSPs with QC $= 0$ or 1 only, would strongly reduce the number of optically and geometrically thickest

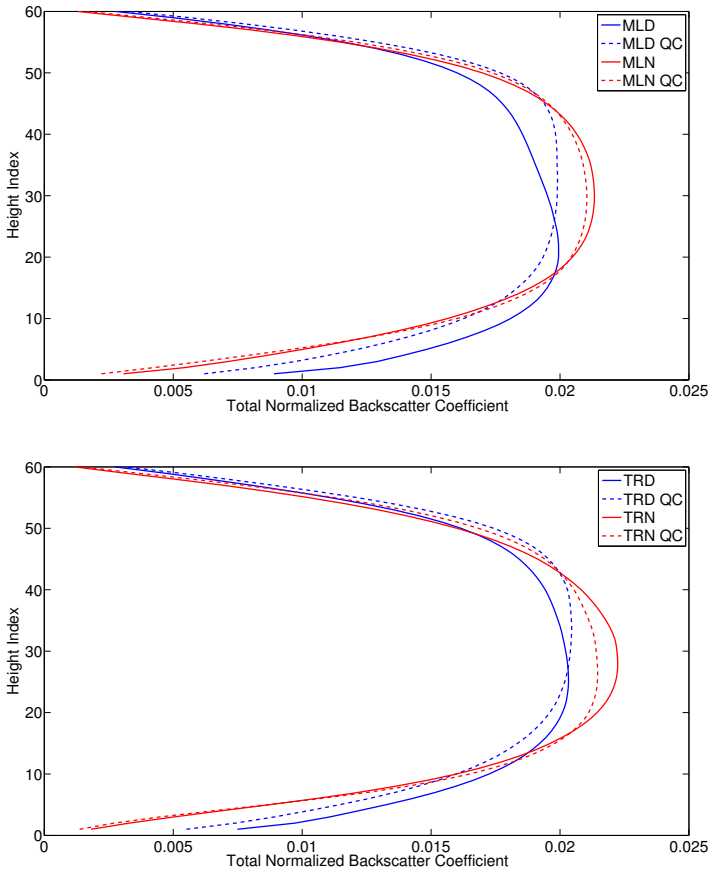

Figure B.2: Mean backscatter profiles for the midlatitude region (upper panel) and for the tropical region (lower panel). For both panels the daytime case is shown with blue curves while the nighttime case with red curves. The solid lines represent the mean BSP for the HCCD without restriction on the QC, the dashed lines represent the mean BSP for the subset of the HCCD with QC = 0 or 1.

clouds and thus would make very difficult to perform a statistically relevant analysis of the BSPs for multiple geometrical depth and optical depth classes.

Bibliography

Ackerman, S., Strabala, K., Menzel, W. P., Frey, R., Moeller, C., Gumley, L., Baum, B., Wetzel Seemann, S., and Zhang, H. (2006). *Discriminating clear-sky from cloud with MODIS. Algorithm Theoretical Basis Document (MOD35).* CIMSS, NOAA/NESDIS, NASA/LaRC.

Anderson, G. P., Chetwynd, J. H., Clough, S. A., Shettle, E. P., and Kenizys, F. X. (1986). Afgl atmospheric consituent profiles (0-120km). Technical report, U.S. Air Force Geophysics Laboratory, Hanscom Air Force Base, MA 01731.

Aumann, H. H. and Miller, C. (1995). Atmospheric infrared sounder (AIRS) on the earth observing system. *SPIE*, 2583.

Baker, B. A. and Lawson, R. P. (2006). In situ observations of the microphysical properties of wave, cirrus, and anvil clouds. part I: Wave clouds. *Journal of the Atmospheric Sciences*, 63.

Baran, A. J. (2009). A review of the light scattering properties of cirrus. *Journal of Quantitative Spectroscopy & Radiative Transfer*, 110:1239–1260.

Baran, A. J., Bodas-Salcedo, A., Cotton, R., and Lee, C. (2011). Simulating the equivalent radar reflectivity of cirrus at 94 GHz using an ensemble of cirrus ice crystals: a test of the Met Office global numerical weather prediction model. *Quarterly Journal of the Royal Meteorological Society*, 137(659):1547–1560.

Baum, B. A., Heymsfield, A. J., Yang, P., and Bedka, S. T. (2005a). Bulk scattering properties for the remote sensing of ice clouds. part I: Microphysical data and models. *Journal of Applied Meteorology*, 44.

Baum, B. A., Menzel, W. P., Frey, R. A., Tobin, D. C., Holz, R. E., Ackerman, S. A., Heidinger, A. K., and Yang, P. (2012). MODIS cloud-top property refinement for collection 6. *Journal of Applied Meteorology and Climatology*, 51.

Baum, B. A., Yang, P., Heymsfield, A. J., Platnick, S., King, M. D., Hu, Y. X., and Bedka, S. T. (2005b). Bulk scattering properties for the remote sensing of ice clouds. part II: Narrowband models. *Journal of Applied Meteorology*, 44.

Baum, B. A., Yang, P., Heymsfield, A. J., Schmitt, C. G., Xie, Y., Bansemer, A., Hu, Y.-X., and Zhang, Z. (2011). Improvements in shorwave bulk scattering and absorption models for the remote sensing of ice clouds. *Journal of Applied Meteorology and Climatology*, 50(5):1037–1056.

Baum, B. A., Yang, P., Hu, Y.-X., and Feng, Q. (2010). The impact of ice particle roughness on the scattering phase matrix. *Journal of Quantitative Spectroscopy & Radiative Transfer*, 111:2534–2549.

Berthier, S., Chazette, P., Pelon, J., and Baum, B. (2008). Comparison of cloud statistics from spaceborne lidar systems. *Atmospheric Chemistry and Physics*, 8.

Bhawar, R., Bianchini, G., Bozzo, A., Calvello, M. R., Cacciani, M., Carlotti, M., Castagnoli, F., Cuomo, V., Di Girolamo, P., Di Iorio, T., Di Liberto, L., di Sarra, A., Esposito, F., Fiocco, G., Fuà, D., Grieco, G., Maestri, T., Masiello, G., Muscari, G., Palchetti, L., Papandrea, E., Pavese, G., Restrieri, R., Rizzi, R., Romano, F., Serio, C., Summa, D., Todini, G., and Tosi, E. (2008). Spectrally resolved observations of earth's emission spectrum in the h2o rotation band. *Geophysical Research Letters*, 35.

Bhawar, R., Di Girolamo, P., Summa, D., Flamant, C., Althausen, D., Behrendt, A., Kiemle, C., Bosser, P., Cacciani, M., Champollion, C., Di Iorio, T., Engelmann, R., Herold, C., Müller, D., Pal, S., Wirth, M., and Wulfmeyer, V. (2011). The water vapour intercomparison effort in the framework of the convective and orographically-induced precipitation study: airborne-to-ground-based and airborne-to-airborne lidar systems. *Quarterly Journal of the Royal Meteorological Society*, 137:325–348.

Bianchini, G. and Palchetti, L. (2008). Technical note: REFIR-PAD level 1 data analysis and performance characterization. *Atmospheric Chemistry and Physics*, 8.

Bianchini, G., Palchetti, L., Baglioni, A., and Castagnoli, F. (2007). Far-infrared spectrally resolved broadband emission of the atmosphere from morello and gomito mountains near florence. *Proceedings of SPIE*, 6745.

Bianchini, G., Palchetti, L., and Carli, B. (2006). A wide-band nadir-sounding spectroradiometer for the characterization of the earth's outgoing long-wave radiation. *Proceedings of SPIE*, 6361.

Bianchini, G., Palchetti, L., and Carli, B. (2009). Vectorial combination of signals in fourier transform spectroscopy. *Infrared Physics & Technology*, 52.

Bianchini, G., Palchetti, L., Muscari, G., I, F., Di Girolamo, P., and Di Iorio, T. (2011). Water vapor sounding with the far infrared REFIR-PAD spectroradiometer from a high-altitude ground-based station during the ECOWAR campaign. *Journal of Geophysical Research*, 116.

Bozzo, A., Maestri, T., and Rizzi, R. (2010). Combining visible and infrared radiometry and lidar data to test simulations in clear and ice cloud conditions. *Atmospheric Chemistry and Physics*, 10:7369–7387.

Bozzo, A., Maestri, T., Rizzi, R., and Tosi, E. (2008). Parameterization of single scattering properties of mid-latitude cirrus clouds for fast radiative transfer models using particle mixtures. *Geophysical Research Letters*, 35.

Cattrall, C., Reagan, J., Thome, K., and Dubovik, O. (2005). Variability of aerosol and spectral lidar and backscatter extinction ratios of key aerosol types derived from selected aerosol robotic network locations. *Journal of Geophysical Resarch*, 110.

Chahine, M. T., Pagano, T. S., Aumann, H. H., Atlas, R., Barnet, C., Blaisdell, J., Chen, L., Divakarla, M., Fetzer, E. J., Goldberg, M., Gautier, C., Granger, S., Hannon, S., Irion, F. W., Kakar, R., Kalnay, E., Lambrigtsen, B. H., Lee, S.-Y., Marshall, J. L., McMillan, W. W., McMillin, L., Olsen, E. T., Revercomb, H., Rosenkranz, P., Smith, W. L., Staelin, D., Strow,

L. L., Susskind, J., Tobin, D., Wolf, W., and Zhou, L. (2006). AIRS improving weather forecasting and providing new data on greenhouse gases. *Bulletin of the American Meteorological Society*, 87.

Chiriaco, M., Chepfer, H., Noel, V., Haeffelin, M., and Drobinski, P. (2006). Dual lidar observations at 10.6 μm and 532 nm for retrieving semitransparent cirrus cloud properties. *Journal of Applied Meteorology and Climatology*, 45.

Clough, S. A., Iacono, M. J., and Moncet, J.-L. (1992). Line-by-line calculations of atmospheric fluxes and cooling rates: Application to water vapor. *Journal of Geophysical Research*, 97(15):761–785.

Clough, S. A., Shephard, M. W., Mlawer, E. J., Delamere, J. S., Iacono, M. J., Cady-Pereira, K., Boukabara, S., and Brown, P. D. (2005). Atmospheric radiative transfer modeling: a summary of the AER codes. *Journal of Quantitative Spectroscopy & Radiative Transfer*, 91:233–244.

Cox, C. V., Harries, J. E., Taylor, J. P., Green, P. D., Baran, A. J., Pickering, J. C., Last, A. E., and Murray, J. E. (2010). Measurements and simulation of mid- and far-infrared spectra in the presence of cirrus. *Quarterly Journal of the Royal Meteorological Society*, 136:718–739.

Delamere, J. S., Clough, S. A., Payne, V. H., Mlawer, E. J., Turner, D. D., and Gamache, R. R. (2010). A far-infrared radiative closure study in the arctic: application to water vapor. *Journal of Geophysical Research*, 115.

Di Girolamo, P., Behrendt, A., and Wulfmeyer, V. (2006). Spaceborne profiling of atmospheric temperature and particle extinction with pure rotational raman lidar and of relative humidity in combination with differential absorption lidar: performance simulations. *Applied Optics*, 45:2474–2494.

Di Girolamo, P., Cacciani, M., di Sarra, A., Fiocco, G., and Fuà, D. (1994). Lidar observations of the pinatubo aerosol layer at thule, greenland. *Geophysical Research Letters*, 21:1295–1298.

Di Girolamo, P., Marchese, R., Whiteman, D. N., and Demoz, B. B. (2004). Rotational raman lidar measurements of atmospheric temperature in the UV. *Geophysical Research Letters*, 31.

Di Girolamo, P., Summa, D., Bhawar, R., Di Iorio, T., Cacciani, M., Veselovskii, I., Dubovik, O., and Kolgotin, A. (2012a). Raman lidar observations of a saharan dust outbreak event: Characterization of the dust optical properties and determination of particle size and microphysical parameters. *Atmospheric Environment*, 50:66–78.

Di Girolamo, P., Summa, D., Cacciani, M., Norton, E. G., Peters, G., and Dufournet, Y. (2012b). Lidar and radar measurements of the melting layer: observations of dark and bright band phenomena. *Atmospheric Chemistry and Physics*, 12:4143–4157.

Di Girolamo, P., Summa, D., and Ferretti, R. (2009a). Multiparameter raman lidar measurements for the characterization of a dry stratospheric intrusion event. *Journal of Atmospheric and Oceanic Technology*, 26:1742–1762.

Di Girolamo, P., Summa, D., Lin, R.-F., Maestri, T., Rizzi, R., and Masiello, G. (2009b). UV raman lidar measurements of relative humidity fot the characterization of cirrus cloud microphysical properties. *Atmospheric Chemistry and Physics*, 9(8799-8811).

Di Giuseppe, F. and Rizzi, R. (1999). Far infrared scattering effects in cloudy sky. *Physics and chemistry of the Earth, Part B: Hydrology, Oceans and Atmosphere*, 24(3):243–247.

Eguchi, N., Yokota, T., and Inoue, G. (2007). Characteristics of cirrus clouds from ICESat/GLAS observations. *Geophysical Research Letters*, 34.

Esposito, F., Grieco, G., Masiello, G., Pavese, G., Restieri, G., Serio, C., and Cuomo, V. (2007). Intercomparison of line-parameter spectroscopic databases using downwelling spectral radiance. *Quarterly Journal of the Royal Meteorological Society*, 133:191–202.

Evans, K. F. and Stephens, G. L. (1991). A new polarized atmospheric radiative transfer model. *Journal of Quantitative Spectroscopy & Radiative Transfer*, 46.

Field, P. R., Heymsfield, A. J., and Bansemer, A. (2007). Snow size distribution parameterizaion for midlatitude and tropical ice clouds. *Journal of the Atmospheric Sciences*, 64.

Field, P. R., Heymsfield, A. J., Bansemer, A., and Twohy, C. H. (2008). Determination of the combine ventilation factor and capacitance for ice crystals aggregates from airborne observations in a tropical anvil cloud. *Journal of the Atmospheric Sciences*, 65.

Field, P. R., Hogan, R. J., Brown, P. R. A., Illingworth, A. J., Choularton, T. W., and Cotton, R. J. (2005). Parametrization of ice-particle size distributions for mid-latitude stratiform cloud. *Quarterly Journal of the Royal Meteorological Society*, 131.

Fiorucci, I., Muscari, G., Bianchi, C., Di Girolamo, P., Esposito, F., Grieco, G., Summa, D., Bianchini, G., Palchetti, L., Cacciani, M., Di Iorio, T., Pavese, G., Cimini, D., and de Zafra, R. L. (2008). Measurements of low amounts of precipitable water vapor by millimeter wave spectroscopy: An intercomparison with radiosonde, raman lidar, and fourier transform infrared data. *Journal of Geophysical Research*, 113.

Fu, Q. (2007). A new parameterization of an asymmetry factor of cirrus clouds for climate models. *Journal of the Atmospheric Sciences*, 64.

Green, P. D., Newman, S. M., Beeby, R. J., Murray, J. E., Pickering, J. C., and Harries, J. E. (2012). Recent advances in measurement of the water vapour continuum in the far-IR spectral region. *Philosophical Transaction of the Royal Society A*, 370:2637–2655.

Griaznov, V., Veselovskii, I., Di Girolamo, P., Korenskii, M., and Summa, D. (2007). Spatial distribution of doubly scattered polarized laser radiation in the focal plane of a lidar receiver. *Applied Optics*, 46:6821–6830.

Ham, S.-H., Sohn, B.-J., and Baum, B. A. (2009). Assessment of the quality of MODIS cloud products from radiance simulations. *Journal of Applied Meteorology and Climatology*, 48:1591–1612.

Harries, J., Carli, B., Rizzi, R., Serio, C., Mlynczak, M., Palchetti, L., Maestri, T., Brindley, H., and Masiello, G. (2008). The far-infrared earth. *Reviews of Geophysics*, 46.

Hartmann, D. L. (1994). *Global Physical Climatology*. Academic Press.

Heymsfield, A. J. (2003). Properties of tropical and midlatitude ice cloud particle ensembres. part II: Applications for mesoscale and climate models. *Journal of the Atmospheric Sciences*, 60.

Heymsfield, A. J., Lewis, S., Bansemer, A., Iaquinta, J., Miloshevich, L. M., Kajikawa, M., Twohy, C. H., and Poellot, M. R. (2002). A general approach for deriving the properties of cirrus and stratiform ice cloud particles. *Journal of the Atmospheric Sciences*, 59.

Heymsfield, A. J. and Miloshevich, L. M. (1995). Relative humidity and temperature influences on cirrus formation and evolution: observations from wave clouds and FIRE II. *Journal of the Atmospheric Sciences*, 52.

Heymsfield, A. J. and Miloshevich, L. M. (2003). Parameterizations for the cross-sectional area and extincion of cirrus and stratiform ice cloud particles. *Journal of the Atmospheric Sciences*, 60.

Holton, J. R. (2004). *An Introduction to Dynamic Meteorology*. Elsevier Academic Press.

Hostetler, C. A., Liu, Z., Reagan, J., Vaughan, M. A., Winker, D. M., Osborn, M., Hunt, W. H., Powell, K. A., and Trepte, C. (2006). *CALIOP Algorithm Theoretical Basis Document. Calibration and Level 1 Data Products*. NASA.

IPCC (2007). *Climate change 2007 - The physical science basis: Contribution of working group I to the fourth assessment report of the IPCC*. Cambridge University Press.

Ivanova, D., Mitchell, D. L., Arnott, W. P., and Poellot, M. (2001). A GCM parameterization for bimodal size spectra and ice mass removal rates in mid-latitude cirrus clouds. *Atmospheric Research*, 59.

King, M. D., Menzel, W. P., Grant, P. S., Myers, J. S., Arnold, G. T., Platnick, S. E., Gumley, L. E., Tsay, S.-C., Moeller, C. C., Fitzgerald, M., Brown, K. S., and Osterwisch, F. G. (1996). Airborne scanning spectrometer for remote sensing of cloud, aerosol, water vapor, and surface properties. *Journal of Atmospheric and Oceanic Technology*, 13:777–794.

King, M. D., Tsay, S. C., Platnick, S. E., Wang, M., and Liou, K. N. (1997). MODIS algorithm theoretical basis document no. ATBD-MOD-05 MOD06 cloud product. Technical report, NASA MODIS Science Team.

Korolev, A. V., Emery, E. F., Strapp, J. W., Cober, S. G., Isaac, G. A., Wasey, M., and Marcotte, D. (2011). Small ice particles in tropospheric clouds: Fact or artifact? airborne icinc instrumentation evaluation experiment. *Bulletin of the American Meteorological Society*, 92.

Lawson, R. P., Baker, B. A., Pilson, B., and Mo, Q. (2006). In situ observations of the microphysical properties of wave, cirrus and anvil clouds. part II: Cirrus clouds. *Journal of Atmospheric Sciences*, 63.

Liou, K.-N. (1986). Influence of cirrus clouds on weather and climate processes: A global perspective. *Monthly Weather Review*, 114.

Liou, K.-N. (1992). *Radiation and Cloud Processes in the Atmosphere*. Oxford University Press.

Liu, Z., Omar, A. H., Hu, Y., Vaughan, M. A., and Winker, D. M. (2005). *CALIOP Algorithm Theoretical Basis Document. Part 3: Scene Classification Algorithms*. NASA.

Lynch, D. K., Sassen, K., Starr, D. O., and Stephens, G. L. (2002). *Cirrus*. Oxford University Press, Inc.

Maestri, T., Di Girolamo, P., Summa, D., and Rizzi, R. (2010). Clear and cloudy sky investigations using raman lidar and airborne interferometric measures from the european AQUA thermodynamic experiment. *Atmospheric Research*, 97:157–169.

Maestri, T. and Holz, R. E. (2009). Retrieval of cloud optical properties from multiple infrared hyperspectral measurements: A methodology based on a line-by-line multiple scattering code. *IEEE Transactions on geoscience and remote sensing*, 47.

Maestri, T. and Rizzi, R. (2003a). A study of infrared diabatic forcing of ice clouds in the trophical amtosphere. *Journal of Geophysical Resarch*, 108.

Maestri, T. and Rizzi, R. (2003b). A study of infrared diabatic forcing of ice clouds in the tropical atmosphere. *Journal of Geophysical Research*, 108.

Maestri, T., Rizzi, R., and Smith, J. A. (2005). Spectral infrared analysis of a cirrus cloud based on airborne research interferometer evaluation system (ARIES) measurements. *Journal of Geophysical Resarch*, 110.

Mannozzi, L., Di Giuseppe, F., and Rizzi, R. (1999). Cirrus clouds optical properties in far infrared. *Physics and chemistry of the Earth, Part B: Hydrology, Oceans and Atmosphere*, 24:269–273.

Martins, E., Noel, V., and Chepfer, H. (2011). Properties of cirrus and subvisible cirrus from nighttime Cloud-Aerosol Lidar with Orthogonal Polarization (CALIOP), related to atmospheric dynamics and water vapor. *Journal of Geophysical Resarch*, 116.

Masiello, G., Serio, C., Esposito, F., and Palchetti, L. (2012). Validation of line continuum spectroscopic parameters with measurements of atmospheric emitted specrtal radiance from far to mid infrared wave number range. *Journal of Quantitative Spectroscopy & Radiative Transfer*, 113:1286–1299.

McFarquhar, G. M., Heymsfield, A. J., Spinhirne, J., and Hart, B. (2000). Thin and subvisual tropopause tropical cirrus: Observations and radiative impacts. *Journal of the Atmospheric Sciences*, 57.

Mertens, C. J., Mlynczak, M. G., Garcia, R. R., and Portmann, R. W. (1999). A detailed evaluation of the stratospheric heat budget: 1. radiation transfer. *Journal of Geophysical Research*, 104(D6):6021–6038.

Mona, L., Cornacchia, C., D'Amico, G., Di Girolamo, P., Pappalardo, G., Pisani, G., Summa, D., Wang, X., and Cuomo, V. (2007). Characterization of the variability of the humidity and cloud fields as observed from a cluster of ground-based lidar systems. *Quarterly Journal of the Royal Meteorological Society*, 133:257–271.

Nagle, F. W. and Holz, R. E. (2008). Computationally efficient methods of collocating satellite, aircraft, and ground observations. *Journal of Atmospheric and Oceanic Technology*, 26.

Naud, C., Russell, J. E., and Harries, J. E. (2001). Remote sensing in cirrus cloud properties in the far infrared. *Proceedings of SPIE*, 4168.

Nazaryan, H., McCormick, M. P., and Menzel, W. P. (2008). Global characterization of cirrus clouds using CALIPSO data. *Journal of Geophysical Resarch*, 113.

Omar, A. H., Won, J.-G., Winker, D. M., Yoon, S.-C., Dubovik, O., and McCormick, M. P. (2005). Development of global aerosol models using cluster analysis of aerosol robotic network (AERONET) measurements. *Journal of Geophysical Resarch*, 110.

Palchetti, L., Barbis, A., Harries, J. E., and Lastrucci, D. (1999). Design and mathematical modelling of the space-borne far-infrared fourier transform spectrometer for REFIR experiment. *Infrared Physics & Technology*, 40.

Palchetti, L., Belotti, C., Bianchini, G., Castagnoli, F., Carli, B., Cortesi, U., Pellegrini, M., Camy-Peyret, C., Jeseck, P., and Té, Y. (2006). Technical note: first spectral measurement of the earth's upwelling emission using an uncooled wideband fourier transform spectrometer. *Atmospheric Chemistry and Physics*, 6.

Palchetti, L., Bianchini, G., Carli, B., Cortesi, U., and Del Bianco, S. (2007). Measurements of the water vapour vertical profile and of the earth's outgoing far infrared flux. *Atmospheric Chemistry and Physics*, 7.

Palchetti, L., Bianchini, G., Castagnoli, F., Carli, B., Serio, C., Esposito, F., Cuomo, V., Rizzi, R., and Maestri, T. (2005). Breadboard of a fourier-transform spectrometer for the radiation explorer in the far infrared atmospheric mission. *Applied Optics*, 44.

Potter, J. F. (1970). The delta function approximation in radiative transfer theory. *Journal of Atmospheric Sciences*, 27.

Revercomb, H. E., Walden, V. P., Tobin, D. C., Anderson, J., Best, F., Ciganovich, N. C., Dedecker, R. G., Dirkx, T., Ellington, S. C., Garcia, R. K., Herbsleb, R., Knuteson, R. O., LaPorte, D., McRae, D., and Werner, M. (1998). Recent results from two new aircraft-based fourier-transform interferometers: the scanning high-resolution interferometer sounder and the NPOESS atmospheric sounder testbed interferometer. In *ASSFTS Conference*, Toulouse, France.

Rizzi, R., Carli, B., Harries, J. E., Leotin, J., Serio, C., Sutera, A., Bizzarri, B., Bonsignori, R., and Peskett, S. (2001). *Mission objectives and instrument requirements for the REFIR (Radiation Explorer in the Far Infrared) mission: An outline after the end of phase B0*. A. Deepak Publishing Co., Hampton, Virginia.

Rizzi, R., Maestri, T., and Bozzo, A. (2007). Reference tool for simulation of VIS/NIR spectral radiances. Report EUM/CO/06/1529/PS, Eumetsat.

Rizzi, R. and Mannozzi, L. (2000). Preliminary results on the planetary emission between 100 and 600 cm^{-1}, in REFIR-radiation explorer in the far infared, final report. ENV4-CT6 0344 vol. 1, pp. 77-87, Eur. Comm. Brussels. Available at `http://www.adgb.df.unibo.it/refir/report/index_final.html`.

Sassen, K., Wang, Z., and Liu, D. (2008). Global distribution of cirrus clouds from CloudSat/Cloud-Aerosolo Lidar and Infrared Pathfinder Satellite Observation (CALIPSO) measurements. *Journal of Geophysical Resarch*, 113.

Serio, C., Esposito, F., Masiello, G., Pavese, G., Calvello, M. R., Grieco, G., Cuomo, V., Buijs, H. L., and Roy, C. B. (2008a). Interferometer for ground-based observations of emitted spectral radiance from the troposphere: evaluation and retrieval performance. *Applied Optics*, 47:3909–3919.

Serio, C., Masiello, G., Esposito, F., Di Girolamo, P., Di Iorio, T., Palchetti, L., Bianchini, G., Muscari, G., Pavese, G., Rizzi, R., Carli, B., and Cuomo, V. (2008b). Retrieval of foreign-broadened water vapor continuum coefficients from emitted spectral radiance in the h2o rotational band from 240 to 590 cm-1. *Optics Express*, 16-20:15816–15833.

Smith, W. L., Weisz, E., Kireev, S. V., an Zhenglong Li, D. K. Z., and Borbas, E. E. (2012). Dual-regression retrieval algorithm for real-time processing of satellite ultraspectral radiances. *Journal of Applied Meteorology and Climatology*, 51.

Stackhouse, P. W. and Stephens, G. L. (1991). A theoretical and observational study of the radiative properties of cirrus: Results from FIRE 1986. *Journal of Atmospheric Sciences*, 48.

Stephens, G. L. and Vane, D. (2007). Cloud remote sensing from space in the era of the A-Train. *Journal of Applied Remote Sensing*, 1.

Stephens, G. L., Vane, D. G., Boain, R. J., Mace, G. G., Sassen, K., Wang, Z., Illingworth, A. J., O'Connor, E. J., Rossow, W. B., Durden, S. L., Miller, S. D., Austin, R. T., Benedetti, A., Mitrescu, C., and the CloudSat Science Team (2002). The CloudSat mission and the A-Train: A new dimension of space-based observations of clouds and precipitation. *Bulletin of the American Meteorological Society*, 83.

Tobin, D. C., Best, F. A., Brown, P. D., Clough, S. A., Dedecker, R. G., Ellington, R. G., Garcia, R. K., Howell, H. B., Knuteson, R. O., Mlawer, E. J., Revercomb, H. E., Short, J. F., van Delst, P. F. W., and Walden, V. P. (1999). Downwelling spectral radiance observations at the SHEBA ice station: water vapor continuum measurements from 17 to 26 μm. *Journal of Geophysical Research*, 04(D2):2081–2092.

Tobin, D. C., Strow, L. L., Lafferty, W. J., and Olson, W. B. (1996). Experimental investigation of the self- and N_2-broadened continuum within the ν_2 band of water vapor. *Applied Optics*, 35(24):4724–4734.

Turner, D. D., Lesht, B. M., Clough, S. A., Liljegren, J. C., Revercomb, H. E., and Tobin, D. C. (2003). Dry bias and variability in vaisala RS80-H radiosondes: the ARM experience. *Journal of Atmospheric and Oceanic Technology*, 20:117–131.

Turner, D. D. and Mlawer, E. J. (2010). The radiative heating in underexplored bands campaigns. *Bulletin of the American Meteorological Society*, 91:911–923.

Ulanowski, Z., Hesse, E., Kaye, P. H., and Baran, A. J. (2006). Light scattering by complex ice-analogue crystals. *Journal of Quantitative Spectroscopy & Radiative Transfer*, 100.

Veglio, P. and Maestri, T. (2011). Statistics of vertical backscatter profiles of cirrus clouds. *Atmospheric Chemistry and Physics*, 11:12925–12943.

Waliser, D. E., Li, J.-L. F., Woods, C. P., Austin, R. T., Bacmeister, J., Chern, J., Del Genio, A., Jiang, J. H., Kuang, Z., Meng, H., Minnis, P., Platnick, S., Rossow, W. B., Stephens, G. L., Sun-Mack, S., Tao, W.-K.,

Tompkins, A. M., Vane, D. G., Walker, C., and Wu, D. (2009). Cloud ice: A climate model challenge with signs and expectations of progress. *Journal of Geophysical Resarch*, 114.

Wiscombe, W. J. (1977). The delta-M method: Rapid yet accurate radiative flux calculations for strongly asymmetric phase functions. *Journal of Atmospheric Sciences*, 34.

Wylie, D., Jackson, D. L., Menzel, W. P., and Bates, J. J. (2005). Trends in global cloud cover in two decades of HIRS observations. *Journal of Climate*, 18.

Wylie, D. P., Menzel, W. P., Woolf, H. M., and Strabala, K. I. (1994). Four years of global cirrus cloud statistics using HIRS. *Journal of Climate*, 7.

Yang, H., Dobbie, S., Herbert, R., Connolly, P., Gallagher, M., Ghosh, S., Al-Jumur, S. M. R. K., and Clayton, J. (2012). The effect of observed vertical structure, habits, and size distributions on the solar radiative properties and cloud evolution of cirrus clouds. *Quarterly Journal of the Royal Meteorological Society*, 138.

Yang, P., Mlynczak, M. G., Wei, H., Kratz, D. P., Baum, B. A., Hu, Y. X., Wiscombe, W. J., Heidinger, A., and Mishchenko, M. I. (2003). Spectral signature of ice clouds in the far-infrared region: Single-scattering calculations and radiative sensitivity study. *Journal of Geophysical Research*, 108.

Young, S. A., Winker, D. M., Vaughan, M. A., Hu, Y., and Kuhen, R. E. (2008). *CALIOP Algorithm Theoretical Basis Document. Part 4: Extinction Retrieval Algorithms*. NASA.

Yue, Q., Liou, K.-N., Ou, S. C., Kahn, B. H., Yang, P., and Mace, G. G. (2007). Interpretation of AIRS data in thin cirrus atmospheres based on a fast radiative transfer model. *Journal of the Atmospheric Sciences*, 64.

Zhang, Y., Macke, A., and Albers, F. (1999). Effect of crystal size spectrum and crystal shape on stratiform cirrus radiative forcing. *Atmospheric Research*, 52.

Zhang, Z., Platnick, S., Yang, P., Heidinger, A. K., and Comstock, J. M. (2010). Effects of ice particle size vertical inhomogeneity on the passive remote sensing of ice clouds. *Journal of Geophysical Resarch*, 115.

Zhao, Y., Mace, G. G., and Comstock, J. M. (2011). The occurrence of particle size distribution bimodality in midlatitude cirrus as inferred from ground-based remote sensing data. *Journal of the Atmospheric Sciences*, 68.

Zhou, D. K., Smith, W. L., Liu, X., Larar, A. M., Huang, H.-L. A., Li, J., McGill, M. J., and Mango, S. A. (2005). Thermodynamic and cloud parameters retrieval using infrared spectral data. *Geophysical Research Letters*, 32(L15805).